2009

Theoretical and experimental study of solid state complex borohydride hydrogen storage materials

Pabitra Choudhury
University of South Florida

Theoretical and Experimental Study of Solid State Complex Borohydride Hydrogen Storage Materials

by

Pabitra Choudhury

A dissertation submitted in partial fulfillment
of the requirements for the degree of
Doctor of Philosophy
Department of Chemical and Biomedical Engineering
College of Engineering
University of South Florida

Co-Major Professor: Venkat R. Bhethanabotla, Ph.D.
Co-Major Professor: Elias Stefanakos, Ph.D.
Yogi Goswami, Ph.D.
Vinay Gupta, Ph.D.
Lilia Woods, Ph.D.
Sesha Srinivasan, Ph.D.

Date of Approval:
September 25, 2009

Keywords: Density functional theory, lattice dynamics, thermodynamics, stability, mechano-chemical process, nanocatalyst doping

Dedications

To my parents, wife and my newly born son.

Acknowledgements

First, I would like to thank my wife, parents and brothers, and for their unwavering love and support. Your encouragement and loyalty mean the world to me.

I am deeply indebted to my advisors, Professor Venkat R. Bhethanabotla and Professor Elias Stefanakos, for their excellent supervision throughout my Ph.D. study. I could not have reached this point without their tonic advices and patient guidance during each stage of my research work.

I would also like to thank Dr. Sesha Srinivasan and Mr. Brian Smith for the help they provided during the last few years.

I thank Prof. Yogi Goswami, Prof. Vinay Gupta, Prof. Lilia Woods, and Dr. Sesha Srinivasan for agreeing to be in my Ph.D. defense committee.

I would also like to acknowledge the computational resources provided by USF Research Computing. As one of the users of their systems, an unlimited time was granted for usage and great support was provided for technical problems, without which, this dissertation would be possible.

I am grateful for the support of my fellow group members, Subramanian Sankaranarayanan, Reetu Singh, Nianthrini Balakrishnan, Michael Jurczyk and Jonathan Mbah, who have accompanied me on this journey. Thank you for the assistance you have given me and, most of all, for your friendship. I wish you well.

Table of Contents

List of Tables

List of Figures

Theoretical and Experimental Study of Solid State Complex Borohydride Hydrogen Storage Materials

Pabitra Choudhury

ABSTRACT

Materials that are light weight, low cost and have high hydrogen storage capacity are essential for on-board vehicular applications. Some reversible complex hydrides are alanates and amides but they have lower capacity than the DOE target (6.0 wt %) for 2010. High capacity, light weight, reversibility and fast kinetics at lower temperature are the primary desirable aspects for any type of hydrogen storage material. Borohydride complexes as hydrogen storage materials have recently attracted great interest.

Understanding the above parameters for designing efficient complex borohydride materials requires modeling across different length and time scales. A direct method lattice dynamics approach using *ab initio* force constants is utilized to calculate the phonon dispersion curves. This allows us to establish stability of the crystal structure at finite temperatures. Density functional theory (DFT) is used to calculate electronic properties and the direct method lattice dynamics is used to calculate the finite temperature thermodynamic properties. These computational simulations are applied to understand the crystal structure, nature of bonding in the complex borohydrides and

mechanistic studies on doping to improve the kinetics and reversibility, and to improve the hydrogen dynamics to lower the decomposition temperature.

A combined theoretical and experimental approach can better lead us to designing a suitable complex material for hydrogen storage. To understand the structural, bulk properties and the role of dopants and their synergistic effects on the dehydrogenation and/or reversible rehydrogenation characteristics, these complex hydrides are also studied experimentally in this work.

Chapter 1 - Introduction

Clean Energy is one of the greatest environmental and geopolitical challenges of recent times. Inexpensive and plentiful energy is in great demand for our current standard of living – which can at the moment only be supported by fossil fuels, which pollute the air by emitting green house gas CO_2. 32.8% of the total energy is used by the transportation sector in the United States according to the Energy Information Administration's (EIA) Emissions of Greenhouse Gases in the United States 2004 report. For transportation, petroleum products are primarily used, which cause major CO_2 emission to the environment. To prevent global warming, we have to adopt new strategies to harness inexhaustible sources of energy[1].

1.1. Current scenario of energy resources

In general, oil, gas and coal along with nuclear energy and thermomechanical energy are considered three primary categories of energy sources. The first type of energy is due to breaking chemical bonds of any chemical compound such as hydrocarbon. The first type of primary energy sources is generally called fossil fuel. This type of energy can also come from absorbing sunlight and generating heat or electricity. The second type of energy is due to nuclear reaction from fission of heavy nuclei or fusion of light nuclei. The amount of energy generated in this reaction in the order of MeV per reaction. The third type of energy is thermomechanical energy which

includes water, wind, and geothermal steam or hot water. The energy involved in this type is very low (meV) compare to other two types of energy sources.

Global energy consumption has increased tremendously over the past few decades. The world primary energy consumption has shown in Table 1-1. The energy data are expressed in million tonnes of oil equivalent (Mtoe) which is the amount of energy (~ 42 GJ) released after burning of one tonne of crude oil. The world's energy need is expected to (at least) double within the next half century. Essentially, the current world depends solely on first type of primary resources, which are expected to deplete in the very near future. Overexploitation of these fossil fuels is also main cause of global warming, environmental pollution and acid rain.

Table 1-1. World energy consumption by fuel (2007)

Region	Million Tonnes of oil equivalent (Mtoe)					
	Oil	Natural Gas	Coal	Nuclear Energy	Hydro-electricity	Total
Total North America	1134.7	728.9	613.3	215.6	146.2	2838.7
Total S & C America	252.0	121.1	22.4	4.4	153.1	553.0
Total Europe & Eurasia	949.4	1040.1	533.7	275.6	188.6	2987.4
Total Middle East	293.5	269.4	6.1	-	5.1	574.1
Total Africa	138.2	75.2	105.9	3.0	22.2	344.5
Total Asia Pacific	1185.1	403.1	1896.2	123.4	194.0	3801.8
Total World	3952.9	2637.8	3177.6	622.0	709.2	11099.5

Source: BP Statistical review of World Energy – June 2008

The production of energy is expected to remain adequate in coming few decades. However, imbalance of energy consumption is widely accepted around the world. Most of the developed and developing countries need to consume more energy to ensure economic growth resulting very high energy consumption (Table 1-2). As the energy can be produced from fossil fuels *via* straightforward combustion process, they are relatively inexpensive and easy to transport. However, fossil fuels are essentially non-renewable energy sources in the long-term. The geological processes which create fossil fuels take millions of years, so they cannot be regenerated within the timescales of human race once they have been exhausted.

Table 1-2. World primary energy production by fuel (2007)

Region	Million Tonnes of oil equivalent (Mtoe)			
	Oil	Natural Gas	Coal	Total
Total North America	643.4	706.3	629.9	1979.6
Total S & C America	332.7	135.7	55.3	523.7
Total Europe & Eurasia	860.8	968.2	445.4	2274.4
Total Middle East	1201.9	320.2	0.5	1522.6
Total Africa	488.5	171.3	154.2	814.0
Total Asia Pacific	378.7	352.3	1850.2	2581.2
Total World	3906	2654.0	3135.5	9737.6

Source: BP Statistical review of World Energy – June 2008

It can be observed from Table 1-1 that the ever-increasing (by 2.7% in 2007) consumption for energy coupled with decreasing fossil fuel resources due to

overexploitations make the establishment of a clean and sustainable energy system a compelling need. Hydrogen-based energy systems seem to be potential solutions. Although, in the long-term, the ultimate technological challenge is large-scale production of hydrogen from renewable sources, the challenging issue is how to store hydrogen efficiently for onboard vehicular application powered by fuel-cell.

1.2. Hydrogen as an energy carrier

Hydrogen is considered the greatest energy carrier amongst all sustainable fuels because of its highest heat of combustion (-33.3 kwh/kg) amongst all fuels. Hydrogen is also the cleanest fuel because after combustion it produces only water which is completely harmless, and it is also easily available; of course it is not freely available in nature; it can be produced easily by various methods such as steam reforming, electrolysis of water, etc., and used as an energy carrier. Thus, hydrogen is the ideal fuel for the future since it reduces significantly the greenhouse gas emissions, reduces the global dependence on fossil fuels, and increases the efficiency of the energy conversion process for both internal combustion engines and proton exchange membrane (PEM) fuel cells. Hydrogen used in the fuel cell converts directly the chemical energy of hydrogen into water, electricity and heat[2] as represented by the :

$$H_2 + \tfrac{1}{2} O_2 \rightarrow H_2O + \text{Electricity} + \text{Heat} \qquad 1\text{-}1$$

From the phase diagram[3] it can be observed that hydrogen is gaseous at temperatures above 32 K and H_2 gas reacts, in concentrations down to 4.73%, explosively with air. Hydrogen is an extremely clean energy resource for many purposes such as turbine engines and vehicular applications; however, it requires very high pressure for gas phase storage which is unsafe in these applications.

1.3. Hydrogen storage methods

The typical hydrogen storage options are: (i) compressed hydrogen, (ii) liquid hydrogen and (iii) solid hydrogen materials. Compressed hydrogen requires very high potential energy to store and requires bulky tanks. Liquid hydrogen has reasonably higher density than gaseous phase but it requires very low temperature (-253 ^{o}C) and also requires very high liquefaction energy. Hence, solid hydrogen storage materials are the appropriate choice for practical hydrogen storage for on-board vehicular applications. Hydrogen can be stored in the solid media *via* physisorption and chemisorption. The key concept of hydrogen adsorption/desorption is that hydrogen strongly affects the electronic and structural properties of the materials. In terms of electronic structure, the proton acts as an attractive potential to the host-metal electrons; electronic bands are lowered in energy and form low-lying bonding bands by hybridization with the hydrogen *s* orbital. This results in change of electronic structure and energy bandgap during hydrogen adsorption/desorption process.

1.3.1. Hydrogen storage *via* physisorption

Nanoporous materials, which have diverse tunable physical properties as a function of their size and shape due to strong quantum confinement effect and large surface to volume ratio, such as activated carbons, zeolites, carbon nano tubes, conducting polymers and metal organic frameworks (MOFs) can be considered to be strong candidate for hydrogen storage[4-6]. The main advantage of hydrogen storage *via* physisorption is that these materials can store and release hydrogen with fast kinetics and high reversibility over multiples cycles. The binding of hydrogen into the porous materials is due to the weak Van der Walls interaction force (~10 kJ/mol) results in fast

adsorption/desorption kinetics. But the hydrogen storage capacity for all above mentioned materials, except for some conducting polymers[6], fall short of the Department of Energy (DOE) target.

1.3.2. Hydrogen storage *via* chemisorption

Over the decades, the exploration and the scope of the hydrogen storage researches have been extended to hydrogen storage *via* chemisorption methods because of high storage capacity (gravimetric and volumetric) and tunable kinetic and thermodynamic parameters by addition of both catalysts and mixing of hydride phases. In chemisorption, unlike physisorption, both pressure and temperature play an important role to change the chemical transformation of the parent compounds *via* formation/breaking of chemical bonds. These chemical bonds between the hydrogen atom and the metal can lead to the stronger bonded chemisorbed state, and finally the hydrogen atoms can diffuse into the host crystal lattice. The chemisorption energy is typically in order of ~ 60 kJ/mol. Some examples of such materials are simple metal hydrides, hydrides in nanophase structures and complex hydrides.

1.3.2.1 Metal hydrides

The simplest chemical compositions of metal hydrides are called the binary hydrides, on the form MH_x. Depending on the electronegativity of the metal M it forms different kinds of metal hydrides. Group I and II metals can be bonded to hydrogen ionic bonds. Covalent hydrides can formed with both non metallic (Group III – V) and light weight elements (Group I). Transition metal hydrides are generally form interstitial hydrides where hydrogen atoms occupy tetrahedral or octahedral interstitial sites, or a

combination of both. As interstitial hydrides consist of relatively heavy elements therefore they have low hydrogen capacity by weight. Metal hydrides with alloys are called intermetallic hydrides on the form $A_xB_yH_z$, where A typically represent a rare earth or an alkaline earth metal that tends to form stable hydrides, while B often is a transition metal which forms unstable hydrides[3]. The common host alloys of intermetallic hydrides are AB, AB_3 and AB_5[7]. If this happens, the hydrogen is distributed compactly throughout the intermetallic lattice.

1.3.2.2 Complex hydrides

Complex hydrides are different from simple metal/intermetallic hydrides. In metal or intermetallic hydrides hydrogen atoms are encapsulated in metallic interstitial sites whereas in complex hydrides several hydrogen atoms surround other atom (such as Al, B, or N) to form complex characteristics. Complex hydrides with light-elements have higher hydrogen coordination number than simple metal/intermetallic hydrides and also much higher hydrogen storage capacity than transition metal hydrides. Their thermal stability of the complex hydrides can be flexible due to the co-existence of both covalent and ionic types of bonding. Practically it is possible to synthesize complex hydrides by mixing of existing hydrides, which allows the synthesis of materials with desired properties by tailoring the synthesis process. Among the most viable candidates, complex hydrides are considered to be the best candidates for the onboard hydrogen storage application due to both high hydrogen storage capacity and desirable absorption/desorption thermodynamics/kinetics.

1.4. Role of theoretical and experimental research on hydrogen storage materials

Critical properties of the hydrogen storage materials to be evaluated for automotive applications are: (a) light weight, (b) cost and availability, (c) high volumetric as well as gravimetric density of hydrogen, (d) fast kinetics, (e) low dehydrogenation temperature, (f) favorable thermodynamic properties, (g) long cyclibility and (h) high degree of reversibility. All the above mentioned properties pose many scientific and technical challenges for the development of new materials for hydrogen storage. Since a combined theoretical and experimental approach can lead to design a suitable complex material for hydrogen storage, both experimental and theoretical research is required for understanding of properties and hydrogenation-dehydrogenation mechanisms of stoichiometric complex hydrides, their synthesis and processing, and role of catalytic dopants. This requires intimate collaboration between experiment and theory, and also integrated efforts from physics, chemistry, material science, and engineering.

The absorption/desorption energy and hence the thermodynamic properties of the material can be tailored by manipulating the physical and electronic structures of the material. Quantum mechanical calculations are used to explain the nature of chemical bonding and the preferred occupancy sites for hydrogen atoms in hydrogen storage materials, and the activation energy barriers, diffusion paths, and catalysis mechanisms during hydrogen uptake and release. Modeling and simulation can help in analyzing the experimental data and identifying the key factors for hydrogen storage capacity improvements, and also provide guidance for further experiments. Thus computer simulation is considered to be a powerful tool in characterizing the structure and

hydrogen storage/diffusion properties and also in understanding the destabilization mechanisms and various structure-properties relationships.

Various methods are used to synthesize different kinds of hydrides, including solid-gas reaction, solution methods, mechano-chemical, ion implantation, and electrochemical methods. Solution methods are usually used to synthesize complex metal hydrides. They often introduce impurities that are hard to remove from the materials, and result in formation of irreversible hydrides in many cases. Thus mechano-chemical synthesis technique in a hydrogen environment is currently the most popular method to synthesize hydrogen storage materials. Mechano-chemical milling yields samples in fine powders results in no practical growth of single crystal. These difficulties make X-ray absorption near-edge structure spectroscopy (XANES) and photoelectron spectroscopy (PES) hard to apply. Hydrogen atom is the lightest element in the periodic table as a result it is very difficult to identify the hydrogen atoms using X-ray diffraction. Hydrogen shows the most significant isotope effect of all elements. Therefore deuterides (having better coherent scattering) can be used to determine the location of the hydrogen atoms easier. Sometime, Neutron powder diffraction in combination with high resolution X-ray diffraction (synchrotron) is used in the structure determination. Inelastic neutron scattering (INS) is used to study interatomic interactions and locate hydrogen positions in low concentration hydrides. Nuclear magnetic resonance (NMR), infrared (IR), Raman, are used to give information on local structures and coordinated hydrogen dynamics in materials that can be compared with the theoretically predicted phonon spectra. Understanding the physico-chemical reactions and synergistic effects of the nanocatalysts on the complex hydrides can also be predicted *via* different experimental techniques.

Experimentally predictive hydrogen storage capacity, thermodynamic stability and kinetic enhancement due to nanocatalyst doping on these complex hydrides can also be supported the theoretical calculations. The schematic representation of combined theoretical and experimental approach is shown below (Figure 1-1).

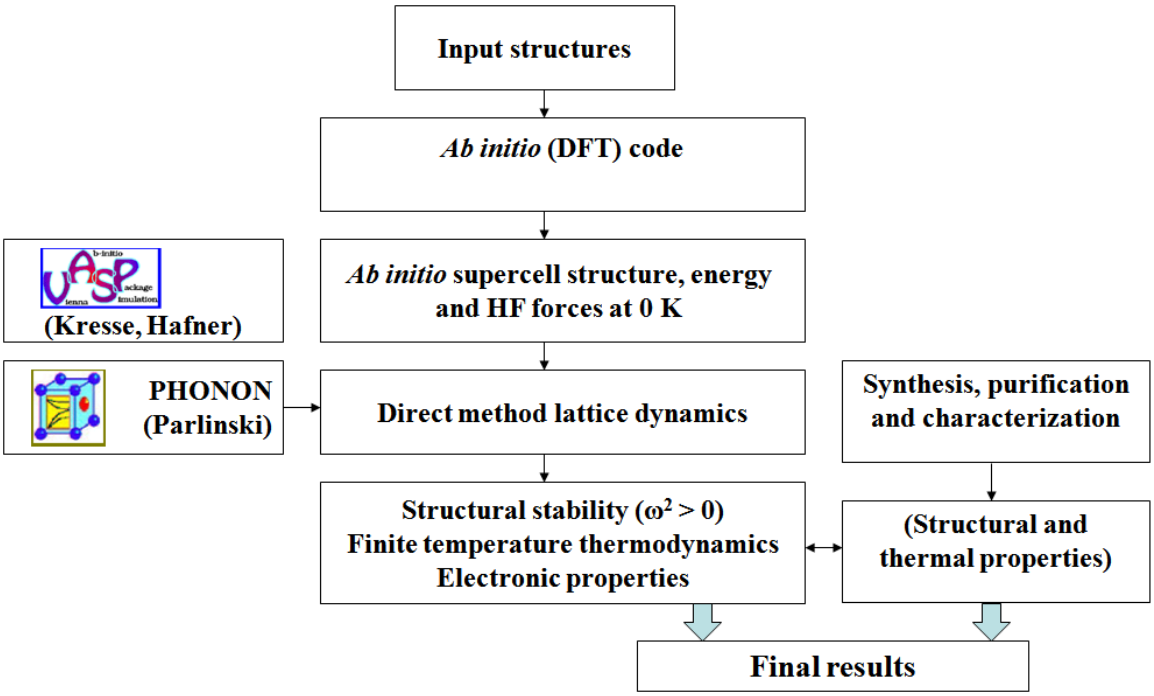

Figure 1-1. Schematic representation of combined theoretical and experimental approach

Sometime, materials having all the favorable properties like energetics and thermodynamics are not suitable for hydrogen storage because of the poor kinetics and irreversibility. These cannot be predicted by theoretical simulation but with experiment, can be determined easily. Thus, both experimental and theoretical research is needed to design suitable hydrogen storage materials.

1.5. Organization of the dissertation

This dissertation is organized as follows:

- Chapter 2 provides details of the theoretical approach implemented for fundamental study by density functional theory and finite temperature thermodynamics by direct method lattice dynamics of complex borohydrides.
- Chapter 3 describes the experimental tools/techniques implemented for the analysis of complex borohydrides in our study including destructive and nondestructive methods/techniques.
- Chapter 4 discuses the first principle investigation of stable crystal structure of zinc borohydride at finite temperature.
- Chapter 5 studies the fundamental understandings of the role of Ni additives in promoting the dehydrogenation mechanism of hydrogen de-sorption in zinc borohydride.
- Chapter 6 studies the crystal structure, electronic structure and dehydrogenation thermodynamics of $Mn(BH_4)_2$ and also compares with the experimental IR spectroscopy data.
- Chapter 7 discuses the quantitative hydrogen storage capacity and compositions at each dehydrogenation reaction steps for the multinary complex borohydride Li-Mg-B-N-H system. It also discuses about the reversible hydrogen storage capacity and feasibility of application to the real fuel cell system for onboard application.
- Chapter 8 presents the experimental study of Li-Mn-B-H system, member of a new class of complex borohydrides for hydrogen storage.

- Chapter 9 summarizes the contents of this dissertation and suggests possible future research directions.

Chapter 2 - Theoretical Approach

In this chapter, the basic concepts of theoretical approaches for the study of complex borohydrides are presented. Firstly, the foundations of density functional theory calculations and the direct method lattice dynamics calculations are presented.

2.1. Density functional theory

Density functional theory is a theory of correlated many-body systems. This is a remarkable theory that allows one to replace the complicated N-electron wave function $\Psi(x_1, x_2, \ldots, x_N)$ and the associated Schrödinger by the much simpler electron density $\rho(r)$ and its associated calculation scheme.

Hohenberg and Kohn[8] provided the basis for DFT in 1964 and proved that all electronic properties of the system could be uniquely defined by its ground state probability density. This provided an alternative to the wave functions. However, the theorems didn't provide a practical scheme to calculate the ground state properties from electron density. The modification was provided by Kohn and Sham[9] (1965) who reformulated the problem of calculating the total electronic energy E as a functional of the electron density ρ(r) to that of solving a set of single-particle Schrödinger like equations.

Thus,

$$E[\rho] = T[\rho] + \int \rho(\vec{r}) v_{ext}(\vec{r}) d\vec{r} + \frac{1}{2} u(\vec{r}) d\vec{r} + E_{xc}(\rho) \qquad 2\text{-}1$$

$T[\rho]$, v_{ext} and u are kinetic energy, external potential and inter electronic repulsion, respectively. E_{xc} is the exchange correlation functional which includes everything not contained in other terms. There are several approximations to calculate the correlation functional such as local density approximation (LDA)[10], generalized gradient approximation (GGA)[11] amongst several others. In LDA the spatial variations in density are ignored and potential at any point is calculated as that for a homogeneous electron gas with the density at that point. In GGA, the exchange and correlation energies are dependent not only on the electron density, but also on the derivatives of electron density. Recently, several hybrid approaches have been developed that allow even more accurate calculation of energies and structures[12, 13].

An extensive study by *ab initio* DFT calculations would allow us to develop a complete picture of the electronic structure of complex borohydrides by (i) calculating the lattice parameter of the crystal structure, (ii) the systematic search for the thermodynamically stable phases of complex hydrides by calculating the enthalpy of formation of the complex hydrides, (iii) electronic partial and total density of state (DOS) and band structure calculations of complex hydrides.

2.1.1. Hohenberg-Kohn theorem

The approach of Hohenberg and Kohn[8] is to formulate density functional theory as an *exact theory of many-body systems*. The formulation applies to any system interacting particles in an external potential $v_{ext}(r)$, including any problem of electrons and fixed nuclei, where the Hamiltonian can be written as:

$$\hat{H} = -\frac{h^2}{2m_e}\sum_i \nabla_i^2 + \sum_i v_{ext}(r_i) + \frac{1}{2}\sum_{i\neq j}\frac{e^2}{|r_i - r_j|} = \hat{T} + \hat{V} + \hat{U} \qquad 2\text{-}2$$

The basic lemma of Hohenberg-Kohn theorem is that the ground-state density ρ(r) of a bound system of interacting electrons in some external potential $v_{ext}(r)$ determines this potential uniquely. The proof is reproduced as follow:

Let ρ(r) be the nondegenerate ground-state density of N electrons in the potential $v_{ext}(r)$, corresponding to the ground state Ψ, and the energy E. Then,

$$E = (\Psi, H\Psi) = \int v_{ext}(r)\rho(r)dr + (\Psi, (T+U)\Psi) \qquad 2\text{-}3$$

Where, H is the total Hamiltonian corresponding to $v_{ext}(r)$, and T and U are the kinetic and interaction energy operators. Now assume that there exists a second potential $v_{ext}{}^{1}(r)$, *not* equal to $v_{ext}(r)$ + constant, with ground state Ψ^1, necessarily $\neq e^{i\theta\Psi}$, which gives rise to the same ρ(r).

Then,

$$E^1 = \int v_{ext}{}^{1}(r)\rho(r)dr + \int (\Psi^1, (T+U)\Psi^1) \qquad 2\text{-}4$$

Since Ψ is assumed to be nondegenerate, the Rayleigh-Ritz minimal principle for Ψ gives the inequality

$$\begin{aligned} E < (\Psi^1, H\Psi^1) &= \int v_{ext}(r)\rho(r)dr + (\Psi^1, (T+U)\Psi^1) \\ &= E^1 + \int (v_{ext}(r) - v_{ext}{}^{1}(r))\rho(r)dr \end{aligned} \qquad 2\text{-}5$$

Similarly,

$$E^1 \le (\Psi, H\Psi) = E + \int (v_{ext}{}^{1}(r) - v_{ext}(r))\rho(r)dr \qquad 2\text{-}6$$

Where we use ≤ since the nondegeneracy of Ψ^1 was not assumed. Adding (2-5) and (2-6) leads to the contradiction.

$$E + E^1 < E + E^1 \qquad 2\text{-}7$$

We conclude by *reductive ad absurdum* that the assumption of the existence of a second potential $v_{ext}^{1}(r)$, which is unequal to $v_{ext}(r)$ + constant and gives the same ρ(r), must be wrong. The lemma is thus proved for a nondegenerate ground state. Since ρ(r) determines both N and $v_{ext}(r)$ (ignoring an irrelevant additive constant) it gives us the full H and N for the electronic system. Hence ρ(r) determines implicitly all properties derivable from H through the solution of the time-independent or time-dependent Schrödinger equation.

The second lemma of the Hohenberg-Kohn theorem is that for any external potential applied to an interacting particle system, it is possible to define a universal total energy functional of the particle density, which is written as

$$E_v[\rho] = \int v_{ext}(r)\rho(r)dr + F_{HK}[\rho] \qquad 2\text{-}8$$

Where $F_{HK}[\rho]$ is universal functional by construction since the kinetic energy and interaction energy of the particles are functionals only of the density and is defined as

$$F_{HK}[\rho] = (\Psi, (T+U)\Psi) \qquad 2\text{-}9$$

$$T \equiv \frac{1}{2}\int \nabla\psi^{*}(r)\nabla\psi(r)dr \qquad 2\text{-}10$$

$$U \equiv \frac{1}{2}\int \frac{1}{|r-r^{1}|}\psi^{*}(r)\psi^{*}(r^{1})\psi(r)\psi(r^{1})drdr^{1} \qquad 2\text{-}11$$

It follows that if the functional $F_{HK}[\rho]$ is known, then by minimizing the total energy of the system, Equation (2-7), with respect to variations in the density function $\rho(r)$, one would find the exact ground state density and energy. This means that the energy functional equals the ground-state energy for the correct $\rho(r)$, and has a minimum, given that the number of particles of the system $N[\rho] \equiv \int\rho(r)\mathrm{d}r$ is kept constant.

2.1.2. Self consistent Kohn-Sham equation

The Kohn-Sham approach[9] (1965) is to replace the difficult interacting many-body system obeying the Hamiltonian with a different auxiliary system that can be solved more easily. The *ansatz* of the Kohn and Sham assumes that the ground state density of the original interacting system is equal to that of some chosen non-interacting system. This leads to independent particles for the non-interacting system that can be solved with all the difficult many-body terms incorporated into an exchange-correlation functional of the density as shown in Equation (2-1).

The set of wave functions $\psi_i(r)$ that minimize the Kohn-Sham total energy functional are given by the self-consistent solutions to the Kohn-Sham shown in (2-12) and (2-13).

$$\left[-\frac{h}{2m}\nabla^2 + V_{eff}\right]\psi_i(r) = \varepsilon_i\psi_i(r) \qquad 2\text{-}12$$

$$V_{eff} = V_{ext} + V_H + V_{xc} \qquad 2\text{-}13$$

where ε_i are the eigenvalues, $\psi_i(r)$ are the Kohn-Sham orbitals and $V_{eff}(r)$ is the effective potential, V_H is the Hartree potential given by Equation (2-14)

$$V_H = \int \frac{\rho(r')}{|r-r'|}dr' \qquad 2\text{-}14$$

The V_{xc}, the exchange-correlation potential is the derivative of exchange-correlation energy functional with respect to the ground state density, given by Equation (2-15).

$$V_{xc}(r) = \frac{\delta E_{xc}[\rho(r)]}{\delta\rho(r)} \qquad 2\text{-}15$$

By construction, the exact ground-state density, $\rho(r)$, of an N-electron system is given by

$$\rho(r) = \sum_i |\psi_i(r)|^2 \qquad 2\text{-}16$$

As can be seen, by solving the equations one can finds the ground state density and energy of original interacting system with the accuracy limited only by the approximations in the exchange-correlation functional. If the exchange-correlation potential defined in Equation (2-15) is known, the exact ground-state density and energy of the many-body electron problem can be found by solving the single-particle Kohn-Sham equation.

2.1.3. Exchange and corelations functionals approximations

The most important approximations for $E_{xc}[\rho(r)]$ have a quasilocal form. The $E_{xc}[\rho\ (r)]$ can be written in the form

$$E_{xc}[\rho(r)] = \int \varepsilon_{xc}(r;[\rho(\tilde{r})])\rho(r)dr \qquad 2\text{-}17$$

Where $\varepsilon_{xc}(r;[\rho(\tilde{r})])$ represents an exchange-correlation (*xc*) energy/particle at the point *r*, which is a functional of the density distribution $\rho(\tilde{r})$. It depends primarily on the density $\rho(\tilde{r})$ at points $\tilde{r}$ near *r*. The simplest approximation for E_{xc} is the so-called local-density approximation (LDA).

$$E_{xc}^{LDA} = \int \varepsilon_{xc}(\rho(r))\rho(r)dr \qquad 2\text{-}18$$

Where $\varepsilon_{xc}(\rho)$ is the exchange-correlation energy per particle of a uniform electron gas of densityρ. The exchange-correlation, $\varepsilon_{xc}(\rho)$ has two part exchange, $\varepsilon_x(\rho)$ and correlation, $\varepsilon_c(\rho)$ given, in atomic units, by

$$\varepsilon_x(\rho) = -\frac{0.458}{r_s} \qquad 2\text{-}19$$

Where r_s, is the radius of a sphere containing one electron and given by $\frac{4\pi}{3} r_s^3 = \rho^{-1}$. The correlation part was first estimated by Wigner (1938)[14]:

$$\varepsilon_c(\rho) = -\frac{0.44}{r_s + 7.8} \qquad 2\text{-}20$$

and more recently with a high precision of about ±1% by Ceperley (1978); Ceperley and Alder (1980) using Monte Carlo methods [15, 16].

A better way to improve the LDA is to consider the exchange-correlation energy density not only depending on the density ρ(r) but also on its gradient $\nabla\rho$(r). These new expressions are called generalized gradient approximation (GGA).

$$E_{xc}^{GGA} = E_{xc}[\rho; \nabla\rho] \qquad 2\text{-}21$$

In practice, there are various forms of GGA for different requirements, such as the Perdew-Becke form, the Perdew-Wang 86 form, and the Langreth-Mehl-Hu form, etc. Becke introduced another approach to improve the LDA is called hybrid method:

$$E_{xc}^{hyb} = \alpha E_x^{KS} + (1-\alpha) E_{xc}^{GGA} \qquad 2\text{-}22$$

where E_x^{KS} is the exchange energy calculated with the exact KS wave functions, E_{xc}^{GGA} is an appropriate GGA, and α is a fitting parameter[17]. Use of GGA's and hybrid approximations instead of the LDA has reduced errors of atomization energies of standard sets of small molecules, consisting of light atoms, by factors of typically 3–5. The improved accuracy of exchange-correlation functionals and capability of DFT to deal with systems of many atoms, has, over the time DFT become the preferred method for calculating total energies and hence cohesive energies of most condensed-matter systems including solid state complex hydrides.

2.2. Solving self consistent Kohn-Sham equation

In Equation (2-12) the effective potential depends on the electron density ρ(r), which depends on the Kohn-Sham orbitals $\psi_i(r)$, which are being searched. It means that the Kohn-Sham have to be solved iteratively until a self-consistent solution being reached. The schematic diagram is shown in Figure (2-1).

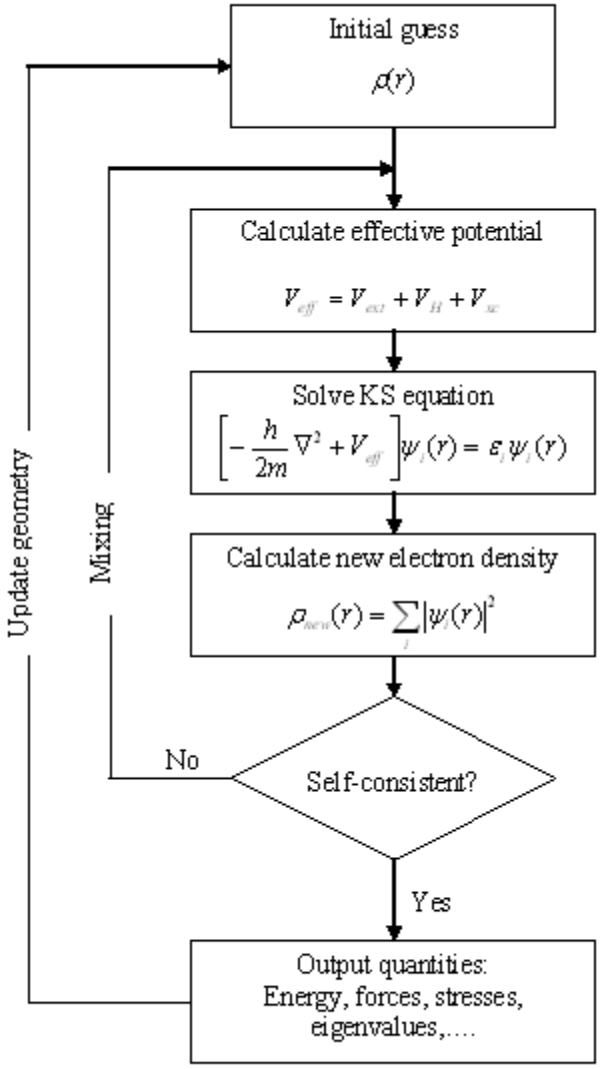

Figure 2-1. Schematic representation of the self-consistent loop for solution of Kohn-Sham equation[18].

2.2.1. Basis set for solution

For a solid state system, the effective potential in the Kohn-Sham Equation (2-12) has the periodicity of the crystalline lattice. Therefore, the Kohn-Sham orbitals, $\psi_k^n(r)$, can be written as a product of a function $u_k^n(r)$ that has the periodicity of the crystal lattice and a plane wave $e^{ik.r}$ with k being any wave vector in the first Brillouin zone, i.e.

$$\psi_k^n(r) = u_k^n(r)e^{ik.r} \qquad 2\text{-}23$$

According to the Bloch theorem, a plane wave basis set is used, the periodic function in Equation (2-23) can be written as a sum over plane waves that have the same periodicity as it. Such plane waves are those ones corresponding to reciprocal lattice vectors. Thus, the expansion of $\psi_k^n(r)$ in this basis set is

$$\psi_k^n(r) = \frac{1}{\Omega_{cell}} \sum_j C_j^n(k) e^{i(k+K_j).r} \qquad 2\text{-}24$$

Where Ω_{cell} is the volume of the primitive cell, K_j are the reciprocal lattice vectors and the parameter n is called band index. It should be pointed out that this basis set is k-dependent, i.e. the eigenstates $\psi_k^n(r)$ corresponding to different k vectors are represented by different basis sets. The plane wave basis set can be truncated by setting all K_j with $K \leq K_{max}$. This means that all reciprocal lattice vectors that are inside a sphere with radius K_{max} are taken into the basis set. It is more common to specify the free electron energy corresponding to K_{max}, which is called cut-off energy

$$E_{cut} = \frac{\hbar^2 K_{\max}^2}{2m} \qquad 2\text{-}25$$

However the basis set will still be intractably large for systems that contain both valence and core electrons. If we look at the radial part of a conduction electron wavefunction,

we see that close to the atom core it displays a nodal behavior, while further away from the core; the wavefunction is smooth and vary as plane waves. The nodal behavior ensures orthogonality of the wavefunctions. Because the radial wavefunctions vary intensely with the smallest radii, many plane waves are required to describe this part of the wavefunction, while much lesser number plane waves are required for the outermost parts. A smart way to reduce the number of plane waves needed is the use of pseudopotentials.

2.2.2. Pseudopotentials and ultra-soft pseudopotential

In the previous section, many plane waves are needed to describe the nodal behavior close to the core region of the radial wavefunction of a conduction electron. If we treat the conduction electrons in the interstitial regions as plane waves, the energy must depend on the wavevector approximately as $\varepsilon_{\vec{k}} = \frac{\hbar^2 k^2}{2m}$ as for free electrons[19]. Using the Hamilton operator, one can calculate the energy of an orbital at any point in space. This means that in the interstitial regions, this energy will be close to the above free electron energy. The wavefunctions' behavior close to the core does not affect the dependency of ε on $\vec{k}$ much, or in other words; the outer regions are mainly responsible for the chemical reactions. This leads to the idea of replacing the core potential with a .pseudopotential that gives the same wavefunctions outside the core[20, 21], but simpler ones inside the core. This is why the pseudopotential best fits the outer side and nearly zero fits inside the core[19]. An example of pseudopotential is shown in Figure 2-2.

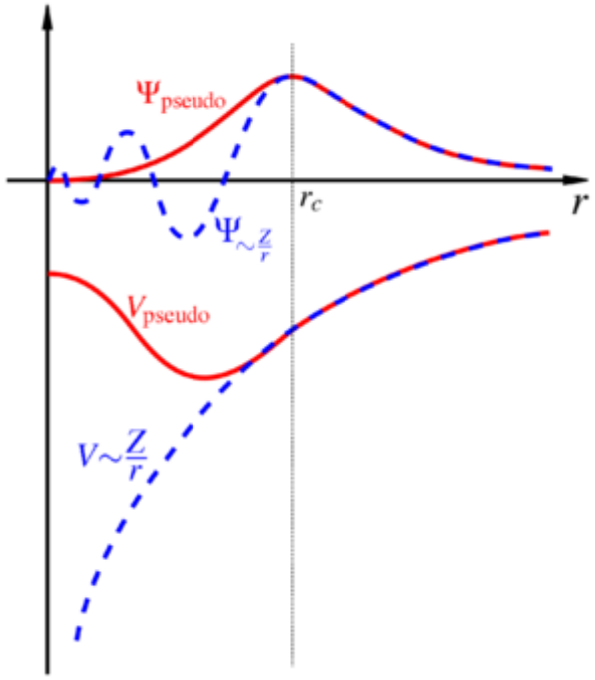

Figure 2-2. Illustration of the real and pseudo wave-function and the real and pseudopotential[22].

Pseudopotentials can be soft or hard. A soft pseudopotential includes only the outermost electrons and requires only a few plane waves[23]. A hard pseudopotential includes some of the core electrons and requires hence more planewaves. Some pseudopotential is called ultrasoft, as very small number of plane waves needed to describe them. Although the norm-conserving pseudopotentials can be used in many general solid state calculations, their application is limited for systems containing first-row and transition-metal elements. The difficulty lies in the inefficiency to represent the highly localized *p* and *d* orbitals which are already nodeless. The pseudo wave function can be made softer by pushing the cutoff radius outward[23, 24], but the norm-conserving constraint leaves little room for any significant improvement in the procedure.

2.2.3. Projector-augmented-plane-wave method

The projector augmented wave (PAW) method[25] is a general approach to solution of the electronic structure problem that reformulates the orthogonalized plane waves (OPW), adapting it to modern techniques for calculations of total energy, forces and stresses. Like the ultrasoft pseudopotential method, it introduces projectors and auxiliary functions. The PAW approach also defines a functional for the total energy that involves auxiliary functions and it uses advances in algorithms for efficient solution of the generalized eigenvalue problem. The PAW method is an all-electron frozen core method, which combines the features of both the ultra-soft pseudopotentials and linear augmented plane wave (LAPW) methods. It allows an easier treatment of first-row and transition-metal elements, and provides access to the full wave function. In real materials, the wave function is fairly smooth in the bonding region, whereas it varies rapidly near the nucleus due to the large attractive potential. This is the main difficulty for electronic structure methods to describe the bonding region with accuracy as well as account for the large variations in the atomic core. The augmented-wave methods deal with this problem by dividing the wave function into two parts, i.e., a partial-wave expansion within an atom-centered sphere and envelope functions outside the spheres. The value and derivative of the two parts are then matched at the sphere radius.

In the PAW method, one can define a smooth part of valence wavefunction $\tilde{\psi}_i^v(r)$ or an atomic orbital and a linear transformation $\psi^v = \tau\tilde{\psi}^v$ that relates the set of all-electron valence functions $\tilde{\psi}_j^v(r)$ to the smooth functions $\tilde{\psi}_i^v(r)$. The transformation is assumed to be unity except with a sphere centered on the nucleus, $\tau = 1 + \tau_0$. For simplicity, we omit the superscript *v*, assuming that the ψs are valence states, and the

labels *i*, *j*. Using the Dirac notation, the expansion of each smooth function $|\tilde{\psi}\rangle$ in partial waves *m* within each sphere can be written Equation (2-26),

$$|\tilde{\psi}\rangle = \sum_m c_m |\tilde{\psi}_m\rangle \qquad 2\text{-}26$$

with a the corresponding all-electron function,

$$|\psi\rangle = \tau|\tilde{\psi}\rangle = \sum_m c_m |\psi_m\rangle \qquad 2\text{-}27$$

Hence the full wave function in all space can be written

$$|\psi\rangle = |\tilde{\psi}\rangle + \sum_m c_m \{|\psi_m\rangle - |\tilde{\psi}_m\rangle\} \qquad 2\text{-}28$$

If the transformation τ is required to be linear, then the coefficients must be given by a projection in each sphere

$$c_m = \langle \tilde{p}_m | \tilde{\psi} \rangle \qquad 2\text{-}29$$

for some set of projection operators $\tilde{p}$. If the projection operators satisfy the bi-orthogonality condition,

$$\langle \tilde{p}_m | \tilde{\psi}_{m'} \rangle = \delta_{mm'} \qquad 2\text{-}30$$

Then the one-center expansion $\sum_m |\tilde{\psi}_m\rangle\langle \tilde{p}_m | \tilde{\psi}\rangle$ of the smooth function $\tilde{\psi}$ equals $\tilde{\psi}$ itself.

The requirement that the transformation in Equation (2-26) is linear leads to the following form for the operator τ

$$\tau = 1 + \sum_m \{|\psi_m\rangle - |\tilde{\psi}_m\rangle\}\langle \tilde{p}_m| \qquad 2\text{-}31$$

Furthermore, the expressions apply equally well to core and valence states so that one can derive all-electron results by applying the expressions to all the electron states. The general form of PAW s can be cast in terms of transformation by Equation (2-31). For

nay operator $\hat{A}$ in the original all-electron problem, one can introduce a transformed operator $\hat{A}$ that operates on the smooth part of the wavefunctions

$$\tilde{A} = \tau' \hat{A} \tau = \hat{A} + \sum_{mm'} |\tilde{p}_m\rangle \{\langle \psi_m | \hat{A} | \psi_{m'} \rangle - \langle \tilde{\psi}_m | \hat{A} | \tilde{\psi}_{m'} \rangle\} \langle \tilde{p}_{m'}| \qquad 2\text{-}32$$

One can add an operator of the form in the right hand side

$$\hat{B} - \sum_{mm'} |\tilde{p}_m\rangle \langle \tilde{\psi}_m | \hat{B} | \tilde{\psi}_{m'} \rangle \langle \tilde{p}_{m'}| \qquad 2\text{-}33$$

with no change in the expectation values. For example, one can remove Coulomb singularity for the smooth function, leaving a term that can be dealt with in the radial about each nucleolus. Now the physical quantities can be obtained from Equations (2-31) and (2-32). For example, the charge density is given by Equation (2-34)

$$\rho(r) = \tilde{\rho}(r) + \rho^1(r) - \tilde{\rho}^1(r) \qquad 2\text{-}34$$

which can be written in terms of eigenstates labeled *i* with occupancy f_i as

$$\tilde{\rho}(r) = \sum_i f_i |\tilde{\psi}_i(r)|^2 \qquad 2\text{-}35$$

$$\rho^1(r) = \sum_i f_i \sum_{mm'} \langle \tilde{\psi}_i | \tilde{\psi}_m \rangle \psi^*_m(r) \psi_{m'}(r) \langle \tilde{\psi}_{m'} | \tilde{\psi}_i \rangle \qquad 2\text{-}36$$

and

$$\tilde{\rho}^1(r) = \sum_i f_i \sum_{mm'} \langle \tilde{\psi}_i | \tilde{\psi}_m \rangle \tilde{\psi}^*_m(r) \tilde{\psi}_{m'}(r) \langle \tilde{\psi}_{m'} | \tilde{\psi}_i \rangle \qquad 2\text{-}37$$

Similarly, the energy functionals can be written as

$$E = \tilde{E} + E^1 - \tilde{E}^1 \qquad 2\text{-}38$$

The last two terms $\rho^1(r)$ and $\tilde{\rho}^1(r)$ are localized around each atom and the integrals can be done in spherical co-ordinates with no problems from the string variables near the nucleus. They contain contributions from the core and smooth core states, respectively.

In practice, the smooth core density is constructed instead of constructing a smooth core state for each core state individually unless one is interested in the physical properties that are related to the core states.

2.3. The Vienna ab-initio simulation package

The Vienna *ab-initio* simulation package (VASP)[18, 26, 27] is used to perform first-principles total-energy calculations within the density functional theory. The VASP simulates the electronic and atomic structures of molecules and crystals. It uses ultrasoft pseudopotentials or the projector-augmented wave method and a plane wave basis set. The expression *ab initio* means that only first-principles are used in the simulations, no experimental data are needed. VASP has a large amount of settings and specifications in the database for tailoring the calculations for different systems. The inputs to the program are text-files of which the most important are: *INCAR*, *POSCAR*, *KPOINTS* and *POTCAR*. The *INCAR* file contains the basic instructions to VASP, such as which algorithm to use, what precision is required for the result, which way to relax the structure, (conjugate gradient, MD, etc.), energy cut-off for the plane waves, the E_{XC} approximation and much more. In the *POSCAR* file the size of the supercell is specified along with the positions of the atoms and, if relevant, initial velocities and constraints on movement. The *KPOINTS* file controls which *k*-point scheme to use and finally the *POTCAR* file contains the atomic mass and the ultrasoft pseudopotentials or PAW potentials for the relevant atoms and the chosen E_{XC} approximation from the database.

2.4. Direct method lattice dynamics and finite temperature thermodynamics

DFT is a non-empirical parameter method whose applications and predictive ability in different fields known for some time. But, the results we obtain from DFT are always at 0 K which may not be viable in practical applications. Hence combination of DFT with different techniques such as linear response method[28, 29] or direct methods[30-32] allows us to evaluate phonon dispersion curves without empirical parameters. In the direct method[33, 34], the forces are calculated *via* the Hellmann-Feynman theorem using DFT-derived total energies, assuming a finite range of interaction. The phonon spectra are then derived using Newton's equation of motion in lattice dynamics calculations.

$$\phi_{i,j}(n,\mu;m,\nu) = \left[\frac{\partial^2 E}{\partial R_i(n,\mu)\partial R_j(m,\nu)}\right] \quad 2\text{-}39$$

$$F_i(n,\mu) = \sum_{m,\nu,j} \phi_{i,j}(n,\mu;m,\nu) U_j(m,\nu) \quad 2\text{-}40$$

$$D(k;\mu,\nu) = \frac{1}{\sqrt{M_\mu M_\nu}} \sum_m \phi(0,\mu;m,\nu) e^{2\pi i k[R(0,\mu)-R(m,\nu)]} \quad 2\text{-}41$$

$$D(k).e(k,j) = \omega^2(k,j)e(k,j) \quad 2\text{-}42$$

$$g(\omega) = \frac{1}{nd\Delta\omega} \sum_{k,j} \delta_{\Delta\omega}(\omega - \omega(k,j)) \quad 2\text{-}43$$

$$\delta_{\Delta\omega}(x) = \begin{cases} 1 & if\ -\frac{\Delta\omega}{2} < x \le \frac{\Delta\omega}{2} \\ 0 & otherwise \end{cases} \quad 2\text{-}44$$

Where, $\phi_{i,j}(n,\mu;m,\nu)$ is force constant matrix, $F_i(n,\mu)$ is force due to atomic displacement U_j, d is the number of degree of freedom in the unit cell, $D(k;\mu,\nu)$ is called the dynamical matrix, $\omega^2(k,j)$ is called the phonon frequency which can be

obtained by solving the Newton and $g(\omega)$ is called the phonon density of states which is frequency distribution over normal modes. The partial phonon DOS can be calculated using the following:

$$g_{i,\mu}(\omega) = \frac{1}{nd\Delta\omega}\sum_{k,j}\left|e_i(k,j;\mu)\right|^2 \delta_{\Delta\omega}(\omega - \omega(k,j)) \qquad 2\text{-}45$$

Integrating phonon DOS we can calculate the vibrational internal energy and entropy as follow:

$$E_{i,\mu} = \frac{1}{2}d\int_0^\infty d\omega.g_{i,\mu}(\omega).(\hbar\omega).\coth(\frac{\hbar\omega}{2k_BT}) \qquad 2\text{-}46$$

$$E_{vib}(T) = \sum_{i,\mu} E_{i,\mu} \qquad 2\text{-}47$$

$$S_{i,\mu} = k_B d\int_0^\infty d\omega.g_{i,\mu}(\omega).\{(\frac{\hbar\omega}{2k_BT})[\coth(\frac{\hbar\omega}{2k_BT}) - 1] - \ln[1 - \exp(\frac{\hbar\omega}{2k_BT})]\} \qquad 2\text{-}48$$

$$S_{vib}(T) = \sum_{i,\mu} S_{i,\mu} \qquad 2\text{-}49$$

Where, a contribution from any atom μ and degree of freedom i to the internal energy and entropy are given by $E_{i,\mu}$ and $S_{i,\mu}$, respectively.

2.5. The PHONON package

For building the crystal the best is to use PHONON[35]. The supercell with a given space group can also be created using this. The supercell can be equal to the primitive unit cell of the crystal. Next, transfer the structural data (*POSCAR*) to an *ab initio* software, for example VASP, and minimize the system energy. The optimized lattice constants, and atomic positions are then reused by PHONON to create a large supercell, which will be used to calculate phonons spectra. Transfer the crystal data from

PHONON to VASP program and optimize again the large supercell. Usually it is sufficient to optimize the atomic positions only (in VASP ISIF=2). One should quickly reach the minimum, since the input structural data correspond already to the minimum. In VASP create a new *POSCAR* with atomic positions where one atom is displaced. For each configuration with displaced atom calculate the Hellmann-Feynman forces from a single minimization run of electronic subsystem only (NSW=1). The Hellmann-Feynman forces are then collected to a single file. Then import the generated Hellmann-Feynman file to PHONON, and calculate phonon dispersion curves, density of states, etc to calculate the finite temperature thermodynamic properties.

Chapter 3 - Experimental Approach

3.1. Experimental details

Starting precursor materials and various nano-catalytic dopants were obtained either from Sigma Aldrich or from QuantumSphere Inc., CA and they were used to synthesize and characterize our desired hydrogen storage materials without any further purification. High purity H_2 (99.9999%), N_2 (99.99%) and He (99.99%) were procured from Airgas for the synthesis and analytical measurements. All chemical reactions and operations were performed in a nitrogen filled glove box. Precursor materials with different stoichiometric mole ratio were mixed in a stainless steel bowl (80 ml) and the lid sealed with viton O-ring in the glove box. The bowl was then evacuated for 30 minutes to remove the residual oxygen and moisture down to *ppm* levels. A specially designed lid with an inlet and outlet valves were used for this purpose.

The mechano-chemical process employing high energy milling was carried out by Fritsch pulversette planetary mono mill, P6 in an inert atmosphere. The milling parameters, ball to powder weight ratio and milling speed were optimized to 20:1 and 300 rpm respectively. Milling duration was optimized for all the samples. These mechano-chemically processed complex hydrides were immediately transferred to the glove box for further characterizations. In a similar way, few mole concentrations of

nano-catalytic dopants such as nanoNi, nanoCo, nanoFe, etc. were added during the milling process for the synthesis of nanocatalyst doped complex borohydrides.

The B–H bond stretch/bending of the complex borohydrides system was measured using a Perkin-Elmer *Spectrum One* FTIR spectrometer. This instrument operates in a single-beam mode and is capable of data collection over a wave number range of 370–7800 cm^{-1} with a resolution of 0.5 cm^{-1}. The complex borohydrides samples were palletized and sealed in a specially designed KBr cell for infrared measurements.

The powder X-ray diffraction of the mechano-chemically milled complex hydride was carried out by the Philips X'pert diffractometer with CuK_α radiation of λ = 5.4060 Å. The incident and diffraction slit widths used for the measurements are 1^o and 2^o, respectively. The incident mask of 10 mm was used for all the samples and their XRD studies. The sample holder (zero background silicon disc of 32 mm diameter procured from the Gem Dugout, Pennsylvania, and USA) was covered with polyethylene tape (foil) with O-ring seal in a N_2 filled glove box to avoid the O_2/moisture pickup during the XRD measurements. Diffraction from the tape was calibrated without the actual sample and found to be occurring at the 2θ angles of 22^o and 24^o, respectively. The XRD phase identification and particle size calculation was carried out using the PANalytical X'pert Highscore software with built-in Scherer calculator.

The simultaneous DSC and TGA (SDT) analysis pertaining to the weight loss and the heat flow for the reaction enthalpy during thermal decomposition of undoped and nanomaterial doped complex hydrides were performed by using the TA instruments' SDT-Q600 analytical tool. Calibration of SDT was performed in four steps with empty

pan and standard sapphire disc. The four calibration subroutines of TGA weight, DTA baseline, DSC heat flow and temperature were carried out before an actual measurement on the sample. A pre-weighed sample was loaded into the ceramic pan and covered with the ceramic lid inside the glove box to prevent moisture from getting into the sample during transfer. A ramp rate of 2^{o}C/min was used for all the measurements. TA instruments' Universal Analysis 2000 software was used to analyze the TGA and DSC profiles.

The isothermal volumetric measurements were carried out by Hy-Energy's PCTPro 2000 sorption equipment. This fully automated Sievert's type instrument uses an internal PID controlled pressure regulator with maximum pressure of 170 bars. It also includes five built-in and calibrated reservoir volumes of 4.66, 11.61, 160.11, 1021.30 and 1169.80 ml. The volume calibration without and with the sample was performed at a constant temperature with an accuracy of $\pm 1^{o}$C using a helium gas. The software subroutines for hydrogen purging cycles, leak test, kinetics, PCT and cycling, etc. were performed by the HyDataV2.1 Lab-View program. The data collected from each run were analyzed using the Igor Pro 5.03 program with a built in HyAnalysis Macro.

Temperature programmed desorption (TPD) measurement was carried out by Autosorb-1 equipment of Quantachrome Instrument. A 100 to 120 mg amount of sample was loaded in the reactor and heated, in a 25 mL/min helium flow while heating from 25 to 200 °C at constant heating rate. The thermal desorption/reduction profiles were recorded and analyzed using TPRWIN software package.

The gas chromatography (GC) analysis was carried out during thermal programmed desorption process for both undoped and nanocatalyst doped samples. The

gas sample was injected (less than 50-100 micro liter) in to the TCD detector and recorded the GC signal over a period of retention time. The gas analysis and plotting of the curves were carried out by Saturnview Version 5.52 software.

3.2. Thermo analytical tools/techniques

3.2.1. Differential scanning calorimetry

The differential scanning calorimetry (DSC) is a thermal analysis tool and it measures the difference in the amount of heat required to increase the temperature of a sample with respect to an inert reference as a function of time and temperature.

The specific Q10 differential scanning calorimeter manufactured by TA instruments consists of two closed pans, one is for the sample and the other is working as a reference pan (which is generally an empty) inside a helium filled chamber at 50-70 psi gas pressure. Figure 3-1 shows the DSC Q10 apparatus. The heat flow difference between the two pans is monitored while they are heated, or cooled, uniformly. This can be done at a constant temperature (isothermally) or at a constant temperature rate (ramp).

Figure 3-1. Differential scanning calorimetry (DSC) Q10 apparatus

The basic working principle in this tool/technique is that, when the sample undergoes a physical transformation such as phase transitions, an extra amount of heat is required/withdrawn to/from the sample pan to maintain both the pans at the same temperature. The process can be exothermic or endothermic depending on the characteristics of the sample. Some examples of endothermic processes are glass transition, melting, evaporation, etc. and some exothermic examples are crystallization, oxidation, etc.

3.2.2. Thermo gravimetric analysis

Thermo gravimetric analysis (TGA) is also a thermal analysis tool which uses heat as an external force to occur chemical reactions or/and physical changes in the materials under investigation. TGA measures the amount and rate of change in the weight of a material due to dehydration, decomposition, and oxidation as a function of temperature or time in a controlled atmosphere. Molecular structure gives characteristic thermo gravimetric curves for specific materials due to unique sequence from physicochemical reactions occurring over specific temperature ranges and heating rates.
The specific TGA used in our work is the Q600 series; it gives an accurate measurement of simultaneous DSC-TGA (SDT) of the same sample. A matched Platinum/Platinum-Rhodium thermocouple pair embedded in the ceramic beams provides direct sample, reference, and differential temperature measurement and a dual balance mechanism gives an accurate weight loss/gain measurement. The schematic cross-sectional diagram of Q600 SDT[36] is shown in Figure 3-2.

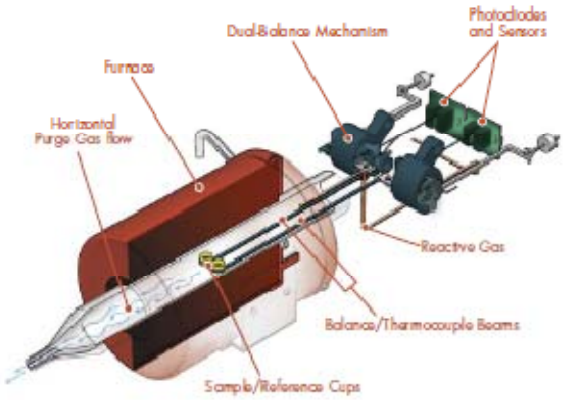

Figure 3-2. Schematic diagram of Q600 balance/furnace[36]

The balance operates based on a null-balance principle. At the zero position, equal amounts of light shine on the two photodiodes. If the balance moves out of the null position an unequal amount of light shines on the two photodiodes. A certain amount of current is then applied to the meter to return the balance to the zero position. The amount of applied current is proportional to the weight loss or gain.

3.2.3. Thermal programmed desorption autosorb-1

Temperature programmed desorption (TPD) is a technique in which the amount of desorption/reaction is monitored as a function of temperature. The temperature is raised in a linear fashion so that a suitable detection system can record a characteristic desorption/reaction profile of the sample being tested. A high sensitive thermal conductivity detector (TCD) is used to monitor the process. The TCD signal is also proportional to the quantity of desorbed gas molecules as the thermal energy overcomes the binding energy.

In Figure 3-3 shows the basic schematic diagram[37] of the TPD Autosorb-1 equipment manufactured by Quantachrome Instruments.

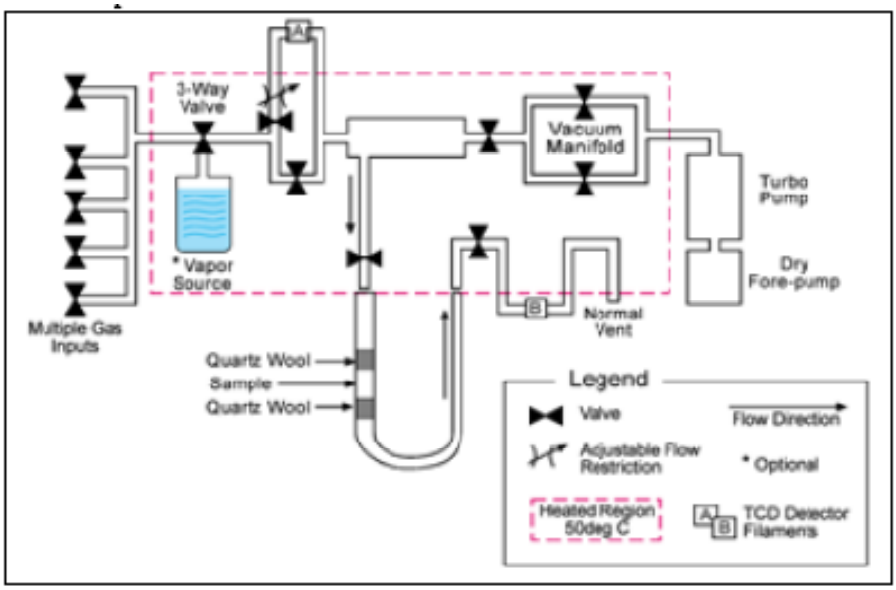

Figure 3-3. Schematic diagrams of the autosorb-1 TPD/TPR apparatus[37]

The sample between two quartz wool pieces is purged with nitrogen/He in order to avoid O_2 in the sample and inside the lines, then for the TPR measurement, a mixture of 95% Ar and 5% H_2 flows over the sample with a temperature ramping, a monitoring process records the amount of hydrogen absorbed based on the signal in the B TCD detector filament and compared with the A TCD filament. For the TPD measurement, the hydrogen mixture is replaced by an inert gas and the TCD is changed to TPD option. An amount of 100 to 120 mg of sample was loaded in the reactor and heated, in a 25 mL/min helium flow while heating from 25 to 200 °C at constant ramping and then the thermal desorption/reduction profiles were recorded and analyzed using TPRWIN software package.

3.2.4. Pressure composition temperature apparatus

The instrument used is the PCTPro-2000 manufactured by Hy-Energy, USA. This fully automated Sievert's type instrument uses an internal PID controlled pressure regulator with maximum pressure of 170 bars. It also includes five built-in and calibrated reservoir volumes of 4.66, 11.61, 160.11, 1021.30 and 1169.80 ml. The equipment is designed to measure absorption/desorption behavior of the complex hydrides. Important measurements can be done with this instrument; they are pressure composition temperature (PCT), absorption/desorption kinetics, cycle-life, etc.

In the Sievert's technique, a calibrated reference volume at a constant temperature is filled with hydrogen gas to a measured pressure and then opened to the sample chamber; the gas uptake by the sample is calculated from the change in the hydrogen gas pressure in the system. Hydrogen uptake is represented by the hydrogen-to host atomic ratio, H/X, by analogy with the hydrogen-to-metal ratio for a metal, H/M. Similarly, the gas release by the sample is measured from the gas pressure difference in the system. The helium bottle (purity 99.9999%) is used for calibrating the volume and for purging the line from air. The Sievert's type volumetric hydrogen sorption system[38] is shown in Figure 3-4, where Res 1 and Res 2 are the gas reservoirs.

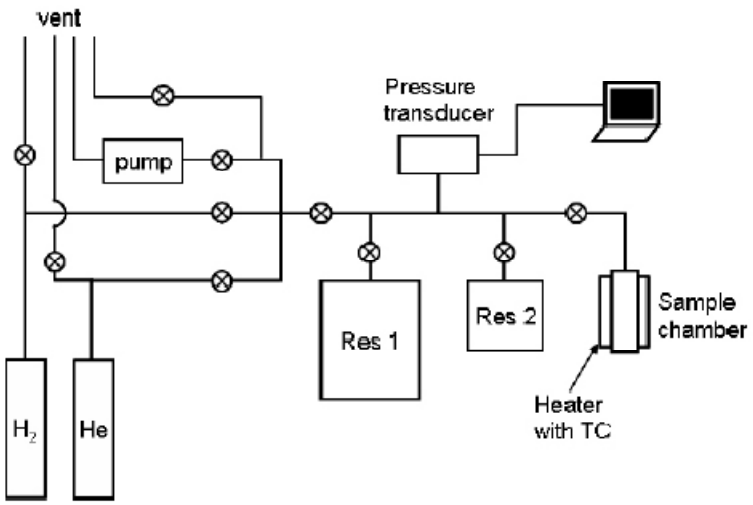

Figure 3-4. Schematic diagrams of Sievert's type volumetric apparatus[38]

3.3. Chemical analytical tools/techniques

3.3.1. Fourier transform infrared spectrometer

Infrared (IR) spectroscopy is a chemical analytical technique, which measures the infrared intensity versus wavelength of light. Infrared spectroscopy detects the vibration characteristics of chemical functional groups in a sample. Chemical bonds in the matter may stretch, contract and bend when an infrared light interacts with it. As a result, a chemical functional group tends to adsorb infrared radiation in a specific wavenumber (frequency) range regardless of the structure of the rest of the molecule.

In a Fourier transform infrared spectrometer (FTIR), the light passes through an interferometer which creates constructive and destructive interference pattern of two light beams, the recombined beam passes through the sample. The sample absorbs all the different wavelength characteristics of its spectrum depending on functional groups, and this subtracts specific wavelengths from the interferometer. The detector now detects

variation in energy versus time for all wavelengths simultaneously[39]. A Perkin-Elmer Spectrum One FTIR Spectrometer is shown in Figure 3-5.

Figure 3-5. Perkin-Elmer spectrum one FTIR spectrometer

Determining these frequencies allows us to identify the chemical fingerprint of the sample, since chemical functional groups are known to absorb radiation at specific frequencies. The intensity of the absorption light is related to the concentration of the component. Intensity and frequency of absorption by the sample are depicted in a two-dimensional plot called a spectrum. Intensity is generally reported in terms of percent transmittance, the amount of light that passes through it.

3.3.2. X-ray diffractometer

X-ray diffraction (XRD) is an efficient analytical technique used to characterize and identify unknown crystalline materials. Monochromatic X-rays are used to determine the interplanar distances of the unknown materials. With this technique the samples are analyzed as powders with grains in random orientations to ensure that all crystallographic directions are "sampled" by the beam. The basic principle of operation

of the XRD spectrometer is based on Bragg's law. When the Bragg conditions for constructive interference are obtained, a "reflection" is produced, and the relative peak height is generally proportional to the number of grains in a preferred orientation.

A Philips X'Pert XRD system is shown in Figure 3-6, it consists a source of monochromatic radiation and an X-ray detector which is situated on the circumference of a graduated circle centered on the powder sample, a detector and sample holder are mechanically coupled with a goniometer in such a way that a rotation of the sample holder through θ degrees occurs in conjunction with the rotation of the detector through θ degrees, a fixed 1:2 ratio. Divergent slits, placed between the X-ray source and the specimen, and between the sample and the detector, limit scattered (non-diffracted) radiation, reduce background noise, and collimate the radiation.

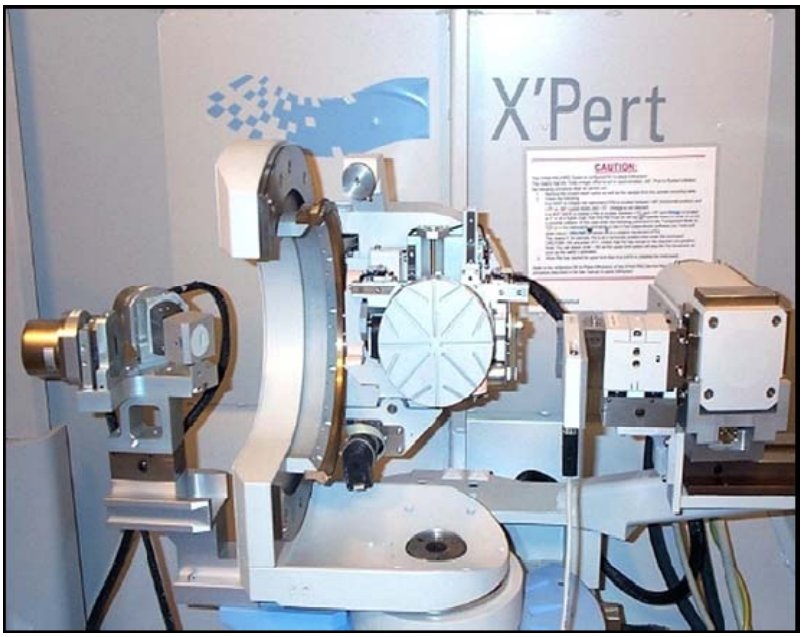

Figure 3-6. The Philips X'Pert XRD system

3.3.3. Scanning electron microscope

Scanning electron microscopy is a technique by which one can get topography, morphology, compositions and crystallographic information of an object. The scanning electron microscope (SEM) uses electrons rather than light to form an image. The Hitachi S800 scanning electron microscope used in the present study is limited to magnifications of around 3,000k.

The SEM uses the secondary electrons to form the image of the surface of the specimen since they do not diffuse much inside the specimen. In Figure 3-7 shows the details of interaction between an electron beam and specimen.

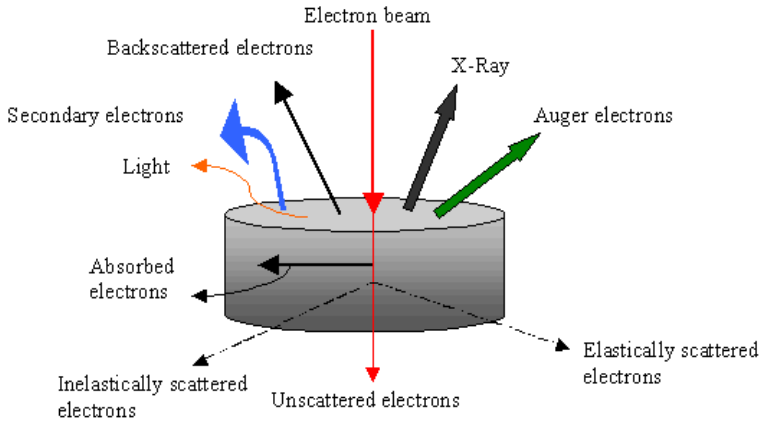

Figure 3-7. Electron beam and specimen interaction signals[40]

The schematic basic diagram of the operation of the Hitachi S800 SEM is show in Figure 3-8. Electrons beams come from an electron gun filament targeted at the specimen inside a vacuum chamber. That beam is collimated by electromagnetic condenser lenses, focused by an objective lens and then swept across the specimen at high speed. The secondary electrons are detected by a scintillation material which

produces electron flash lights. The flash lights are then detected and amplified by a photomultiplier tube.

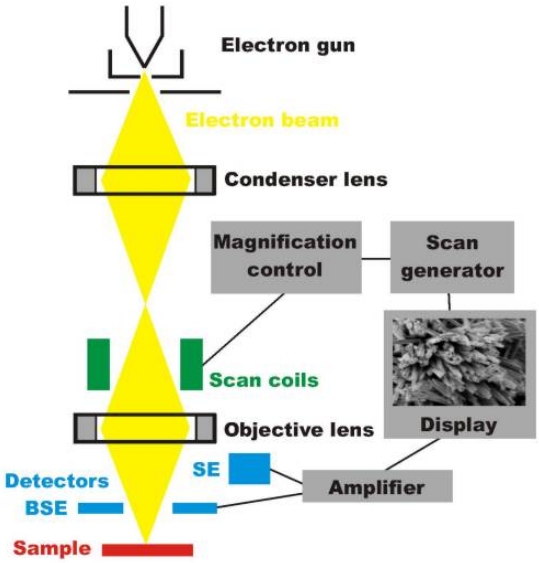

Figure 3-8. Schematic working principle diagram for a SEM[41]

3.3.4. Energy dispersive X-ray spectroscopy

Energy dispersive X-ray spectroscopy (EDS) is a technique used to identify the elemental composition of a sample or a section of interest within the sample for all elements with an atomic number greater than boron (B). When the electron beams of the SEM hits the surface of the sample, it produces X-ray fluorescence from the atoms in its path. The energy of each X-ray is the characteristic of each element which produces it. The EDS microanalysis system collects all the X-rays, sorts and plots them by energy level, and automatically identifies and labels the elements which are responsible for the peaks in those energy distributions. The detector cooled *via* liquid nitrogen is used to capture and mapped the X-ray counts continuously.

3.3.5. Gas chromatography

Gas chromatography (GC) is a technique which is used for common chemical confirmation test. GC analysis separates all of the components in a sample and provides a representative spectral output corresponding to each component. There is a carrier gas is used in this technique, which carry the component through a long column. The time elapsed between injection and elution is called the "retention time." This retention time can help to differentiate between some compounds. By changing the carrier gas flow rate and the temperature, the retention time can also be altered.

Chapter 4 - First-Principles Investigation Of The $Zn(BH_4)_2$

4.1. Abstract

First-principles calculations were performed on $Zn(BH_4)_2$ using density functional theory (DFT) within the local density approximation (LDA) and the projected augmented wave (PAW) method. $Zn(BH_4)_2$ is a promising candidate for hydrogen storage with a capacity of 8.5 wt%. A direct method lattice dynamics approach using *ab initio* force constants was utilized to calculate the phonon dispersion curves. This allowed us to establish stability of the crystal structure at finite temperatures. DFT was used to calculate electronic properties and the direct method lattice dynamics was used to calculate the finite temperature thermal properties. $Zn(BH_4)_2$ is found to have an orthorhombic structure in the space group of $Pmc2_1$ with lattice parameters a = 4.118 Å, b = 4.864 Å, c = 7.916 Å. It is an insulating material having a DFT-calculated band gap of 3.529 eV. Analysis of the electronic structure shows strong bonding between hydrogen atoms and boron in the $[BH_4]^-$ complex and also less polar bonding between the Zn and the hydrogen atom. The reaction enthalpy was calculated for the reaction $Zn(BH_4)_2 = Zn + 2B + 4H_2(g)$ to be 76.91 kJ/mol of H_2 at 0 K without any zero point energy correction, and 59.90 kJ/mol of H_2 including the zero point energy correction. The simulated standard enthalpy of formation for the complex $Zn(BH_4)_2$ was found to be -66.003 kJ/mol of H_2 at 300 K. This suggests that the crystal structure of $Zn(BH_4)_2$ is

stable at room temperature and this complex hydride can thus be considered a potential candidate for hydrogen storage.

4.2. Introduction

A recent challenge in hydrogen storage is to find light weight complex solid hydrides which have higher gravimetric system capacity greater than 6.5 wt % for on-board vehicular applications. The technical challenge is to find materials that can exhibit favorable thermodynamics and kinetics for hydrogen de-sorption and absorption, and have the ability to store a sufficient amount of hydrogen by weight as well as by volume percent. Borohydride complexes as hydrogen storage materials have recently attracted great interest. The stabilities of borohydrides have been studied using first-principles calculations. Some researchers have reported that alkali borohydrides are too stable for hydrogen storage[42, 43]. Lithium borohydride ($LiBH_4$) possesses a theoretical hydrogen capacity of ~18.3 wt. %, exhibiting potential promise for on-board applications. However, hydrogen decomposition from $LiBH_4$ starts at an elevated temperature of 380 °C and, also, this compound shows little or no reversible hydrogenation behavior. It has been reported that catalytically doping with SiO_2 lowers this temperature of hydrogen evolution to 300 °C[44]. A systematic approach to study the phase stability of $LiBH_4$ based on *ab initio* calculations has been presented and four thermodynamically stable phases have been identified, including a new phase of *Cc* symmetry for the first time for $LiBH_4$[45]. A correlation has been reported between thermodynamic stability of metal borohydrides and Pauli electronegativity of the parent components using first principles calculations[46].

Most of the commonly known borohydrides are found to be unsuitable for on-board hydrogen storage applications. This is primarily attributable to the high stability resulting from very high decomposition temperatures or complete irreversibility of hydrogen desorption[47]. $Zn(BH_4)_2$ is considered a potential candidate for on-board applications as it has a very high theoretical hydrogen storage capacity of 8.5 wt% and a reasonably low decomposition temperature (85 ^oC)[48] compared to complex alkali borohydrides (greater than 300 ^oC).

Density functional theory (DFT) is at present considered to be a versatile and important tool to solve innovative research problems in metal-hydrogen interactions and associated mechanisms. Successful application of DFT to a materials problem involves three distinct steps; (i) translation of the engineering problem to a computable atomistic model, (ii) computation of the required physicochemical properties, and (iii) validation of the simulation results by comparison with laboratory experiments[49]. Lattice dynamics[50, 51] using a direct force constant method helps one complete the picture by allowing for calculation of the finite temperature thermodynamic properties. Recently, in hydrogen storage materials research, DFT calculations have been employed to understand and validate the catalytic behavior of Ti- species on the dehydrogenation of $NaAlH_4$ clusters[52-54]. Crystal structure stability and electronic structure for storing high hydrogen content in light weight complex hydrides[55, 56] have been reported on the basis of DFT calculations.

Although $Zn(BH_4)_2$ is a potential candidate for hydrogen storage, very little is known about its structural and thermodynamic properties. In this study, we performed *ab initio* DFT calculations to establish the 0 K crystal structure and electronic structure. We

then performed lattice dynamics calculations[32] to determine the finite temperature reaction enthalpy of $Zn(BH_4)_2$. We employed the criterion that $\omega^2 > 0$ from the phonon frequencies to establish finite-temperature stability of the crystal structure determined from DFT calculations.

The standard enthalpy of formation is an important predictor of decomposition temperature for the decomposition reaction with its associated standard thermodynamic parameters. For a complex hydride, when the material is being heated, the effect of standard entropy starts dominating the standard enthalpy and at the decomposition temperature and constant pressure the standard Gibbs energy is zero. As during heating the entropy change of solid materials is very small compared to the gas, we can consider that the entropy change during the decomposition reaction is primarily due to H_2 evolution. Now at standard pressure and temperature for the most simple metal hydride, $\Delta S \approx \Delta S(H_2)$ = 130.7 J/mol K[57] which suggests that, for a simple hydride, the enthalpy of decomposition at room temperature (300 K) and 1 bar pressure is about 39 kJ/mol of H_2. For complex metal hydride materials it has been suggested that if the enthalpy of reaction is between 30 and 60 kJ/mol of H_2,[58] we can expect the complex metal hydride to be reversible for hydrogen storage.

We extended our theoretical calculations to identify the most favorable dehydrogenation reaction for $Zn(BH_4)_2$ by calculating the reaction enthalpies of different decomposition reactions. We expect that upon heating, $Zn(BH_4)_2$ releases hydrogen according to the following reaction during decomposition:

$$Zn(BH_4)_2 \rightarrow Zn + 2B + 4H_2(g) \qquad 4\text{-}1$$

Other possible different decomposition reactions are given in Equations (4-1*a*)-(4-1*d*). Formation reactions for the decomposition products are given in Equations (4-2) and (4-3). Formation enthalpy is one good way to establish whether theoretically predicted phases are likely to be stable. Such results are also expected to guide us discover convenient synthesis routes.

$$Zn(BH_4)_2 \rightarrow Zn + B_2H_6 + H_2 \qquad 4\text{-}1a$$

$$Zn(BH_4)_2 \rightarrow ZnH_2 + 2B + 3H_2 \qquad 4\text{-}1b$$

$$Zn(BH_4)_2 \rightarrow \frac{1}{2}ZnH_2 + \frac{1}{2}Zn + 2B + \frac{7}{2}H_2 \qquad 4\text{-}1c$$

$$Zn(BH_4)_2 \rightarrow ZnH_2 + B_2H_6 \qquad 4\text{-}1d$$

$$2B + 3H_2 \rightarrow B_2H_6 \qquad 4\text{-}2$$

$$Zn + H_2 \rightarrow ZnH_2 \qquad 4\text{-}3$$

4.3. Computational methods

4.3.1. Ab initio

First-principle calculations were performed on $Zn(BH_4)_2$ using DFT within the local density approximation (LDA)[59] and projected augmented wave (PAW)[25, 60] method utilizing a plane wave basis set to calculate the total energies, as implemented in the Vienna *Ab initio* Simulation Package (VASP)[18, 26, 27]. A $5\times5\times5$ Monkhorst-Pack[61] **k**-point mesh was used for sampling the Brillouin zone. A kinetic energy cutoff of 312 eV was used for $Zn(BH_4)_2$ for the plane wave basis set. For Zn, B, H_2 and B_2H_6, the same kinetic energy cutoff values as for $Zn(BH_4)_2$ were utilized, in the self consistent total energy (Table 4-1) calculations. This allows for the maximum cancellation of errors in the reaction enthalpy evaluation, which are calculated as small energy differences

between reactants and products (Table 4-2). The criterion for self-consistency in the electronic structure determination was that two consecutive total energies differed by less than 0.001 meV. The atomic positions and the lattice parameters, including the unit cell volume, were optimized by minimizing the forces and stresses until the residual forces between the atoms were within 1.0 meV/.Å

Table 4-1. Ground state energy, E in eV/mol of Zn, B and H_2 from DFT calculations

Element/ Compound	Space Group (number) / type	E (this work) (eV/unit-formula)	E (Literature) (eV/unit-formula)
Zn	*P63/mmc* (194) / hcp[62, 63]	-0.922	-1.02
H_2	*P63/mmc* (194) / hcp[64, 65]	-6.782	-6.792
α-B	*R-3m* (166) / trigonal[66, 67]	-6.678	-6.479

4.3.2. Direct method lattice dynamics

DFT is a non-empirical parameter method whose applications and predictive ability in different fields are known for some time. Combination of DFT with different techniques such as linear response method[28, 29] or direct methods[30-32] allows us to evaluate phonon dispersion curves without empirical parameters. Parlinski *et al.*[33, 34] developed the direct method where the forces are calculated *via* the Hellmann-Feynman theorem using DFT-derived total energies, assuming a finite range of interaction. The phonon spectra are then derived using Newton's equation of motion in the lattice dynamics calculations.

PHONON code[35], based on the harmonic approximation, as implemented within MOLEKEL was used to calculate the phonon spectra. Based on the optimized crystal structure, a supercell consisting of a large number of atoms depending on the type of unit cell was generated from the conventional cell. The interaction range is confined to the interior of the extended supercell and the force constants at and beyond this extended supercell can be neglected. The asymmetric atoms were displaced by +/- 0.02 Å. The dynamical matrix was obtained from the forces calculated *via* the Hellmann-Feynman theorem. This size of the supercell gives "exact" phonon frequencies at Γ, X, H, R Brillouin zone points in the dispersion curves.

4.4. Results and discussion

$Zn(BH_4)_2$ is a potential candidate for hydrogen storage but very little is known about the thermodynamics of this material. We expect that upon heating, $Zn(BH_4)_2$ releases hydrogen according to reaction (4-1) during decomposition. We calculated the enthalpy of reaction considering Equation (4-1) and based on the total energy calculation by combined DFT and direct method lattice dynamics using the following basic equation:

$$\Delta H = \sum_{\text{products}} E - \sum_{\text{reactants}} E \qquad 4\text{-}4$$

The total energies of $Zn(BH_4)_2$, Zn, B and H_2 were calculated by DFT to evaluate the enthalpy changes for reactions given above based on the following structures: different complex models listed in Table 4-2 for $Zn(BH_4)_2$, hcp for Zn (*P63/mmc*), trigonal for B (*R-3m*) and monoclinic for B_2H_6 ($P2_1/n$). We performed dimmer calculations to determine the optimum binding energy for H_2 molecule, for which we used the constant velocity MD simulation method in VASP. In these calculations, the inter-ionic distance

was increased by 0.01 Å per time step of 1 fs staring from 0.65 Å and ending at 0.88 Å. All the structures were optimized during the total energy calculations. The calculated ground state energies for each element are given in Table 4-1. The following sections discuss the stable crystal structures, electronic structure and finite temperature reaction enthalpy.

4.4.1. Crystal structure

The structure of zinc borohydride with the lowest enthalpy of formation was found to be of the $Mg(BH_4)_2$ type which has an orthorhombic structure in the space group of *Pmc2₁* (#26). No literature studies are available for the crystal structure of $Zn(BH_4)_2$ except a recent one by Nakamori *et al.*[46]. They have found that the crystal structure of $Zn(BH_4)_2$ is triclinic of space group *P-1* (#2) . They considered effective ionic radius of a $[BH_4]^-$ anion as 2.03 Å[68] which is close to the ionic radii of Br^- 1.96 Å and I^- 2.20 Å. In DFT calculations, they considered structures of MX_2 (X=Cl, Br and I; M=Mg, Zn, Hg and Cd) for $Zn(BH_4)_2$ to find the most stable crystal structure, as an ionic bonding exists between Zn^{++} cations and $[BH_4]^-$ anions in $Zn(BH_4)_2$. Most of the commonly known complex hydrogen storage materials which have the same formula unit as $Zn(BH_4)_2$ are given in Table 4-2. We started our calculations for the $Zn(BH_4)_2$ from these known complex models and included the zinc borohydride structure established by Nakamori *et al.*[46] We optimized the atomic positions and cell parameters for the $Zn(BH_4)_2$ for each basis model and finally optimized the cell volume against the total energy. After that we calculated the enthalpy of formation using Equation (4-4) for each model. Results from these calculations are shown in Table 4-2. Negative enthalpy of formation is indicative of a thermodynamically stable structure.

In our calculations, we found that the stable structures are *Pmc2$_1$, I4$_1$cd, Pbca, P-3, Fddd, P-1, P2/c and P-62m*. The highest negative enthalpy of formation (-76.91 kJ/mol of H_2) for $Zn(BH_4)_2$ was found for the space group *Pmc2$_1$* (i.e. $Mg(BH_4)_2$ model). Hence, we considered it to be the most stable structure of $Zn(BH_4)_2$ at 0 K. We found that the enthalpy of formation at 0 K for the *P-1* space group to be -16.73 kJ/mol of H_2 without zero point energy (ZPE) corrections, which suggests this space group is not the most stable structure.

Table 4-2. The enthalpy of formation (in kJ/mol of H_2) of $Zn(BH_4)_2$ from DFT for structures based on a similar chemical formula unit complex

Model	Z	Space Group (Number)	Type of unit cell	ΔH_{form} (0 K) kJ/mol H_2
$Ca(AlH_4)_2$	8	[69]*Pbca* (61)	Orthorhombic	-74.31
	2	[70]*P2$_1$/c* (14)	Monoclinic	14.10
	3	[70]*P-62m*(189)	Hexagonal	-6.36
	9	[70]*P-3* (147)	Trigonal	-68.83
$Mg(AlH_4)_2$	1	[71]*P-3m1* (164)	Trigonal	5.27
$Mg(BH_4)_2$	2	[46]*P2/c* (13)	Monoclinic	-16.63
	2	[56]*Pmc2$_1$* (26)	Orthorhombic	-76.91
$Zn(BH_4)_2$	2	[72]*P-1* (2)	Triclinic	-16.73
$Be(BH_4)_2$	16	[73]*I4$_1$cd* (110)	Tetragonal	-75.85
$Ca(BH_4)_2$	8	[43]*Fddd* (70)	Orthorhombic	-62.98

To establish finite temperature structural stability, we calculated the phonon spectra by the direct force constant lattice dynamics technique. The phonon spectra are shown in Figure 1.*a-h Pmc2$_1$, I4$_1$cd, Pbca, P-3, Fddd, P-1, P2/c* and *P-62m* space groups. We did not perform lattice dynamics calculations for space groups having positive enthalpy of formation without ZPE corrections as they are thermodynamically unstable. It can be seen from these dispersion curves that non-negative frequency distribution is present only for the *Pmc2$_1$* space group. This suggests that *Pmc2$_1$* space group (orthorhombic structure) is the stable structure for $Zn(BH_4)_2$ at finite temperatures. Only for this stable structure can acoustic and optical phonons be seen clearly in the dispersion curve.

The highest soft phonon mode for space group *P-1* was found to be *i*3.75 THz which suggests that the crystal for this phase group is unstable. This finding contradicts the results of Nakamori *et al.*[46]. They're not incorporating ZPE corrections and utilization of ultra soft pseudo potentials (versus our more accurate PAW potentials) are possible reasons for this discrepancy. The PAW potentials give better accuracy for 3-*d* metal hydrides[74]. It is observed that for the structure with the most negative formation enthalpy, the soft phonon modes vanish. The *I4$_1$cd , Pbca , P-3, Fddd, P2/c* and *P-62m* space groups showed the biggest soft modes of *i*1.667 THz, *i*3.415 THz, *i*8.75 THz, *i*36.063 THz, *i*20.25 THz and *i*12.25 THz respectively, along different high symmetry directions.

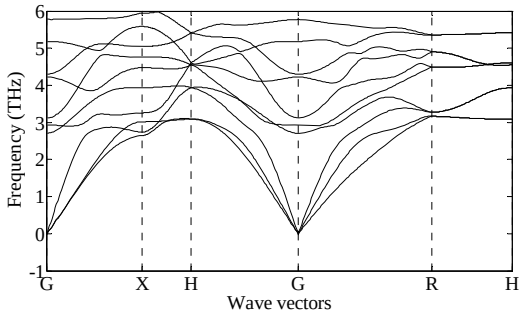
Frequency (THz)
6
5
4
3
2
1
0
-1
G
X
H
G
R
H
Wave vectors

(*a*)

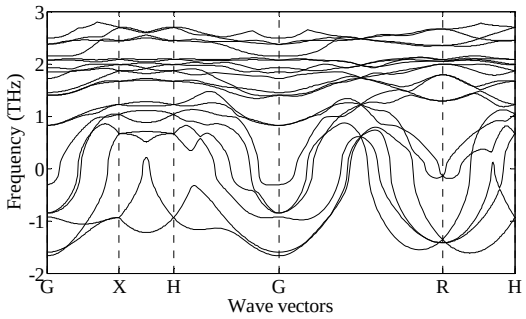
Frequency (THz)
3
2
1
0
-1
-2
G
X
H
G
R
H
Wave vectors

(*b*)

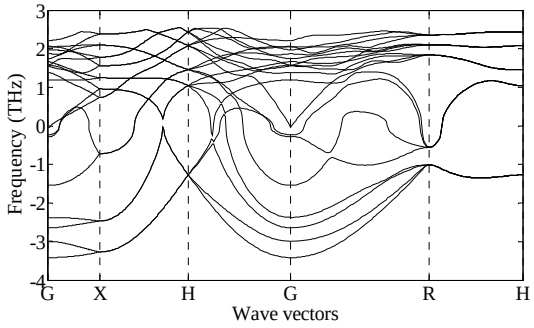
Frequency (THz)
3
2
1
0
-1
-2
-3
-4
G
X
H
G
R
H
Wave vectors

(*c*)

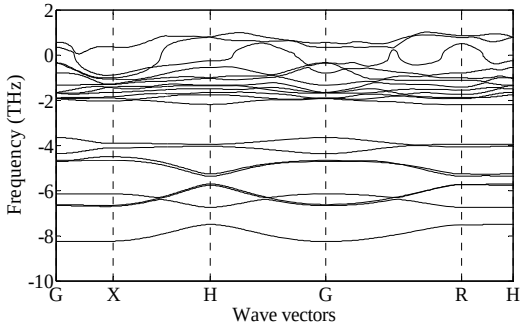
Frequency (THz)
2
0
-2
-4
-6
-8
-10
G
X
H
G
R
H
Wave vectors

(*d*)

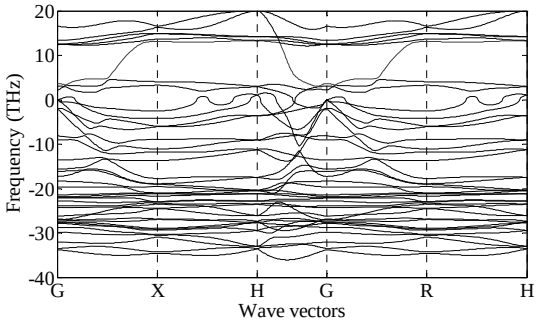
Frequency (THz)
20
10
0
-10
-20
-30
-40
G
X
H
G
R
H
Wave vectors

(*e*)

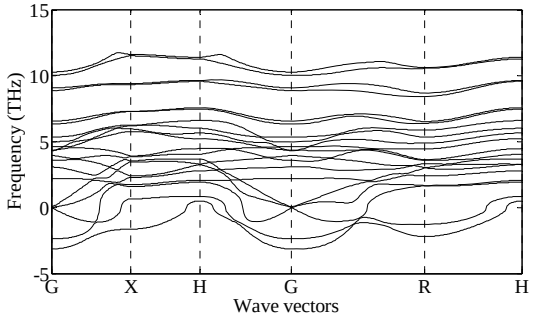
Frequency (THz)
15
10
5
0
-5
G
X
H
G
R
H
Wave vectors

(*f*)

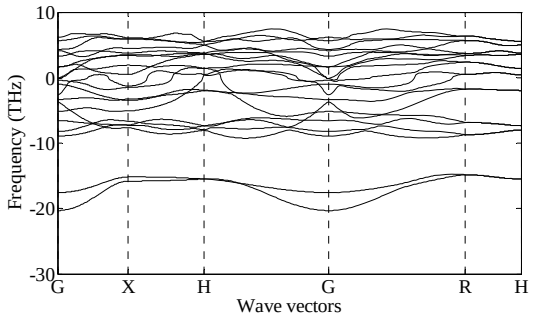

(*g*)

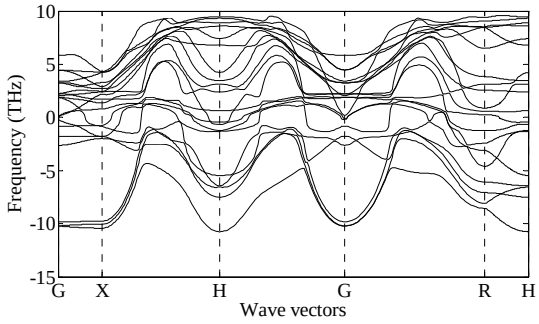

(*h*)

Figure 4-1. (*a-h)* Phonon dispersion relations of the *Pmc2₁*, *I4₁cd*, *Pbca*, *P-3*, *Fddd*, *P-1*, *P2/c* and *P-62m* space group structures of $Zn(BH_4)_2$. Coordinates of high-symmetry points are Γ(0,0,0) ≅ G(0,0,0), X(1/2,0,0), H(1/2,0,1/2), R(1/2,1/2,1/2)

Table 4-3. Optimized crystal structure of $Zn(BH_4)_2$. The space group is *Pmc2₁* (#26) with lattice parameters *a* = 4.118 Å, *b* = 4.864 Å, *c* = 7.916 Å. All the atomic positions are given by Wyckoff letter and the number of formula units in the unit cell *Z*=2

Element	Wyckoff letter	X	Y	Z
Zn	2*a*	0.00000	0.28459	0.00890
B1	2*b*	0.50000	-0.06481	0.47060
B2	2*a*	0.00000	-0.46194	0.24842
H1	2*b*	0.50000	-0.30735	0.42745
H2	4*c*	0.27449	-0.00500	-0.42983
H3	2*a*	0.00000	0.39706	0.37973
H4	2*a*	0.00000	0.21066	-0.24017
H5	4*c*	0.25820	-0.48360	-0.32151
H6	2*b*	0.50000	0.08396	0.34880

The minimum total energy for $Zn(BH_4)_2$ is -44.595 eV/mol at a unit cell volume of 150.82 $Å^3$ (considering the *Pmc2₁* to be the stable structure at finite temperatures). The optimized lattice parameters and atomic positions are given in Table 4-3. Figure 4-2 shows the optimized orthorhombic (*Pmc2₁*) crystal structure. Our calculations showed nearly tetrahedral shape of the BH_4 complex with B-H bond lengths d_{B-H} = 1.20-1.25 Å and H-B-H bond angles θ_{H-B-H} = 104.16-120°. Calculations of the phonon density of states (Figure 4-3) allowed us to determine finite temperature thermodynamic properties. The results are described in detail in a subsequent section.

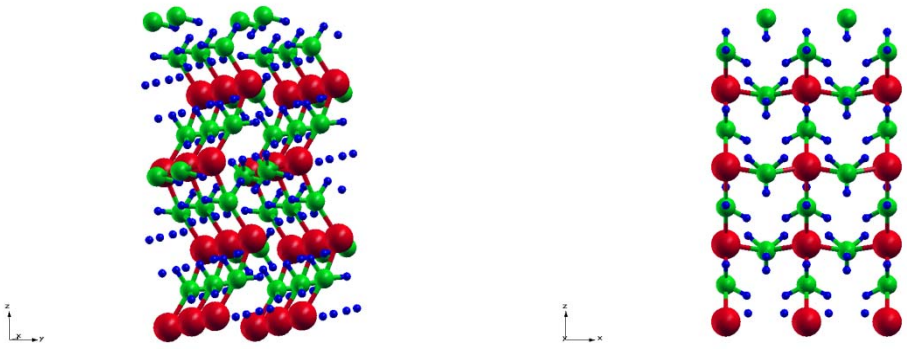

(*a*) (*b*)

Figure 4-2. Orthorhombic structure of space group *Pmc2₁* (#26) of $Zn(BH_4)_2$ (*a*) Proposed three-dimensional crystal structure and (*b*) Projected structure along [010] plane. (Red: Zn, Blue: H and Green: B atom)

In the phonon density of states, the phonon frequencies are classified into three groups. From the analysis of the eigenvectors, we found eigenmodes in the regions 25.75-39.75 THz and 65.75-76.75 THz which originate from internal B-H bending, and stretching vibrations in the $[BH_4]^-$ complex anion, respectively. These results compare

well with the experimental solid state FTIR analysis data (33.84 THz for B-H bending and 73.66 THz for B-H stretching)[48]. As can be seen from Figure 4-3, the librational frequencies (<22.25 THz) that originate from the displacement of Zn^{++} and $[BH_4]^-$, are lower than the B-H bending and stretching modes of $[BH_4]^-$.

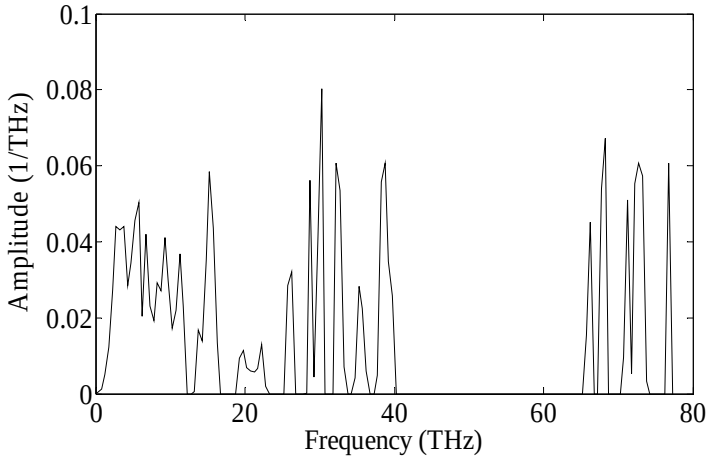

Figure 4-3. Total density of phonon states *g(w)* of $Zn(BH_4)_2$ in $Pmc2_1$ symmetry. Total phonon density of states is normalized as $\int g(w)dw = 1$

4.4.2. Electronic structure

The local and total electronic density of states (DOS) were calculated for the finite temperature stable crystal structure of $Zn(BH_4)_2$, *i.e.*, $Pmc2_1$, and are shown in Figures 4-4 and 4-5. From these figures, it can be seen that $Zn(BH_4)_2$ is an insulating material with a fundamental band gap of 3.529 eV. For $Mg(AlH_4)_2$ quasi particle GW corrections to DFT calculations give the actual excited state band gap of 6.5 eV[65], which is 2.4 eV higher than DFT-calculated band gap of 4.1 eV[71]. Hence, we expect our calculated band gap of 3.529 eV to also be an underestimation. From the total density of

states plot (Figure 4-4), it can be observed that there are three main valence bands and one conduction band. From the partial DOS plot (Figure 4-5), it can be seen that the lowest valence band is dominated by B 2*s* electrons and H 1*s* electrons with negligible contribution from Zn. The middle part of the valence band is mainly dominated by Zn 3*d* electrons. The upper valence band is occupied by B 2*p* electrons and H 1*s* electrons, with a small contribution from Zn 3*d* electrons. The valence band is dominated by B 2*s* and H 1s electrons that make a strong B-H bond. The conduction band is primarily dominated by B 2*p* electrons and to a lesser extent B 2*s* and Zn 4*s* electrons. Although H s electrons are prominent in the valence band small states are also found in the conduction band, which may indicate charge transfer to H atoms.

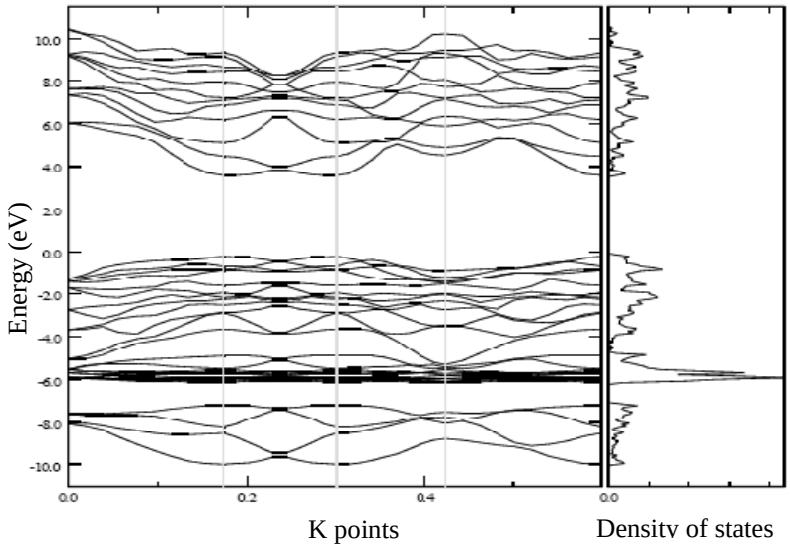

Figure 4-4. DFT/LDA electronic band structure and total density of states (DOS) of $Zn(BH_4)_2$ relative to Fermi level

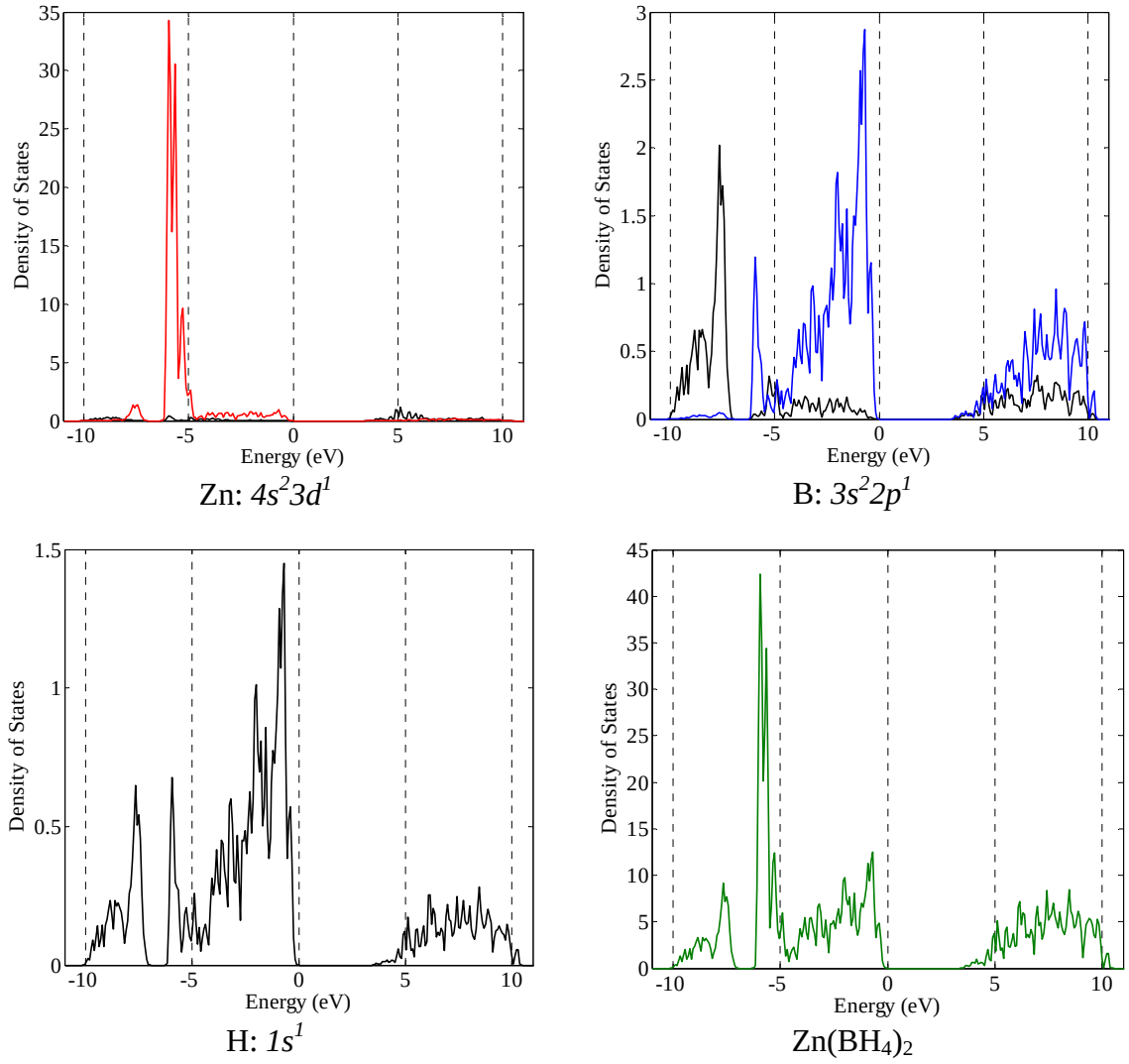

Figure 4-5. DFT/LDA electronic local/total density of state (DOS) relative to Fermi level for the most stable space group *Pmc2₁* (#26) is orthorhombic structure (black line for *s*, blue line for *p* and red line for *d* orbital)

The overall features of the DOS and PDOS, are different from those of $LiBH_4$[75], $NaBH_4$[68], KBH_4[68] and $Mg(BH_4)_2$[46]. The main difference is that the valence band has three parts for $Zn(BH_4)_2$ whereas the above mentioned borohydrides have two major parts in the valence band. This may be due to the presence of *d* electrons from the Zn atom.

However further investigations are required before providing more specific interpretations.

The Electron Localization Function (ELF)[76, 77] and charge density for the $Zn(BH_4)_2$ (100) plane were calculated for the space group $Pmc2_1$ to study the bonding between the atoms. ELF is associated with the probability density of finding two electrons in the same spin-state close to each other. It is a position-dependent function which varies between 0 and 1. An ELF value of 0.5 means a gas-electron like probability. The ELF calculated here (Figure 4-6) shows strong and large attractors around the H atoms. Hydrogen has no core attractor, thus this indicates either a shared-electron or a closed-shell bond. The very low ELF value on the B sites indicates delocalized electrons, while a spherical shell attractor is seen around Zn. The very low ELF value between Zn and $[BH_4]^-$ complex indicates the low ionic bond. Whereas, a very high value of ELF within the $[BH_4]^-$ complex indicates ionocovalent bonding. The plotted charge density (Figure 4-7) shows large densities centered around Zn which is segregated from B and H atoms. Some density is found around the H atom; however, it is significantly lower than around the Zn atom. Almost no charge density is seen around B. This also suggests that electrons are transferred to the H atom mostly from the B atom resulting in a strong B-H bond in the $[BH_4]^-$ complex with less polar bonding between the Zn and H atoms.

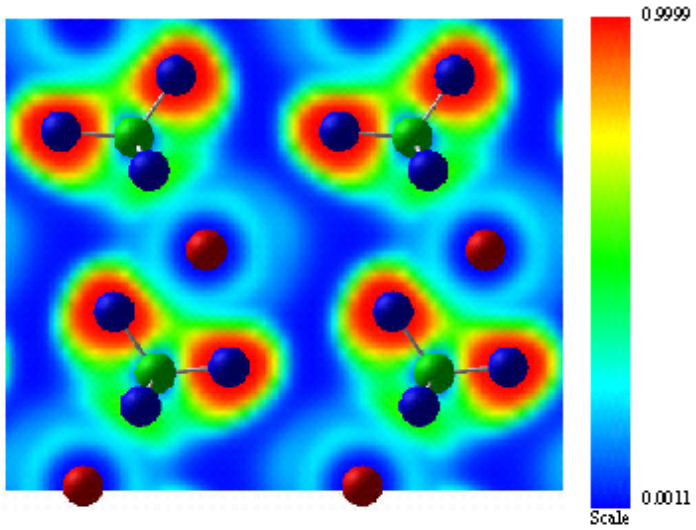

Figure 4-6. Electron localization function (ELF) of $Zn(BH_4)_2$ (100 plane) (Red: Zn, Blue: H and Green: B)

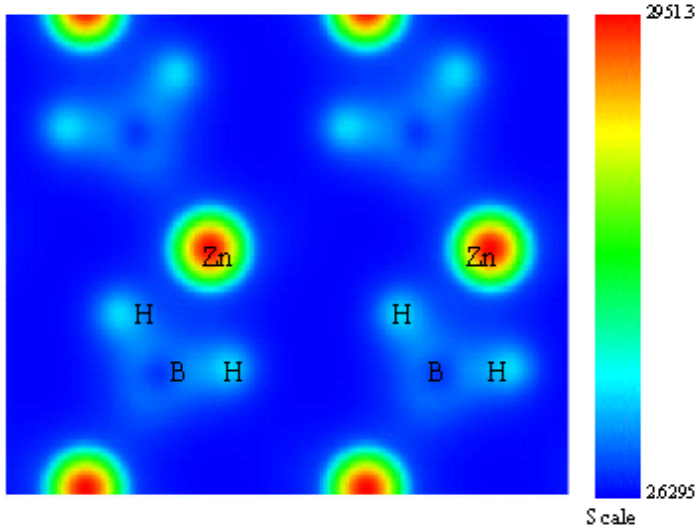

Figure 4-7. Charge density of $Zn(BH_4)_2$ (100 plane)

4.4.3. Finite Temperature Reaction Enthalpy

In the thermodynamic expression for the finite temperature enthalpy

$$H(T) = E(T) + PV \qquad 4\text{-}5$$

E(T) is the total internal energy which includes not only energies from DFT and ZPE (at 0 K) but also contributions from rotational, translational and vibrational (excluding ZPE) energies given in Equation (4-5*a*). We assumed that the rotational and translational energies are important for the gaseous phase only.

$$E = E_{DFT}(0\ K) + E_{ZPE}(0\ K) + E_{vib}(T) + E_{rot}(T) + E_{tran}(T) \qquad 4\text{-}5a$$

The enthalpy of formation is now given by Equation (4-6), as a sum of the absolute zero temperature part and the finite temperature part. The first part (Equation (4-6*a*)) includes the ground state energy and also the zero point vibrational energy which is independent of temperature. On the other hand, the finite temperature part (Equation (4-6*b*)) includes all the energies which are dependent on temperature, and is calculated using statistical mechanical theory.

$$\Delta H_{form}(T) = \Delta H^{0}(0\ K) + \delta\Delta H(T) \qquad 4\text{-}6$$

Where,

$$\Delta H^{0}(0\ K) = \Delta E_{DFT}(0\ K) + \Delta E_{ZPE}(0\ K) \qquad 4\text{-}6a$$

$$\Delta E_{DFT}(0\ K) = \sum_{products} E_{DFT}(0\ K) - \sum_{reactants} E_{DFT}(0\ K) \qquad 4\text{-}6a1$$

$$\Delta E_{ZPE}(0\ K) = \sum_{products} E_{ZPE}(0\ K) - \sum_{reactants} E_{ZPE}(0\ K) \qquad 4\text{-}6a2$$

and

$$\delta\Delta H(T) = \Delta E_{vib}(T) + \Delta E^{g}{}_{rot}(T) + \Delta E^{g}{}_{tran}(T) + \Delta(PV) \qquad 4\text{-}6b$$

$$\Delta E_{vib}(T) = \sum_{products} E_{vib}(T) - \sum_{reactants} E_{vib}(T) \quad \text{4-6}b1$$

$$\Delta E^{g}{}_{rot}(T) = \sum_{products} E^{g}_{rot}(T) - \sum_{reactants} E^{g}_{rot}(T) \quad \text{4-6}b2$$

$$\Delta E^{g}{}_{tran}(T) = \sum_{products} E^{g}_{tran}(T) - \sum_{reactants} E^{g}_{tran}(T) \quad \text{4-6}b3$$

For calculating $\delta\Delta H(T)$, as an example for the reaction given in Equation (4-1), we write (Equations ((4-7)-(4-9)):

$$\delta\Delta H(T) = E_{vib}^{Zn(BH_4)_2}(T) - E_{vib}^{Zn}(T) - 2E_{vib}^{B}(T) - 4\{E_{vib}^{H_2}(T) + E_{tran}^{H_2}(T) + E_{rot}^{H_2}(T) + PV\} \quad \text{4-7}$$

$$\delta\Delta H(T) = E_{vib}^{Zn(BH_4)_2}(T) - E_{vib}^{Zn}(T) - 2E_{vib}^{B}(T) - 4\{E_{vib}^{H_2}(T) + \frac{3}{2}k_BT + k_BT + k_BT\} \quad \text{4-8}$$

$$\delta\Delta H(T) = E_{vib}^{Zn(BH_4)_2}(T) - E_{vib}^{Zn}(T) - 2E_{vib}^{B}(T) - 4\{E_{vib}^{H_2}(T) + \frac{7}{2}k_BT\} \quad \text{4-9}$$

Equation (9) shows that we need to calculate the vibrational energy of the complex material $Zn(BH_4)_2$ and its elemental components to calculate the finite temperature reaction enthalpy. Vibrational energies in the above Equation 9 were calculated by integrating the phonon density of states over the Brillion zone. The results for the E_{ZPE} and E_{vib} (without ZPE) for different elements/compounds are given in Table 4-4.

Table 4-4. Zero point and vibrational energies of $Zn(BH_4)_2$ and its primary elements

Element/ Compd.	E_{ZPE} (kJ/f.u.) (literature)	E_{ZPE}(kJ/f.u.) (calculated)	E_{vib}(300 K) (kJ/f.u.) (incl. ZPE)	E_{vib}(300 K) (kJ/f.u.) (actual)
Zn	[78]1.0 (approx)	1.077	7.176	6.099
α-B	[79]12.5	12.478	13.65	1.172
H_2	[65]28.29, [80]27.08, [79]25.7	28.12	≈ 28.12	≈ 0.0
B_2H_6	[80]170.96	163.367	173.473	10.106
$Zn(BH_4)_2$		206.539	225.404	18.811

The enthalpy of formation of $Zn(BH_4)_2$ was found to be -76.91 kJ/mol of H_2 at 0 K (using Equation (4-6*a*1)) without the zero point energy corrections and -59.90 kJ/mol of H_2 including ZPE (using Equations ((4-6*a*) & (4-6*a*2))). We also found that the finite temperature reaction enthalpy for the dehydrogenation reaction (4-1) by using Equations (4-6) and (4-9) was 66.003 kJ/mol H_2 at 300 K or 264.012 kJ/mol of $Zn(BH_4)_2$. The *ab initio* theoretical formation enthalpy value of ZnH_2 (reaction (4-3)) from zinc and molecular hydrogen varies from 6.464 to 31.57 kJ/mol ZnH_2[81]. As very little is known about ZnH_2, we calculated the formation enthalpy of the ZnH_2 using fluorite type structure and it was found to be 23.66 kJ/mol ZnH_2 at 0 K in our calculations for the dehydrogenation reactions ((4-1*b*)-(4-1*d*)). For reaction (4-2), we calculated the formation enthalpy of diborane. It was found to be 25.38 kJ/mol of B_2H_6 at 0 K including zero point energy whereas the experimental standard enthalpy of formation is 36.00 kJ/mol of B_2H_6[82]. We defined the standard enthalpy of reaction, ΔH_{rxn} for the reaction (4-1*a*) as given below:

$$\Delta H_{rxn} = \Delta H^{0}_{form}(B_2H_6) - \Delta H^{0}_{form}(Zn(BH_4)_2) \qquad 4\text{-}10$$

Similar expressions were used for other reactions. Using the standard formation enthalpies of $Zn(BH_4)_2$, B_2H_6 and ZnH_2 we found ΔH_{rxn} for the reactions ((4-1*a*)-(4-1*d*)) to be 300.012, 287.672, 284.440 and 323.672 kJ/mol of $Zn(BH_4)_2$, respectively. Although H_2 is released from the liquid phase, we have not included the heat of fusion for the dehydrogenation reaction enthalpy. So we can expect the enthalpy of formation values calculated to be overestimated. As the enthalpy of dehydrogenation of $Zn(BH_4)_2$ for the reaction (4-1) is the lowest, this reaction may be expected to start first upon heating the complex borohydride. So this reaction can be predicted as the most favorable decomposition reaction. However, Jeon *et al.*[48] have found some evolution diborane experimentally, which indicates that reaction (1a) (36.00 kJ/mol higher enthalpy of dehydrogenation than reaction (4-1)) also occurs at the same time. The exact quantification and identification of the decomposed gaseous components at the decomposition temperature of $Zn(BH_4)_2$ is beyond the scope of this work. The main objective of the work in this section was to find the thermodynamically most favorable decomposition reaction.

4.5. Summary

In this work, we have predicted from theory the stability of the complex zinc borohydride structure. This required investigation of both the ground state energy by DFT and the lattice vibration energy by direct method lattice dynamics. We have calculated the structural stability of $Zn(BH_4)_2$ at $T > 0$ from structure-optimization calculations starting with 10 different very similar formula units for $Zn(BH_4)_2$. These calculations establish $Pmc2_1$ symmetry to be a new thermodynamically most stable

structure of $Zn(BH_4)_2$ at finite temperature. Our estimated value for the formation enthalpy of $Zn(BH_4)_2$ is -66.003 kJ/mol H_2 at 300 K which suggests that it should be possible to synthesize this phase. This finding suggests that the crystal structure is stable at room temperature and thus $Zn(BH_4)_2$ could be considered a potential candidate for hydrogen storage. The other thermodynamically stable structures in Table 4-2 which are *$I4_1cd$, Pbca, P-3* and *Fddd* symmetries, turn out to be unstable at finite temperatures with respect to lattice vibrations. From electronic structure calculations, ionic interaction between Zn and $[BH_4]^-$ and the strong ionocovalent B–H interaction within the $[BH_4]^-$ tetrahedral are revealed. Electronic density of states studies reveal that this phase has wide-band-gap of 3.529 eV which suggests that the $Zn(BH_4)_2$ is an insulator. Standard reaction enthalpy calculations reveal that decomposition to primary elements is the most favorable one. The findings of our work are in qualitative agreement with experimental results. Our study has given new insights into the thermodynamically most stable phase for the complex zinc borohydride. The methodology outlined in this work can be extended to studies on other complex hydrogen storage materials.

Chapter 5 - First-Principles Study Of Ni-Induced $Zn(BH_4)_2$

5.1. Abstract

Fundamental understanding of the role of Ni additives in promoting the dehydrogenation mechanism of hydrogen de-sorption in zinc borohydride ($Zn(BH_4)_2$) is a key factor for using this material in hydrogen storage. A systematic theoretical study of the energetics and hydrogen dynamics was carried out to understand this dehydrogenation mechanism. The energetic calculations reveal that Ni substitutes Zn in preference to B. H atoms are pulled towards these doped Ni atoms, which introduces instability *via* the breaking of multiple B-H bonds in the complex borohydride. The mechanistic understanding gained from this study can be applied to the design of better hydrogen storage materials.

5.2. Introduction

Hydrogen is considered to be the cleanest amongst the fuels available for onboard vehicular applications. The high operational cost of using liquid hydrogen and the low explosive limit (4%) of hydrogen in the gas phase makes its storage an important aspect for potential vehicular applications. The technical challenge is to find materials that exhibit favorable thermodynamics and kinetics for hydrogen de-sorption and absorption, and have sufficient gravimetric and volumetric storage capacity. $Zn(BH_4)_2$ is considered to be a potential candidate for on-board applications as it has very high theoretical

hydrogen storage capacity of 8.4 wt% and also reasonably low decomposition temperature compared to complex alkali borohydrides[47].

Improvement of the hydrogen ab- and de-sorption kinetics in complex hydrides is essential for these materials to be good reversible hydrogen storage media in the transportation sector. It has been reported that the addition of titanium-based compounds improves the kinetics significantly for $NaAlH_4$[52, 83, 84]. The role of 3-d transition metals in improving both dehydrogenation kinetics and thermodynamics of crystalline $NaAlH_4$ has been clearly explained by density functional theory (DFT) calculations[83, 85]. Calculations reveal that doped, destabilized metal hydride reaction systems are unstable with respect to phase separation at 0 K[86]. However, experimental results[87, 88] suggest that only Ni doping in $Zn(BH_4)_2$ reduces the de-hydrogenation temperature by approximately 20 °C, although physical understanding remains elusive. Thus, theoretical studies at the atomic scale are necessary to understand the role of Ni in lowering the hydrogen de-sorption temperature. Such understanding will allow for selection of appropriate dopants for complex metal hydride systems in general, achieving superior hydrogen storage properties.

5.3. Methodology

In this chapter, we provide results of a systematic study of the role of Ni in destabilizing the crystalline structure of $Zn(BH_4)_2$. For this, we calculate the vibrational density of states of hydrogen within the tetrahedral BH_4 complex nearest to the Ni dopant to show that it diminishes the hydrogen binding energy of the crystalline $Zn(BH_4)_2$ resulting in a decrease of the hydrogen decomposition temperature. The energy cost to remove hydrogen, and the hydrogen dynamics nearest to Ni (doped) and the

corresponding Zn (undoped) atom are calculated to understand the dehydrogenation mechanism in the crystalline material. We also show that Ni weakens the multiple B-H bonds, thus allowing the hydrogen to release at lower temperature.

We have utilized *ab initio* DFT methods to calculate the energetics and the direct force lattice dynamics approach to model gas-metal interactions at the atomic scale to gain useful insights into the effect of additives on $Zn(BH_4)_2$ structural behavior. Energetic calculations were performed using DFT within the local density approximation (LDA)[59] and projected augmented wave (PAW)[25, 60] method utilizing a plane wave basis set as implemented in the Vienna *Ab initio* Simulation Package (VASP)[18, 26, 27]. The atomic positions and the lattice parameters, including the unit cell volume, were optimized by minimizing the forces and stresses until the residual forces between the atoms were within 0.01 eV/Å.

We calculated vibrational density of states within the harmonic approximation. Combination of DFT with different techniques such as linear response method[28, 29] or direct methods[30-32] allows evaluation of the phonon dispersion curves without empirical parameters. Parlinski *et al*.[33, 34] have developed the direct method where the forces are calculated *via* the Hellmann-Feynman theorem using DFT-derived total energies, assuming a finite range of interaction. In this work, the PHONON code[35] was utilized to calculate the phonon spectra. Based on the optimized crystal structure, a supercell consisting of a large number of atoms depending on the type of unit cell was generated from the conventional unit cell.

We calculated the cohesive energy of Ni-doped $Zn(BH_4)_2$ (*i.e.* mixed complex hydrides $Zn_{16-n}Ni_nB_{32}H_{128}$ and $Zn_{16}B_{32-2n}Ni_{2n}H_{128}$, ($n$=1–4)) by considering the 2x2x2

supercell containing 16 $Zn(BH_4)_2$ formula units (176 atoms), and 1-4 of the units [a unit = $Zn(BH_4)_2$] Zn or B atoms were substituted with Ni atoms. The energy cost for hydrogen removal was computed by the $Zn_{16}B_{32}H_{127}$, $(Zn_{15}Ni)B_{32}H_{127}$ and $Zn_{16}(B_{30}Ni_2)H_{127}$ supercells.

5.4. Results and discussions

Using this methodology, we first investigated the possibility of Ni dissolution into zinc borohydride from calculations of energetics and cohesive energy, *i.e.* the energy required to break the atoms of the solid into isolated atomic species. Positive cohesive energy indicates a thermodynamically favorable structure. Results are shown in Figure 5-1. We also calculated the hydrogen atom removal energies for $Zn_{16}B_{32}H_{128}$, $(Zn_{15}Ni)B_{32}H_{128}$ and $Zn_{16}(B_{30}Ni_2)H_{128}$ supercells which were found to be 0.930 eV, 0.806 eV and 0.488 eV, respectively.

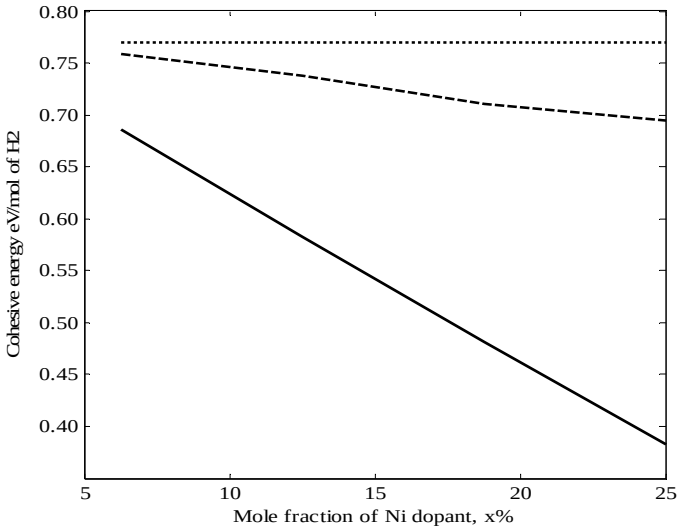

Figure 5-1. Cohesive energy of pure and Ni-substituted $Zn(BH_4)_2$. The dotted line is for pure $Zn(BH_4)_2$, the dashed line is for the case where Ni substitutes Zn and the solid line is for the case where Ni substitutes B

We found that substitution by Ni doping is energetically possible for both cases but pure borohydride is more stable than the doped systems. The results also suggested that the preferred substitution site for Ni is the Zn rather than the B site in the $Zn(BH_4)_2$ crystal lattice. This may be explained by the size effect: as Ni atomic radius (1.24 Å) is closer to the Zn atomic radius (1.34 Å) whereas the Ni atom is much bigger than the B atom (atomic radius 0.85 Å). Hence, energetically, it prefers the Zn site.

This size mismatch is also the cause for Ni substitution of B to be energetically less favorable. A relaxed crystal bonding analysis showed (Figure 5-2) that the bond lengths between Ni-H are 1.80 Å, 1.69 Å, 1.62 Å and 1.62 Å for the doped system. The corresponding Z-H bond distances are 2.0 Å, 1.86 Å, 1.84 Å and 1.84 Å for the pure system. B-H bond lengths for the pure system are 1.22 Å, 1.22 Å, 1.24 Å and 1.25 Å. The corresponding substitutional Ni-doped complex borohydride system, B-H bond distances are 1.25 Å, 1.25 Å, 1.29 Å and 1.32 Å. These results suggested that B-H bond lengths increase for substitutional Ni doped $Zn(BH_4)_2$ compared to those in pure $Zn(BH_4)_2$. The Ni atom pulls the H atoms towards itself from the nearest B atom and helps dehydrogenation by destabilizing the complex $Zn(BH_4)_2$.

These conclusions are also supported by calculations of the energy cost for hydrogen removal. We found that the hydrogen atom removal energy for $Zn_{16}B_{32}H_{128}$ supercell is higher than that for the $(Zn_{15}Ni)B_{32}H_{128}$ supercell by 0.124 eV, confirming that Ni doping does indeed weaken the B-H bonds.

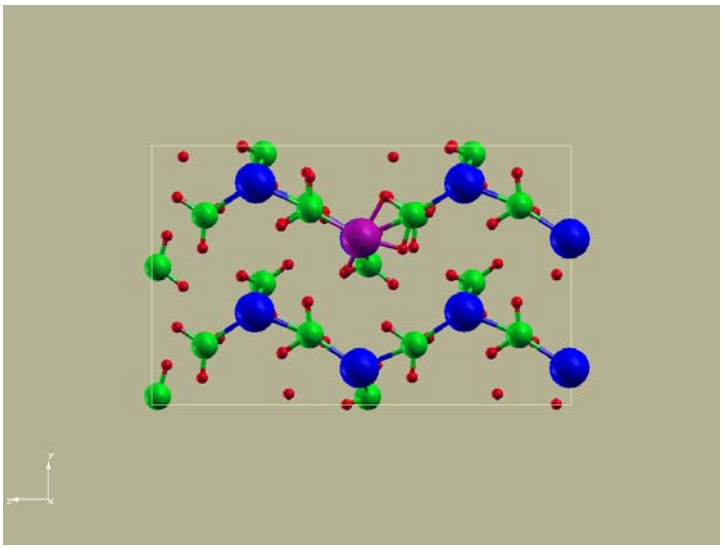

Figure 5-2. Relaxed structure of Ni doped $Zn(BH_4)_2$. Red ball corresponding to hydrogen, blue ball corresponding to zinc, green ball corresponding to boron and purple ball corresponding to nickel, respectively

Vibrational dynamical properties of the H atom in the BH_4 complex nearest to the Ni dopant could be used as local probes to understand the destabilization mechanism. We calculated these properties for the Ni substitution of Zn model as it is energetically favorable than substitution of B. We calculated the vibrational density of states using smaller supercell (88 atoms) structures than the supecells (176 atoms) used for energetic calculations. First, a $(Zn_3Ni)B_8H_{32}$ unit cell was generated and then a 1x2x1 supercell (88 atoms) was utilized in calculating the vibrational density of states for this Ni-doped system. This high dopant fraction (25%) unit cell/supercell was utilized to achieve a computationally viable system, and to stay within the limitations of the PHONON code, which allows a maximum of 62 non-equivalent displasive atoms.

From the dynamic studies, we find that for Ni substitution of Zn affects both low (libration) and high frequency (mainly bending) modes of vibrations of the BH_4 complex, as seen from the phonon density of states plots in Figure 5-3.

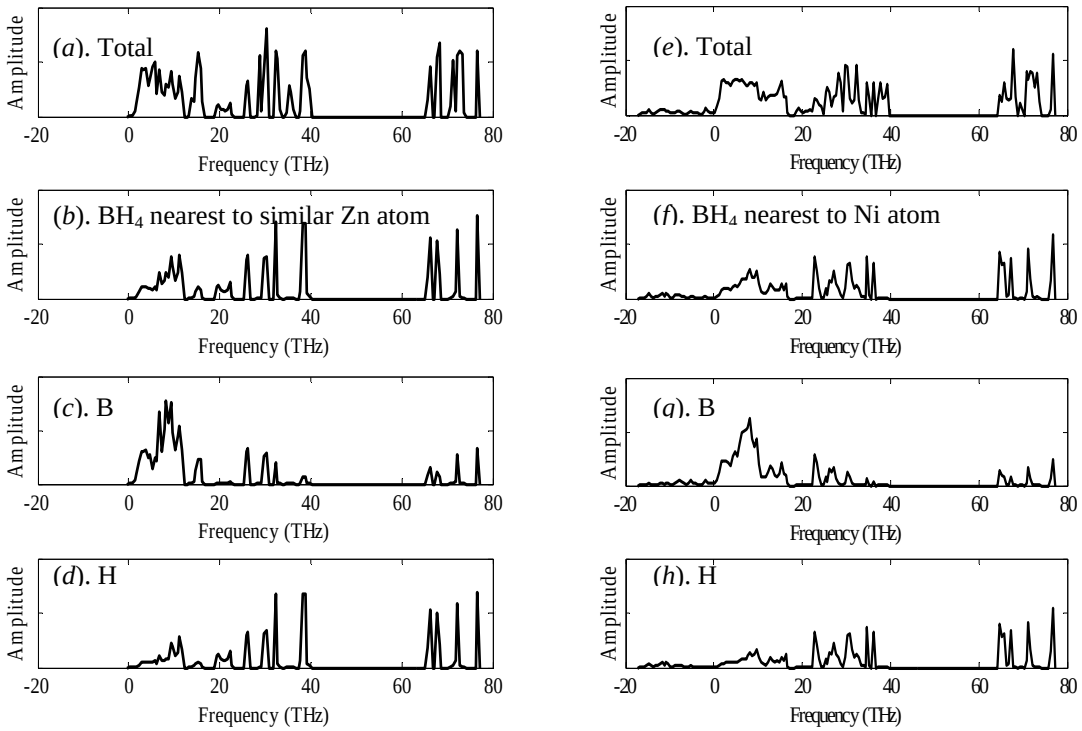

Figure 5-3. The total and partial phonon DOS for $Zn_8B_{16}H_{64}$ (panels *a*-*d*) and $Zn_6Ni_2B_{16}H_{64}$ (panels *e*-*h*). The specific atoms/groups for which the vibrational phonon densities of state are plotted are given within the figures

The small amplitude negative frequencies observed in the total and partial phonon DOS of $Zn_6Ni_2B_{16}H_{64}$ are indications of crystal instability at finite temperature as all phonon frequencies are required to be positive definite: $\omega^2 > 0$ for a stable crystalline structure. The modes that soften are mainly from both hydrogen and B displacements

nearest to the Ni dopant in the complex. These soften all modes and introduce instability in the lattice, thus improving dehydrogenation reactions.

5.5. Summary

To summarize this work, we have studied the lattice destabilization mechanism in the Ni-substituted zinc borohydride lattice structure using DFT and lattice dynamics techniques. The ground state energy calculations from DFT together with the phonon spectra calculated by the direct method lattice dynamics have provided a mechanistic understanding of the dehydrogenation in this doped system, and provide insights into how dopants affect decomposition of this complex borohydride. Cohesive energy calculations indicate that substitution of the Zn atoms by Ni produces a more stable structure than that resulting from substitution of B atoms. This is expected from the comparable sizes of the Ni and Zn atomic radii, and the significantly smaller atomic radius of the B atom. Lattice dynamics indicate that Ni affects both low (librational) and high (bending) frequency modes of the BH_4 complex.

The modes that soften are mainly from both hydrogen and B displacements nearest to the Ni dopant in the complex. These soften all modes and introduce instability in the lattice, thus improving dehydrogenation reactions. From the crystal bonding analysis, we see that bond lengths between Ni-H decrease and B-H bond lengths increase for the doped complex, compared to the pure system. Also, it indicates that Ni has an affinity towards H atom and helps the dehydrogenation mechanism by destabilizing the complex hydride. This result is also further verified by the calculated hydrogen atom removal energy from the pure and doped systems. We have found that 0.124 eV/ H-atom more energy is required for the former than for the latter case. These theoretical results

are in qualitative agreement with experimental findings[8, 9]. The methodology outlined in this work is applicable to the study of other complex hydrogen storage materials.

Chapter 6 - First-Principles Investigation Of The $Mn(BH_4)_2$

6.1. Abstract

Manganese borohydride ($Mn(BH_4)_2$) is considered to be a high-capacity (~10 wt%) solid-state hydrogen storage candidate, but so far has not been shown to exhibit reversible hydrogenation. This study presents the calculated crystal structure and electronic structure of $Mn(BH_4)_2$ from density-functional theory (DFT) within the generalized gradient approximation (GGA) and thermodynamic properties from the direct method lattice dynamics. The calculations of phonon spectra of $Mn(BH_4)_2$ suggest that *I-4m2* symmetry is a stable phase at finite temperature. The formation energy of $Mn(BH_4)_2$ for the *I-4m2* symmetry is -28.93 kJ/f.u. at 0 K including zero point energy (ZPE) corrections and standard state enthalpy of formation is predicted to be -58.89 kJ/f.u. The most feasible dehydrogenation reaction is found to be $Mn(BH_4)_2 = Mn + 2B + 4H_2$, which is an endothermic reaction at decomposition temperature. The spin polarized electronic density of states shows that manganese borohydride is a half-metallic nature due to the presence of half filled 3*d* electrons from Mn. The electronic structure analysis shows that the interaction between Mn atoms and BH_4 complexes has an ionic character while the internal bonding of BH_4 is essentially covalent.

6.2. Introduction

Light weight, low cost, highly reversible hydrogen storage systems are essential for realizing low temperature PEM fuel cell powered vehicles[89]. The breakthrough discovery of Ti- catalyzed $NaAlH_4$[90, 91] for the reversible onboard hydrogen storage may not be the ideal system to attain the DOE 2010 and FreedomCAR technical targets. This is because for $NaAlH_4$, the usable hydrogen storage capacity achievable is 5.4 wt. %, which is well below the set DOE goals of 6.0 wt. % by 2010. Hence, borohydride complexes as hydrogen storage materials have recently attracted great interest. The borohydride complexes $NaBH_4$ and $LiBH_4$ possess high hydrogen storage capacity of 13.0 wt. % and 19.6 wt. %, respectively. However, the release of hydrogen from $NaBH_4$ is possible only by hydrolysis (reaction with H_2O), and this process is irreversible. For the case of $LiBH_4$, the catalytic addition of SiO_2, significantly enhances its thermal desorption rate at 200 °C[44]. In general, the thermal decomposition and/or recombination of hydrogen either from $NaBH_4$ or $LiBH_4$ are difficult to achieve because of the thermodynamic stability due to strong B-H interactions[45, 92]. A systematic approach to study the phase stability of $LiBH_4$ based on *ab initio* calculations has been presented and four thermodynamically stable phases have been identified, including a new phase of *Cc* symmetry for the first time for $LiBH_4$[45]. A correlation has been reported between thermodynamic stability of metal borohydrides and Pauli electronegativity of the parent components using first principles calculations[46].

Most of the commonly known borohydrides are found to be unsuitable for on-board hydrogen storage applications. This is primarily attributable to the high stability resulting from very high decomposition temperatures or complete irreversibility of

hydrogen desorption[47]. Theoretically, it was shown that $Zn(BH_4)_2$ can be stable at finite temperature and also Ni doping improves the dehydrogenation mechanism of this complex borohydride[93, 94]. This allows consideration for on-board applications as $Zn(BH_4)_2$ has a very high theoretical hydrogen storage capacity of 8.5 wt%. However, experimentally it was found that thermal decomposition of $Zn(BH_4)_2$ comprises not only of the evolution of H_2, but also production of an appreciable amount of B–H (borane) compounds[87]. Lowering the decomposition temperature by Ni doping may lead to negligible release of boranes[88]. $Mn(BH_4)_2$, among all other transition complex borohydrides, is stable at room tempearature[47].

Although $Mn(BH_4)_2$ is a potential candidate for hydrogen storage, no literature is available about its structural and thermodynamic properties. In this study, we performed a combination of *ab initio* DFT and lattice dynamics calculations[93] to establish the stable crystal structure and to determine the finite temperature thermodynamic properties of $Mn(BH_4)_2$.

The enthalpy of formation is an important predictor of decomposition temperature for the decomposition reaction with its associated thermodynamic parameters. For a simple metal hydride, when the material is being heated, the effect of entropy starts dominating the enthalpy, and the Gibbs energy at the decomposition temperature and pressure is zero. During heating, the entropy change of solid materials is very small compared to the gas phase, which allows us to consider that the entropy change during the decomposition reaction to be primarily due to H_2 evolution. Formation enthalpy and Gibbs energy are the best predictors of the stability of the theoretically predicted phases and such data may serve as guide for possible decomposition or synthesis routes. So, our

calculations were also extended to find the theoretically possible dehydrogenation reaction of this complex hydride based on the Gibbs energy calculations. The most favorable dehydrogenation reaction will have the lowest value of the Gibbs energy. In this study, we have considered the following different possible reactions (Equations. ((6-1*a*)-(6-1*e*))) for $Mn(BH_4)_2$ and estimated the associated Gibbs energy of dehydrogenation values:

$Mn(BH_4)_2 = Mn + 2B + 4H_2$ 6-1*a*

$Mn(BH_4)_2 = MnH_2 + 2B + 3H_2$ 6-1*b*

$Mn(BH_4)_2 = MnB_2 + 4H_2$ 6-1*c*

$Mn(BH_4)_2 = MnH_2 + B_2H_6$ 6-1d

$Mn(BH_4)_2 = Mn + B_2H_6 + H_2$ 6-1*e*

6.3. Simulation methods

Density functional theory (DFT) is at present considered to be a versatile and important tool to solve innovative research problems in metal-hydrogen interactions and establish associated mechanisms. Successful application of DFT to a materials problem involves three distinct steps; (i) translation of the engineering problem to a computable atomistic model, (ii) computation of the required physicochemical properties, and (iii) validation of the simulation results by comparison with laboratory experiments[49]. Lattice dynamics[50, 51], using a direct force constant method, helps one to complete the picture by allowing for calculation of the finite temperature thermodynamic properties. Crystal structure stability and electronic structures for complex hydrides[55, 56, 93] have been reported on the basis of DFT calculations.

6.3.1. Ab initio methods

First-principle calculations were performed on $Mn(BH_4)_2$ using DFT within the generalized gradient approximation (GGA) with the Perdew-Wang 91 (PW91) functional[59] and projected augmented wave (PAW)[25, 60] method utilizing a plane wave basis set to calculate the total energies, as implemented in the Vienna *Ab initio* Simulation Package (VASP)[18, 26, 27]. A $5\times5\times5$ Monkhorst-Pack[61] **k**-point mesh was used for sampling the Brillouin zone. A kinetic energy cutoff of 400 eV was used for $Mn(BH_4)_2$, MnH_2, B_2H_6 and MnB_2 for the plane wave basis set. For Mn, B and H_2, the same kinetic energy cutoff values as for $Mn(BH_4)_2$ were utilized, in the self-consistent total energy calculations. This allows for the maximum cancellation of errors in the reaction enthalpy evaluations, which are calculated as small energy differences between reactants and products. The criterion for self-consistency in the electronic structure determination was that two consecutive total energies differed by less than 0.001 meV. The atomic positions and the lattice parameters, including the unit cell volume, were optimized by minimizing the forces and stresses until the residual forces between the atoms were within 1 meV/Å.

6.3.2. Direct method lattice dynamics

DFT is a non-empirical-parameter method whose applications and predictive ability in different fields are known for some time. Combination of DFT with different techniques such as linear response method[28, 29] or direct methods[30-32] allows us to evaluate phonon dispersion curves without empirical parameters. Parlinski *et al.*[33, 34] developed the direct method where the forces are calculated *via* the Hellmann-Feynman theorem using DFT-derived total energies, assuming a finite range of interaction. The

phonon spectra are then derived using Newton's equation of motion in the lattice dynamics calculations.

Calculations of the phonon density of states and the resulting vibrational contributions to the free energy were performed using the PHONON code developed by Parlinski[35]. These calculations used the same exchange–correlation functional as our total energy calculations and an energy cutoff of 400 eV. Force constants were computed using displacements of asymmetric individual atoms by +/- 0.02 Å and the absolute force constant cutoff value utilized was 0.01 a.m.u. $(THz)^2$. Based on the optimized crystal structure, a supercell consisting of a large number of atoms depending on the type of unit cell was generated from the conventional cell. It is necessary to use a relatively large supercell to avoid interaction between images of the displaced atom when defining the phonon density of states.

6.4. Results and discussions

We calculated the Gibbs energy of reactions considering Equations ((6-1*a*)–(6-1*e*)) and based on the total energy calculation by combined DFT and direct method lattice dynamics. The total energy of $Mn(BH_4)_2$ was calculated based on the stable structure found based on positive definite frequency distribution criteria over the Brillion zone. For MnH_2 and MnB_2, the total energy was calculated based on *fcc* fluorite (*Fm-3m*)[95] and *hcp* AlB_2 type (*P6/mmm*)[96] structures, respectively. The total energy of B was calculated based on the hexagonal (*R-3m*) structure[93]. We calculated the optimum binding energy for H_2 molecule[93], for which we used the constant velocity MD simulation method in VASP. Mn is known to be the most complex element in the periodic table[97]. Mn has 4-5 phases at different temperatures and also different type of magnetic properties at different

conditions. From our own experimental results we have found $Mn(BH_4)_2$ to decompose at temperatures lower than 500 K[98]. Hence, in this work, Mn was considered to be in the α phase (valid till 900 K). It is known that α-Mn phase is paramagnetic with a Neel temperature of 95 K (bcc structure in the space group of *I-43m*) below which it is anti-ferromagnetic (body centered tetragonal structure in the space group of *I-42m*)[97]. So, in our calculations, we considered α-Mn as anti-ferromagnetic till 95 K and above that as a paramagnetic phase. The total energy was found to be -8.964 eV/f.u. which is well matched with the DFT calculated literature value of 8.97 eV/f.u.[97]. The following sections discuss the stable crystal structures, electronic structure and finite temperature reaction enthalpy and Gibbs energy.

6.4.1. Crystal structure

The structure of $Mn(BH_4)_2$ was found to be tetragonal type in the space group of *I-4m2* (# 119). We started our calculations for $Mn(BH_4)_2$ from the 21 known similar complex model structures presented in Table 6-1. Using this methodology, we first calculated the cohesive energy, *i.e.* the energy required to break the atoms of the solid into isolated atomic species of $Mn(BH_4)_2$ based on these models. Then we calculated the enthalpy of formation of these structures as shown in the Table 6-1. Only five space groups showed negative enthalpy of formation indicate possible thermodynamically favorable structures. To establish finite temperature structural stability, we calculated the phonon spectra of those structures only by the direct force constant lattice dynamics technique. It was found that only *I-4m2* space group shows positive phonon density of states (DOS). This suggests that *I-4m2* (tetragonal) space group is the only stable phase for $Mn(BH_4)_2$ at finite temperatures.

Table 6-1. The model structures (XY_2Z_8 type) used as input for the structural optimizations. The cohesive energy and enthalpy of formation (excluding ZPE) of MnB_2H_8 are calculated based on these model structures. *Z* is the number of formula units in the unit cell

Model	Space group no. (Z)	Cohesive energy, eV/atom	Formation enthalpy, kJ/f.u.
[65, 71, 99-102]$MgAl_2H_8$	1 (2)	3.0488	90.918
	164 (1)	3.1739	-41.580
[103]$MgAl_2Cl_8$	15 (4)	2.5658	602.257
[46, 93]ZnB_2H_8	2 (2)	2.4123	764.771
	26 (2)	3.0868	50.705
[46, 104]MgB_2H_8	13 (2)	2.5309	639.185
	119 (4)	3.2210	-91.428
[69]$CaAl_2H_8$	14 (2)	2.5625	605.708
	61 (8)	3.1206	14.859
	147 (9)	3.1041	32.356
	189 (3)	2.9232	233.814
[43]CaB_2H_8	70 (8)	3.1765	-44.272
[73]BeB_2H_8	110 (16)	3.1178	17.849
[105, 106]ZrW_2O_8	19 (12)	3.1119	24.042
	198 (4)	2.9679	176.554
	213 (8)	1.8181	1393.734
[106]$ZrMo_2O_8$	163 (6)	3.1412	-6.922
[107]$TiAl_2Cl_8$	14 (2)	2.1058	1089.184
[72]$CuAl_2Cl_8$	2 (2)	2.4802	692.879
[108]$CdAl_2Cl_8$	7 (2)	3.057806	81.361
[109]MRe_2O_8 (M = Mn, Co, Ni, Zn)	147 (1)	3.14069	-6.384

In the phonon density of states of the stable space group (Figure 6-1), the phonon frequencies are classified into three groups. From the analysis of the eigenvectors, we found eigenmodes originate from internal B-H bending in the region of 30.75-39.75 THz and the stretching vibrations in the $[BH_4]^-$ complex anion were found to be in the region of 67.25-71.75 THz for *I-4m2* space group, respectively. In the 2000 - 2500 cm^{-1} (60 - 75 THz) region, strong bands are observed in the spectra of borohydride complexes that correspond to the stretching vibrations of the B-H bonds. To compare these theoretical results with experimental data, we prepared the new transition metal based complex borohydride $Mn(BH_4)_2$ from the following stoichiometric reaction by the mechano-chemical synthesis route and measured the solid state FTIR spectrum:

$2NaBH_4 + MnCl_2 \rightarrow Mn(BH_4)_2 + 2NaCl$

$Mn(BH_4)_2$ formation was confirmed from the solid state FTIR spectrum (shown in (Figure 6-1) which indicates that the B-H stretching at 2223.9 – 2371.6 cm^{-1} (66.70 - 71.17 THz) and B-H bending at 1125.7-1213.2 cm^{-1} (33.78 - 36.40 THz) are compared well with theoretical results. It also can be seen from Figure 6-1, the librational frequencies (in regions <17.75 THz) that originate from the displacement of the heavy atom Mn and $[BH_4]^-$ are lower than those of the B-H bending and stretching modes of $[BH_4]^-$.

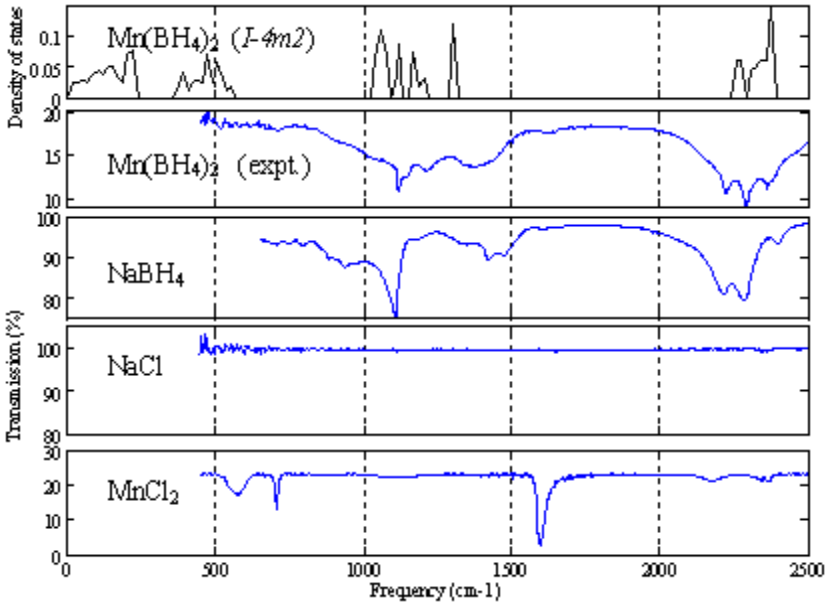

Figure 6-1. Total density of phonon states *g(w)* of $Mn(BH_4)_2$ in *I-4m2* symmetry. Total phonon density of states is normalized as $\int g(w)dw = 1$. FTIR spectrum of $Mn(BH_4)_2$ (along with those of precursors and products) prepared by ball milling of $2NaBH_4 + MnCl_2$. The black lines represent phonon density of states of $Mn(BH_4)_2$ and blue lines represent the FTIR spectra of $Mn(BH_4)_2$, $NaBH_4$, NaCl and $MnCl_2$, respectively

The minimum total energy and primitive cell volume for $Mn(BH_4)_2$ is -50 eV/f.u. and 333.035 $Å^3$ for *I-4m2* structure, respectively. The optimized lattice parameters and atomic positions are given in Table 6-2. Figure 6-2 shows the optimized tetragonal (*I-4m2*) crystal structure. The crystal structure of $Mn(BH_4)_2$ is consist of metal cation Mn^{2+} and nearly ideal tetrahedral $[BH_4]^-$. For the *I*-4*m*2 structure, it is characterized by a fourfold coordination of $[BH_4]^-$ ions around the Mn^{2+} ions. Furthermore, each Mn^{2+} has 8 nearest neighbor H atoms with the shortest Mn-H bond distance around 2.06 Å. The B-B nearest neighbor distance is found to be 3.68 Å and Mn-B distance 2.41 Å. The B-H bond lengths and the H-B-H bond angles within the $[BH_4]^-$ tetrahedral of *I-4m2*

symmetry are found to be d_{B-H} = 1.23 - 1.24 Å and θ_{H-B-H} = 106 – 115°, respectively. The geometry of the BH_4 tetrahedron is similar to that found in isolated $[BH_4]^-$ ions, an ideal tetrahedral structure with a constant bond length of 1.24 Å for B-H bonds, and tetrahedral angles of 109.5°, where the B and H atoms are covalently bonded[110].

Table 6-2. Optimized crystal structure of $Mn(BH_4)_2$. The number of formula units in the unit cell is *Z*. All the atomic positions are given by Wyckoff letters

Space group	Element	Wyckoff letter	X	Y	Z
I-4m2 (Z = 4)	Mn1	2*c*	0.0000	0.5000	0.2500
a = *b* = 8.182	Mn2	2*a*	0.0000	0.0000	0.0000
Å and *c* =	B	8*i*	0.2311	0.00000	0.8494
9.951	H1	8*i*	0.2467	0.0000	0.7266
	H2	8*i*	0.6392	0.0000	0.9137
	H3	16*j*	0.1590	0.1270	0.8786

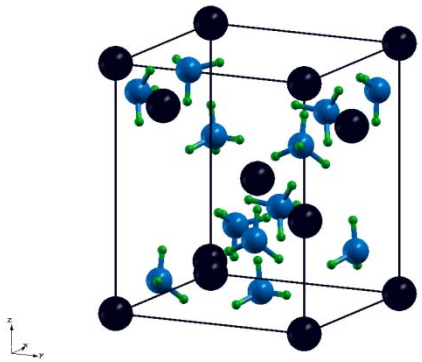

Figure 6-2. Three-dimensional crystal structures of $Mn(BH_4)_2$ of space group *I-4m2* (#119) (Black (large), blue (middle) and green (small) spheres represent Mn, B and H atoms, respectively)

6.4.2. Electronic structure

The local and total spin polarized electronic density of states (DOS) were calculated for the stable crystal structure of $Mn(BH_4)_2$ (shown in Figure 6-3). According to spin polarized total/local DOS calculations (Figure 6-3), the Mn 3*d* DOS has half-metallic character for $Mn(BH_4)_2$. The Mn 3*d* DOS have a high spin-up occupation below the Fermi energy and high peak of spin-down unoccupied states in the region of 1±2 eV above the Fermi energy (Figure 6-3). From this point, Mn partitial 3*d* DOS has metallic character for spin-down and insulating character for spin-up projection, are supposed to show some intermediate behavior. Other than this, there are two more valence bands and one conduction band found in the total DOS plot. Both these two valence bands are well below the Fermi level. From the partial DOS plot (Figure 6-3), it can also be seen that the lowest valence band is dominated by B 2*s* electrons and H 1*s* electrons with negligible contribution from Mn. The middle part of the valence band is mainly dominated by B 3*p* electrons, H 1*s* electrons and smaller number of Mn 3*d* electrons. The valence band well below Fermi level is dominated by B and H electrons that make a strong B-H bond. The conduction band is primarily dominated by B 2*p* electrons and to a lesser extent B 2*s* and H 1*s* electrons. Although H *s* electrons are prominent in the valence band, small number states are also found in the conduction band, which may indicate charge transfer to H atoms.

The overall features of the DOS and PDOS are different from those of $LiBH_4$[75], $NaBH_4$[68], KBH_4[68], $Mg(BH_4)_2$[46] and $Zn(BH_4)_2$[93]. The main difference is that there is no band gap between valence and conduction bands for $Mn(BH_4)_2$, whereas, the above mentioned borohydrides have distinct, wide band gaps. This may be due to the presence

of the half-filled *d* orbital of the Mn atom resulting in high peak of spin-down unoccupied states above the Fermi energy and also it shows magnetic behavior with a total magnetic moment of 5.13 μ_B/Mn for *I-4m2* phase. However, further investigations are required before providing more specific interpretations which is beyond the scope of this work.

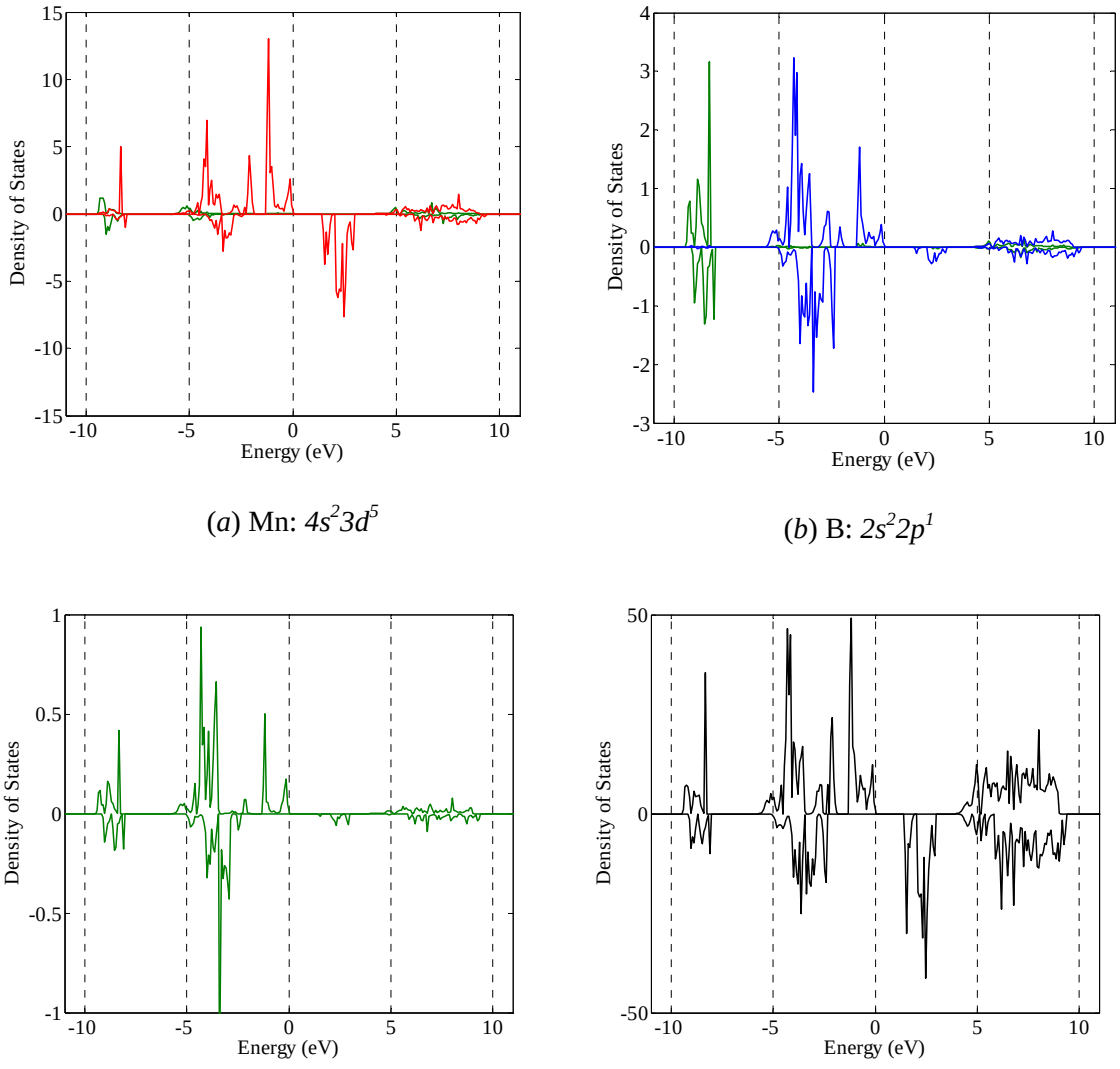

(*a*) Mn: $4s^2 3d^5$

(*b*) B: $2s^2 2p^1$

(*c*) H: $1s^1$

(*d*) $Mn(BH_4)_2$

Figure 6-3. DFT/GGA electronic spin polarized local/total density of state (DOS) relative to Fermi level for $Mn(BH_4)_2$. (Green line for *s*, blue line for *p* and red line for *d* orbital)

The Electron Localization Function (ELF)[76, 77] and charge density for the $Mn(BH_4)_2$ were calculated for the space group *I-4m2*, which is shown in Figure 6-4. The ELF calculated here shows strong and large attractors around the H atoms. The very low ELF value on the B sites indicates delocalized electrons, while a spherical shell attractor is seen around Mn. Low ELF value between Mn and $[BH_4]^-$ complex indicates an ionic bond. Whereas, a very high value of ELF within the $[BH_4]^-$ complex indicates covalent bonding. The plotted charge density shows that valence charge density around Mn atom is considerably low. The charge density is strongly localized around $[BH_4]^-$ anions. This also confirms the strong covalent B-H bonding within the $[BH_4]^-$ complex.

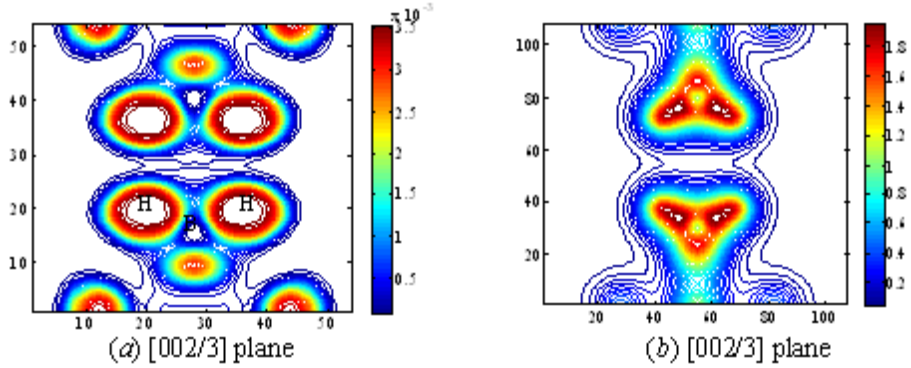

Figure 6-4. (*a-b*) Electron localization function (ELF) and Charge density of $Mn(BH_4)_2$ for *I-4m2* symmetry. The plane contains both Mn and B and H atomic sites are projected on the plane

6.4.3. Thermodynamics

Formation enthalpy and Gibbs energy are the best aids to establish whether the theoretically predicted phases are likely to be stable or not. The thermodynamic

expressions for the enthalpy [*H(T)*] and Gibbs energy [*G(T)*] can be obtained by the following equations:

$$H(T) = E(T) + pV \qquad 6\text{-}2$$

$$E(T) = E(0) + \delta H(T) \qquad 6\text{-}3$$

$$E(0) = E_{elec} + E_{ZPE} \qquad 6\text{-}4$$

$$\delta H(T) = E_{vib}(T) + E_{rot}(T) + E_{tran}(T) \qquad 6\text{-}5$$

$$G(T) = H(T) - TS(T) \qquad 6\text{-}6$$

where, E_{elec} is the electronic total energy of the crystal obtained from the density functional total energy calculations. $E_{vib}(T)$, $E_{tran}(T)$ and $E_{rot}(T)$ are the finite temperature vibrational (excluding ZPE), translational and rotational energies, respectively, and *p* is the pressure (1 atm), and *V* is the volume. The translational, rotational and *pV* energy terms are important for the gas phase only, and thus are neglected for these solid-phase calculations. The E_{ZPE} for Mn was found to be 4.04 kJ/f.u.. The zero point energy of *I-4m2* space group of $Mn(BH_4)_2$ was calculated to be 204.03 kJ/f.u, respectively. For B and H_2 gas molecule the E_{ZPE} were found to be 12.478 kJ/f.u. and 28.12 kJ/f.u.[93]. The calculated enthalpy [*H(T)-H(298)*], entropy (*S(T)*) and Gibbs energy [-(*G(T)-H(298)*)] for B and Mn are given in Figures 6-5 and 6-6, respectively.

The thermodynamic functions were calculated on the basis of the positive phonon DOS (Figure 6-7) and resulting vibrational energy contribution to the Gibbs energy by the direct method lattice dynamics. The solid and dotted lines (Figures 6-5 and 6-6) represent the calculated and experimentally measured[111] results, respectively. The calculated thermodynamic functions: the enthalpy and the Gibbs energy are in good

agreement with the experimental values for B but in little less agreement (within ~20% of experimental values) for the Mn crystal lattice.

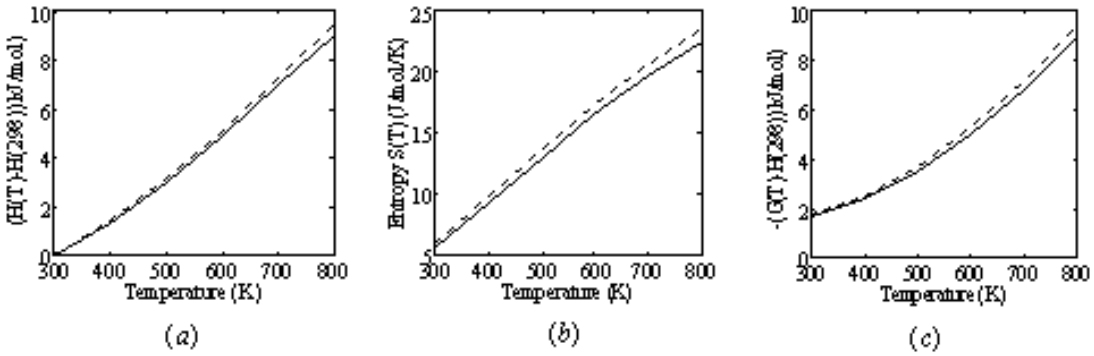

Figure 6-5. Calculated (solid line) and experimental[111] (dotted line) thermodynamic functions for α-B. The functions including the enthalpy (*H(T)−H(298)*), the entropy (*S(T)*) and the Gibbs energy [-(*G(T)-H(298)*)] are presented in (*a*), (*b*) and (*c*), respectively. *H(298)* denotes the standard enthalpy at 298 K

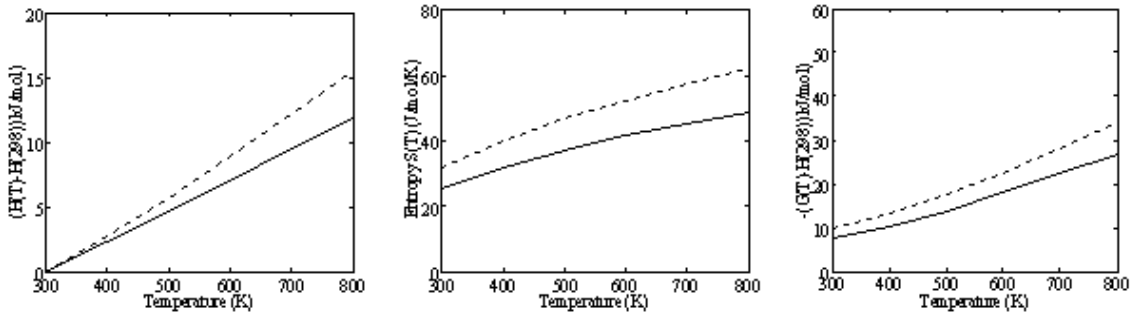

(*a*) (*b*) (*c*)

Figure 6-6. Calculated (solid line) and experimental[111] (dotted line) thermodynamic functions for α-Mn (anti-ferromagnetic). The functions including the enthalpy (*H(T)−H(298)*), the entropy (*S(T)*) and the Gibbs energy [-(*G(T)-H(298)*)] are presented in (*a*), (*b*) and (*c*), respectively. *H(298)* denotes the standard enthalpy at 298 K

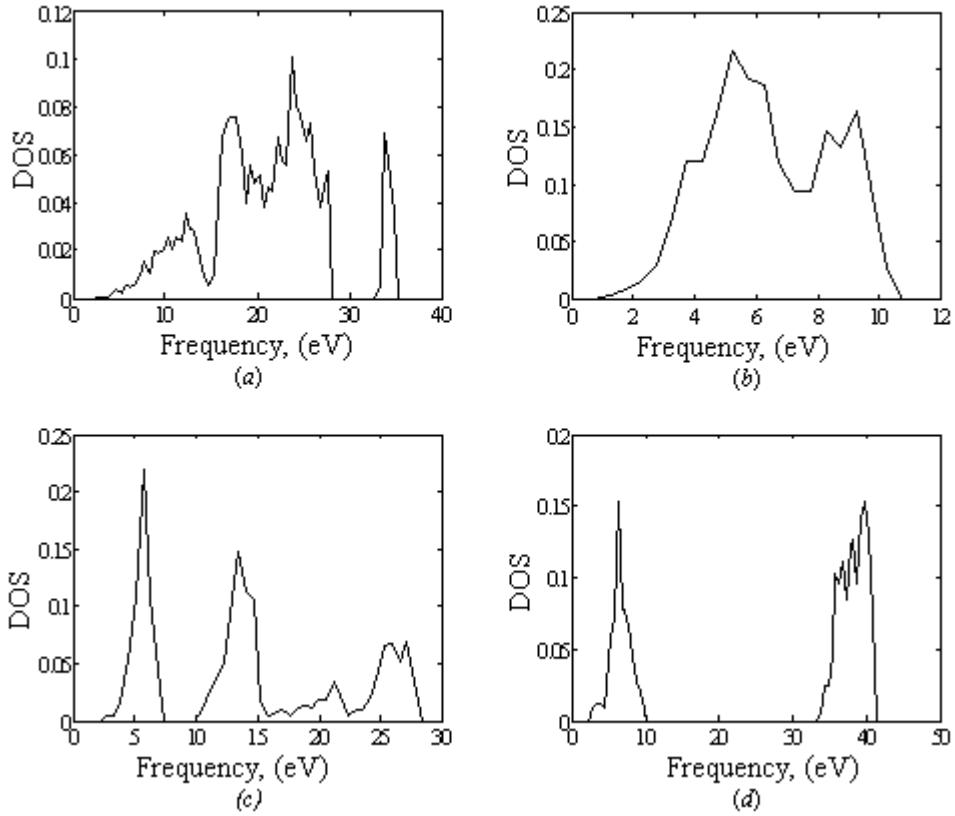

Figure 6-7. (*a-d*) Total density of phonon states *g(w)* of B, Mn, MnB_2 and MnH_2 crystal structures, respectively. Total phonon density of states is normalized as $\int g(w)dw = 1$

For H_2 gas molecule, one needs to know the Gibbs energy at the standard pressure of 1 atm. The vibrations cannot be treated directly from the phonon calculations for H_2 gas molecule because the phonon approach always considers the system as a crystal solid, and thus neglects the translational and rotational modes. The Gibbs energy was calculated by combining both computational and experimental results using Equation (6-7)[112]:

$$G_T(H_2) = E_{el}(H_2) + E_{ZPE}(H_2) + pV + \Delta G_T(H_2) \qquad 6\text{-}7$$

where, $E_{el}(H_2)$ is the electronic binding energy of a H_2 molecule obtained from constant velocity MD simulation using VASP[93]. $E_{ZPE}(H_2)$ is the zero-point energy of a H_2 molecule, p and V are the pressure (1 atm) and the molar volume (of the H_2 ideal gas), respectively, and the last term $\Delta G_T(H_2)$ is the temperature-dependent Gibbs energy with respect to the temperature of 0 K. As a common procedure[113], the $\Delta G_T(H_2)$ can be calculated using Equation (6-8).

$$\Delta G_T(H_2) = [H_T(H_2) - H_0(H_2)] - T \times [S_T(H_2) - S_0(H_2)] \qquad 6\text{-}8$$

where, $H_T(H_2)$ and $H_0(H_2)$ are the enthalpies of H_2 at T and 0 K, respectively, and $S_T(H_2)$ and $S_0(H_2)$ are the entropies of H_2 at T and 0 K, respectively. Inputting the thermochemical data[114], we calculated the numerical values of $\Delta G_T(H_2)$.

6.4.4. The enthalpy and the Gibbs energy of the reactions

In the previous section, the calculated and experimental thermodynamic functions of the B, Mn and $Mn(BH_4)_2$ lattices were plotted. In this section, these functions are utilized to calculate the enthalpy and Gibbs energy of reaction.

To study the reactions, one needs to calculate the temperature-dependent Gibbs energy difference (ΔG_{rxn}) and the entropy contribution difference $\Delta(TS(T))_{rxn}$ between the reactants and products using the following equations (Equations ((6-9)-(6-10))):

$$\Delta G_{rxn}(T) = \sum_{products} G(T) - \sum_{reactants} G(T) \qquad 6\text{-}9$$

$$\Delta(TS(T))_{rxn} = \sum_{products} TS(T) - \sum_{reactants} TS(T) \qquad 6\text{-}10$$

The reaction enthalpy can be calculated from Equation (6-11) as follows:

$$\Delta H_{rxn}(T) = \Delta G_{rxn}(T) + \Delta(TS(T))_{rxn} \qquad 6\text{-}11$$

For convenience, we denote r = reactants and p = products. A positive value of $\Delta G_{p\text{-}r}$ means that the reaction is not spontaneous and thermodynamically not favorable, a negative value of $\Delta G_{p\text{-}r}$ means the reaction is spontaneous and hence, thermodynamically favorable.

The standard state enthalpy of formation of $Mn(BH_4)_2$ was found to be -58.89 kJ/f.u. using DFT while the standard state enthalpies of formation of MnH_2, MnB_2 and B_2H_6 were found to be -12.10, -113.93 and 40.26 kJ/mol. In comparison, literature values are -13.0[95], -120.0 (expt.)[115]/-140.0 (theory)[96] and 35.3 kJ/mol, respectively. The standard state Gibbs energies of dehydrogenation reactions (Equations ((6-1*a*)-(6-1*e*))) were calculated, with rounded-off values in kJ/mol of H_2 as -17, -10, -45, 25 and 13, respectively. It can be concluded from the calculated standard state Gibbs energy of the dehydrogenation reactions that the reactions (6-1*c*), (6-1*a*) and (6-1*b*) are the three favorable dehydrogenation reactions at standard conditions. So, it is expected that upon heating reaction (6-1*c*) will occurs first and then reactions (6-1*a*) and (6-1*b*) may or may not occur in practice. No diborane products should be produced during the dehydrogenation reaction, theoretically.

The calculated Gibbs energy differences $\Delta G_{p\text{-}r}$ for the reactions ((6-1*a*)-(6-1*e*)) for the temperature range of 0-800 K are plotted in Figure 6-8(*a*). It is shown that the Gibbs energy and the enthalpy of reaction is the lowest and negative, respectively for reaction (6-1*c*) over all of this temperature range. But the experimental results suggests that dehydrogenation of $Mn(BH_4)_2$ is an endothermic reaction at its decomposition temperature (413 K)[98] which contradicts the theoretically predicted exothermic reaction. This contradiction may be because it is kinetically unfavorable to form the MnB_2 phase at

the lower temperature range (< 800 K) considered in our calculations. Formation enthalpy of MnB_2 has been measured by calorimetrically at very high temperatures above 2000 K[115]. Perhaps, kinetics prevented its formation for these authors to have not made their measurements at lower temperatures. So the next most favorable reaction is to be considered as reaction 6-1(*a*), which is endothermic and also Gibbs energy become negative over all of the temperature range above 116 K. Hence equation 6-1(*a*) is found to be most feasible to occur at the experimentally determined reaction temperature (413 K). However, experimental investigations are required to identify the phases which exist after the dehydrogenation of $Mn(BH_4)_2$ before providing more specific interpretations.

The calculated Gibbs energy differences $\Delta G_{p\text{-}r}$ and reaction enthalpy for the reaction (6-1*a*) for the temperature range of 0-800 K are shown in Figure 6-8(*b*). The enthalpy of reaction for (6-1*a*) reaction suggests that the dehydrogenation reaction is endothermic over all of this temperature range. It is also shown that the Gibbs energy of reaction (6-1*a*) is positive till 116 K and become negative over all of the temperature range studied above 116 K. This suggests that upon heating, $Mn(BH_4)_2$ is stable with respect to decomposition into Mn + 2B + $4H_2$ till the Gibbs energy become negative and then releases H_2 according to the above reaction spontaneously. This is due to the large entropy contribution ($T\Delta S$) from the gas molecules. The entropy contributions for the $4H_2$ gas molecules, the crystal B, crystal Mn and crystal $Mn(BH_4)_2$ lattices for the reverse formation reaction (6-1*a*) are shown in Figure 6-8(*b*). High yield of gaseous products from the reactions should be favored with increasing temperature[116], and this is consistent with our dehydrogenation reaction (6-1*a*). Based on standard state Gibbs energy of reaction (1*a*), and in Figure 6-8(*a*), we can conclude that H_2 desorption from

$Mn(BH_4)_2$ is thermodynamically favorable essentially at all non-zero temperatures above 116 K. Decrease in negative free energies of dehydrogenation with increase in temperature suggest that $Mn(BH_4)_2$ is metastable with respect to decomposition *via* reaction (6-1*a*). On the other hand, we found from our TGA experiment on $Mn(BH_4)_2$ indicates that desorption does not take place until the temperature is raised above 413 K[98]. These suggest that the relatively high temperatures needed in practice for H_2 release are a consequence of poor kinetics, not unfavorable thermodynamics. It would be interesting to test whether the predicted decomposition reaction is observed experimentally or not.

The values of $\Delta H_{p\text{-}r}$ are always positive above 0 K, indicating that the dehydrogenation reaction (6-1*a*) is endothermic at standard conditions. It can also be seen from Figure 6-8(*b*) that the values of $\Delta(TS)_{p\text{-}r}$ are always positive, indicating that the entropy contribution in *p* is always larger than in *r* (as T>0 K). Therefore, it is concluded that the entropy contribution is the essential reason for the dehydrogenation reaction to take place. From the above figure, it can also be concluded that the net entropy contribution to the dehydrogenation reaction is mainly due to the entropy contribution from the H_2 gas molecule.

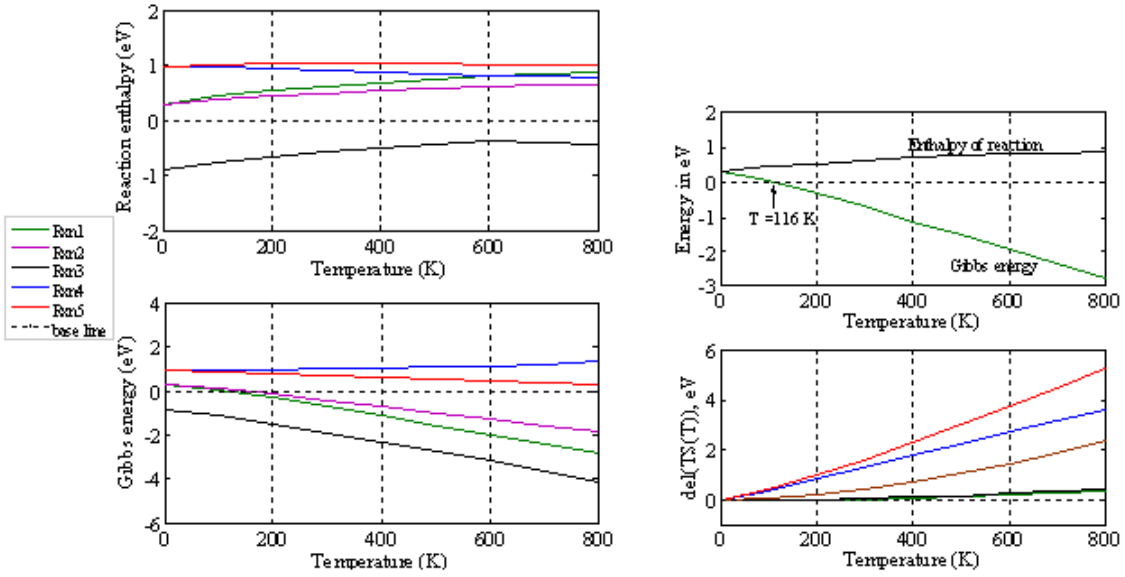

(*a*) (*b*)

Figure 6-8. Temperature dependent reaction enthalpy and Gibbs energy of reactions ((6-1*a*)-(6-1*e*)) (*a*), temperature dependent reaction enthalpy and Gibbs energy and the entropy contribution for the reaction $Mn(BH_4)_2$ = Mn + 2B+ $4H_2$ (*b*). Energy difference between the reactant *r* = ($Mn(BH_4)_2$) and product *p* = (as an example: Mn + 2B + $4H_2$). Symbol $\Delta G_{p\text{-}r}$ indicate the Gibbs energy difference between *r* and *p*, [$\Delta G_{p\text{-}r} = G_p - G_r$]. The Gibbs energy difference $\Delta G_{p\text{-}r}$ (lower palette) and the enthalpy difference $\Delta H_{p\text{-}r}$ (upper palette) are shown in figures (*a*). The total entropy contribution for the reaction (6-1*a*) $\Delta(TS)_{p\text{-}r}$ (blue line), for H_2 molecules $4T\Delta S(H_2)$ (red line), for Mn (black line), for B (green line) and for the $Mn(BH_4)_2$ (brown line) are shown in figure (*b*). Rxns: (1-5) ≅ reactions: ((6-1*a*)-(6-1*e*)).

6.5. Summary

In this work, we have predicted the stability and favorable dehydrogenation reactions of the complex manganese borohydride structure from theoretical calculations. This required investigation of both the ground state energy by DFT and the lattice

vibration energy by the direct method lattice dynamics. These calculations establish the most stable structure of $Mn(BH_4)_2$. The Gibbs energy calculations of $Mn(BH_4)_2$ at finite temperatures suggest that *I-4m2* symmetry is the most stable structure at finite temperature. Our estimated value for the formation enthalpy of $Mn(BH_4)_2$ is found to be -28.93 kJ/f.u. (with ZPE) at 0 K, which suggests that it should be possible to synthesize this phase. From electronic structure calculations, ionic interaction between Mn and $[BH_4]^-$ and strong covalent B–H interaction within the $[BH_4]^-$ tetrahedral structure are revealed. Electronic density of states studies reveal that Mn partial 3*d* DOS has metallic character for spin-up and insulating character for spindown projection, are supposed to show some intermediate behavior, which suggests that the $Mn(BH_4)_2$ is a half-metallic hydrogen storage material.

The phonon dispersion relations and phonon density of states of the solid phases are calculated using a direct force-constant method. On the basis of the phonon DOS and resulting vibrational energy contribution by the direct method lattice dynamics, the calculated thermodynamic functions including the enthalpy and the Gibbs energy are in good agreement with the experimental values of both B and Mn crystal lattice.

Standard state enthalpy of reaction and Gibbs energy calculations reveal that reaction (6-1*a*), *i.e.*, $Mn(BH_4)_2 \rightarrow Mn + 2B + 4H_2$ is the most feasible dehydrogenation reaction. The calculated standard state enthalpy of dehydrogenation is positive, indicating that the decomposition reaction is endothermic at decomposition temperature. To identify the components produced *via* dehydrogenation, we have performed a computational search over 5 different dehydrogenation reactions, and identified the thermodynamically favorable reaction over the temperature range T = 0 - 800 K. The

calculated Gibbs free energies of dehydrogenation of $Mn(BH_4)_2$ are negative above 116 K, indicating that $Mn(BH_4)_2$ releases H_2 according to the above reaction above 116 K spontaneously. It was also found that the net entropy contribution for the dehydrogenation reaction is mainly due to the entropy contribution from H_2 gas molecule.

These findings suggest that the crystal structure is stable at finite temperature and no diborane as a dehydrogenation product is preferred thermodynamically. Thus, $Mn(BH_4)_2$ could be considered a potential candidate for hydrogen storage. However, one needs to address the reversibility issue before its practical on-board applications. Our study has given new insights into the thermodynamically stable phase for the complex manganese borohydride. The methodology outlined in this work can be applied to studies on other complex hydrogen storage materials.

Chapter 7 - First-Principles Investigation Of Li-Mg-B-N-H System

7.1. Abstract

A density functional theory study with the gradient generalized approximation (GGA) and augmented plane wave method (PAW) is performed for the hydrogen storage properties of the complex multinary storage *Li-Mg-B-N-H* system. Using *ab-initio* methods, stability of the structures at finite temperatures are confirmed *via.* phonon spectrum calculations. Thermodynamic properties such as heat of reaction, and Gibbs energy for each reactant and product in the reaction steps in different temperature zones are calculated. It is found that reversibility occurs in the temperature range of 160-225 ^{o}C with approximately 4.38 wt% hydrogen storage capacity. The enthalpy of reversible re/de-hydrogenation is found to be 55.17 kJ/mol H_2, which is supported by experimental data. The total hydrogen storage capacity of this material is calculated to be 8.76 wt% from the desorption behavior observed at different temperatures up to 350 ^{o}C. These theoretically established reactions are validated with the suggested mechanism from experimental observations for the dehydrogenation reaction of this Li-Mg-B-N-H multinary system. These efforts are expected to contribute towards identification of suitable hydrogen storage materials.

7.2. Introduction

The discovery of clean, renewable and inexpensive sources and carriers of energy has been the concern of researchers worldwide. Compressed, liquid and slush have been the favored forms for mobile hydrogen storage. The low efficiency and increased risk of storage of such forms made solid state hydrogen the preferred form for mobile applications. Research has gained pace to find a reversible material with efficient hydrogen storage capacities. Metal/complex hydrides as hydrogen storage material have gained importance in the past few years due to rising fuel costs and ease of on-board storage. The individual storage properties of metal/complex hydrides were found to improve in their combinations. The undesired properties of these hydrides like ammonia liberation[117] or diborane liberation[87, 118], poor kinetics and irreversibility were overcome by their binary systems[119]. Many experimental and theoretical studies have been carried out to find materials with reversible properties, low desorption temperatures, accelerated kinetics and optimum hydrogen storage capacity (at 298 K, the US revised DOE system target for gravimetric hydrogen storage capacity is 5.5 wt % by 2015)[93, 94, 98, 120-125]. Experiments suggest that complex hydrides of *Li, Na, Mg, B, Al* and *N* have such properties[119]. The $LiBH_4$-$LiNH_2$ system fails to re-hydride due to its relatively small dehydriding enthalpy, and suggests that hydrogen release from the system is a kinetically - rather than thermodynamically - hindered process[79]. The $LiBH_4$-MgH_2 system was found to have 8-10 wt% reversible hydrogen storage at about 350 °C[126]. The $LiNH_2$-MgH_2 system operates at 200 °C with 4.5 wt% reversible hydrogen storage[127]. Experiments on the ternary systems of these hydrides also showed promising results and further improved storage properties. The combined $LiNH_2$-MgH_2-$LiBH_4$ system was

found to have lowered desorption temperatures, increased hydrogen purity, accelerated kinetics and good reversibility. The stoichiometry of this mixture was also a major factor for controlling the storage properties. It has been reported that the stoichiometric ratio of $LiNH_2$:$LiBH_4$:MgH_2 with a 2:1:1 molar ratio gives the best hydrogen storage performance [119, 128].

In this work, we tested the feasibility of the $2LiNH_2$ - $LiBH_4$ - MgH_2 reactant mixtures using density functional theory (DFT) studies. The reactants and products of the proposed reaction steps were checked for stability and then the thermodynamic properties of the compounds were found and compared with literature. The storage capacity of these materials was calculated from the desorption behavior observed at different temperatures. These theoretically obtained data can be used to validate the suggested mechanism from experimental observations for the dehydrogenation reaction.

7.3. Computational details

DFT studies on hydrogen storage materials using projected augmented wave (PAW)[25, 60] potentials pertaining to the generalized gradient approximation (GGA)[129] are considered the most appropriate for energy calculations due to their better accuracy than when using the local density approximation (LDA)[130]. The thermodynamic properties calculated using plane wave DFT and those found experimentally were in good agreement for a number of hydrogen storage systems[131, 132]. We used VASP[18, 26, 27] (Vienna ab initio simulation package) to perform the DFT calculations and code PHONON[35] to perform direct method lattice dynamics[32-34] for finite temperature crystal stability and thermodynamics.

The most favored structure of each compound was found from literature and its equilibrium volume was calculated by a quadratic fit of energy. These calculations were performed using Monkhorst Pack[61] meshes containing 5 x 5 x 5 *k*- points. The energy cutoff for all the compounds was set to 400 eV. The external pressures acting on each of these compounds were reduced by relaxing the volume and ionic positions of the structure. PAW potentials were used for these relaxations. The relaxations were continued till the forces on the atoms were reduced to about 0.1 meV/Å. Hellmann-Feynman (HF) forces were calculated using a super cell of the relaxed structure to avoid interaction between the atoms and then displacing its atomic positions.

These HF forces were then used to calculate the phonon density of states (DOS) for the structure at finite temperatures, which would be positive for a stable structure. Entropy and internal energy of the structure can be obtained from phonon DOS, which can be used to calculate the Gibbs energy of the reactions[132].

The experimentally observed *in situ* IR spectroscopy patterns were compared with the theoretically observed ones to validate the structure of the intermediate phases such as $Li_4BH_4(NH_2)_3$, $Mg(NH_2)_2$, $Li_2Mg(NH)_2$ and $LiMgBN_2$. To specify the atomic positions of the compounds with fractional occupancies such as $Li_2Mg(NH)_2$, we used the super cell approach[125, 133, 134].

7.4. Results and discussion

In this study, we calculated the equilibrium structures for all the compounds, namely, $LiBH_4$, $Mg(NH_2)_2$, $LiNH_2$, LiH, $Li_2Mg(NH)_2$, Li_3BN_2, MgH_2, $Li_4BH_4(NH_2)_3$, Mg_3N_2, $LiMgBN_2$ and elements like Mg, Li, B, N_2 and H_2, involved in the reaction mechanism (Table 1). Among all the above mentioned compounds, $Mg(NH_2)_2$ and

$Li_2Mg(NH)_2$ are found to be computationally intensive for phonon calculations as $Mg(NH_2)_2$ is characterized by a tetragonal unit cell belonging to the space group No. 142 with 224 atoms per unit cell[122], and $Li_2Mg(NH)_2$ is characterized by a orthorhombic unit cell belonging to the space group No. 45 with Li/Mg occupancy fractions (due to ordering of atoms) on "4*b*" and "8*c*" Wyckoff sites, resulting in a big supercell for phonon calculations. Possible arrangements of Li and Mg on "4*b*" and "8*c*" Wyckoff sites and the ordering of Mg atoms on the "8*c*" and "4*b*" sites play a significant role in determining the energetics. The magnesium atoms occupy (i) either body-diagonal or face-diagonal tetrahedral sites, (ii) either face-diagonal tetrahedral sites, and (ii) the nearest-neighbor or body-diagonal tetrahedral sites[125]. The Li/Mg occupancy fractions of 0.75 0.25 and 0.50 0.50 on "4*b*" and "8*c*" sites[133], respectively, are assumed in our calculations. Phonon calculations for the remaining solid state compounds/elements were straight forward as discussed in our earlier study[93, 94, 132].

7.4.1. Structural stability

The finite temperature stability of all the compounds and elements was established by using combined DFT and direct method lattice dynamics approach based on positive definite frequency distribution criterion over the Brillion zone. Results for some of these compounds are shown in Figure 7-1.

These stable structures were then used to calculate the finite temperature thermodynamics of the reactions[132]. Experimentally proposed multi-steps hydrogen release pathway for the intermediate phases $Li_4(NH_2)_3(BH_4)$, $Mg(NH_2)_2$, $Li_2Mg(NH)_2$ and $LiMgBN_2$[119, 128] that were formed was examined *via* vibrational spectroscopy, *i.e.,* phonon density of states calculations of the intermediate phases. In line with the

experimental FTIR study on the hydrogen reactions of $LiBH_4$-$LiNH_2$-MgH_2 systems, our calculations showed the co-existence of B-H, N-H and NH_2 stretches, as presented in Figure 7-1. The B-N stretching range found from the phonon density of states of Li_3BN_2 (formation during the exothermic reaction (4)) was 1510-1547 cm^{-1} and B-N stretching range found from phonon density of states of $LiMgBN_2$ (formation during the reaction (5)) was 1700-1874 cm^{-1} (Figure 7-2). The experimentally determined B-N stretching range was found to be 1682 - 1746 cm^{-1} after dehydrogenation of the Li-Mg-B-N-H system at 300 ^oC[128] which is in the high temperature range 225-325 ^oC. This B-N stretching information supports formation of the new phase $LiMgBN_2$ at temperatures above 300 ^oC.

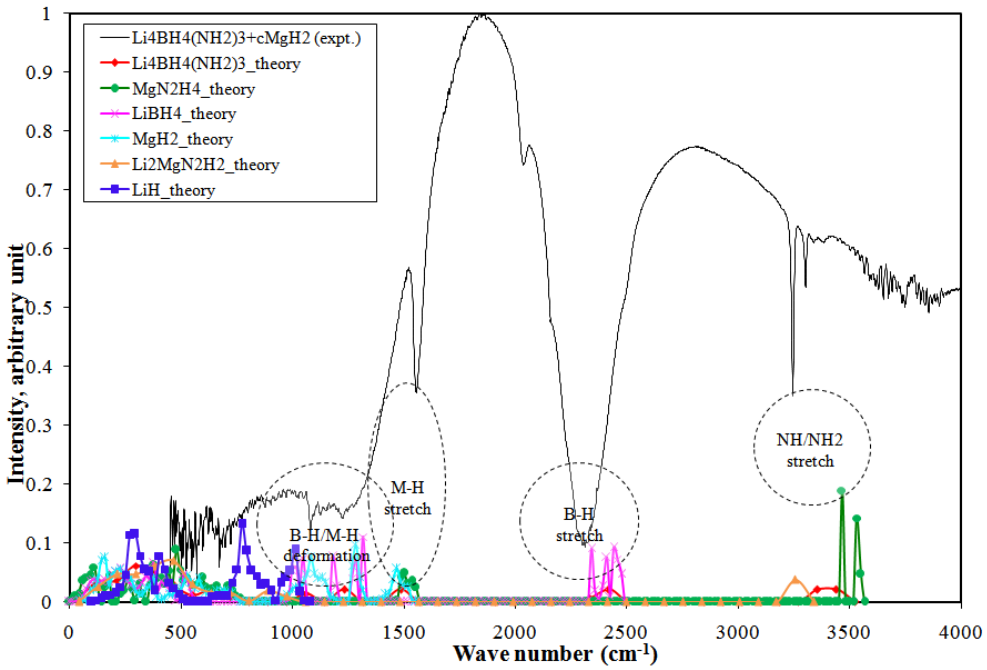

Figure 7-1. Normalized plot of experimental FTIR spectra of the $LiBH_4$-$LiNH_2$-MgH_2 systems and phonon density of states of intermediate states (*i.e.* ($Li_4BH_4(NH_2)_3$, $Mg(NH_2)_2$, $LiBH_4$, MgH_2, $Li_2Mg(NH)_2$ and LiH) during the first step hydrogen release reaction.

Table 7-1. Calculated ground state energy and zero point energy of different reactants/products:

Reactants/products	Space group (number)	Ground state energy (eV/f.u.)	ZPE, kJ/f.u. (cal. value)	ZPE, kJ/f.u. Ref.(lit. value)
$LiBH_4$	Monoclinic (9)	-23.91	107.20	[79]107.1
MgN_2H_4	Tetragonal (142)	-35.62	132.47	[122]134.8
$LiNH_2$	Tetragonal (82)	-19.05	68.26	[79]69.0
LiH	Cubic (225)	-6.17	21.02	[133]21.5
$Li_2MgN_2H_2$	Orthorhombic (45)	-33.09	85.95	[122, 133]86.9
Li_3N_2B	Tetragonal (141)	-34.37	50.33	[79]52.2
MgH_2	Tetragonal (136)	-8.98	39.69	[122]39.10
$Li_4N_3BH_{10}$	Cubic (199)	-81.93	314.10	[79]314.40
Mg_3N_2	Cubic (206)	-25.40	33.76	[122]33.20
$LiMgBN_2$	Tetragonal (142)	-31.57	45.87	NA
Mg	Hexagonal (194)	-1.48	2.94	[133]2.79
Li	Cubic (229)	-1.90	3.83	[79]3.9
B	Trigonal (166)	-6.48	12.61	[79]12.50
N_2		-16.66	15.66	[135]14.40
H_2		-6.78	28.29	[135]26.3

Based on the experimental thermal program desorption (TPD) hydrogen release profile[136], the reactions are categorized into four groups and they are mechanical milling (0-95 ^oC), first peak (95-160 ^oC), first shoulder peak (160-225 ^oC) and second peak (225-325 ^oC). The following different reactions in different temperature ranges were identified based on the PXRD and *in situ* IR spectroscopy data[119, 128].

Mechanical milling (0-95 ^oC)

$2LiBH_4 + 6LiNH_2 \rightarrow 2Li_4BH_4(NH_2)_3$ 7-1a

$2Li_4BH_4(NH_2)_3 + 3MgH_2 \rightarrow 3Mg(NH_2)_2 + 2LiBH_4 + 6LiH$ 7-1b

First peak (95-160 ^oC)

$2Li_4BH_4(NH_2)_3 + 3MgH_2 \rightarrow 3Li_2Mg(NH)_2 + 2LiBH_4 + 6H_2$ 7-2

Shoulder of first peak (160-225 oC)

$Mg(NH_2)_2 + 2LiH \Leftrightarrow Li_2Mg(NH)_2 + 2H_2$ 7-3

Second peak (225-325 ^oC)

$3Li_2Mg(NH)_2 + 2LiBH_4 \rightarrow 2Li_3BN_2 + Mg_3N_2 + 2LiH + 6H_2$ 7-4

$2Li_3BN_2 + Mg_3N_2 + LiBH_4 \rightarrow 3LiMgBN_2 + 4LiH$ 7-5

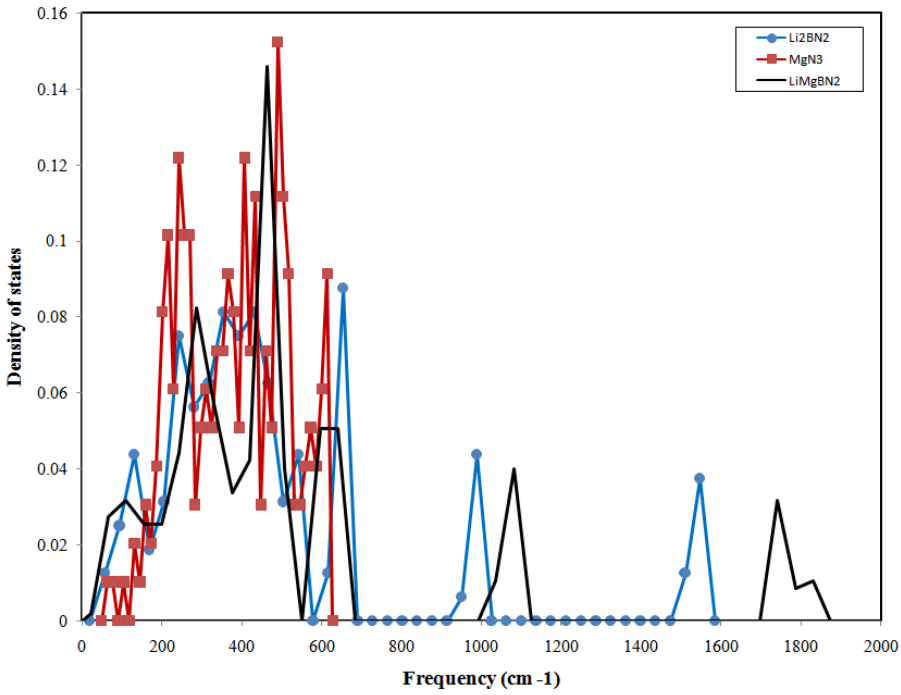

Figure 7-2. Normalized plot of phonon density of states of Li_3BN_2, MgN_3 and $LiMgBN_2$ (intermediate phases of Li-Mg-B-N-H system during second step hydrogen release).

7.4.2. Thermodynamics and reactions

The thermodynamic properties were calculated on the basis of the positive phonon DOS (example: Figures 7-1 and 7-2) and resulting vibrational energy contributions to the Gibbs energy by the direct method lattice dynamics. The solid and dotted lines (Figures (7-3) – (7-6)) represent the calculated and experimentally measured[111] results, respectively. The calculated thermodynamic functions: the enthalpy and the entropy are in good agreement with the experimental values for MgH_2, LiH, Mg_3N_2 and $LiBH_4$ (within ~8.5% of experimental values) crystal lattices.

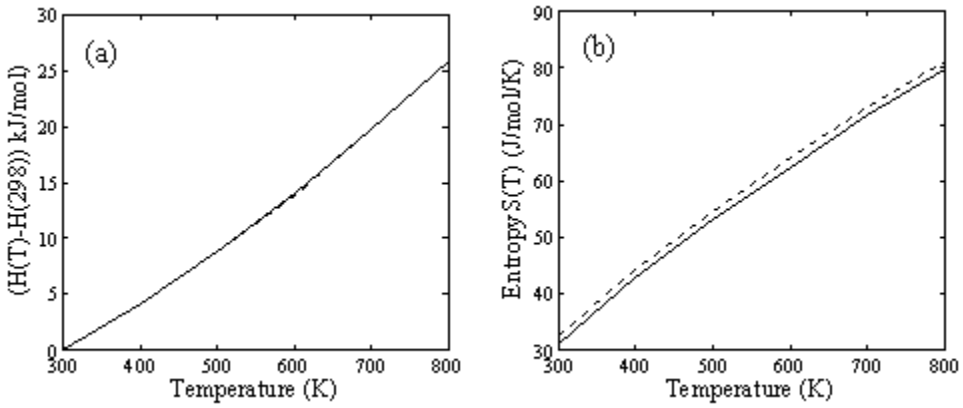

Figure 7-3. Calculated (solid line) and experimental[111] (dotted line) thermodynamic functions for MgH_2. The functions including the enthalpy (*H(T)−H(298)*) and the entropy (*S(T)*) are presented in (*a*) and (*b*), respectively. *H(298)* denotes the standard enthalpy at 298 K.

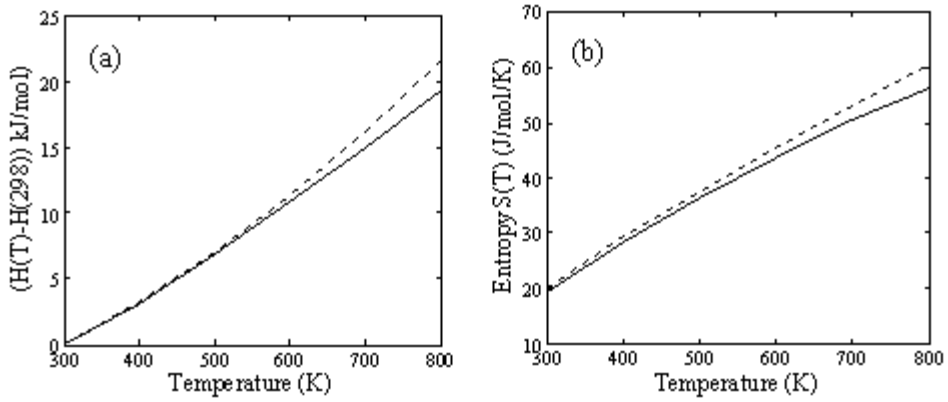

Figure 7-4. Calculated (solid line) and experimental[111] (dotted line) thermodynamic functions for LiH. The functions including the enthalpy (*H(T)−H(298)*) and the entropy (*S(T)*) are presented in (*a*) and (*b*), respectively. *H(298)* denotes the standard enthalpy at 298 K.

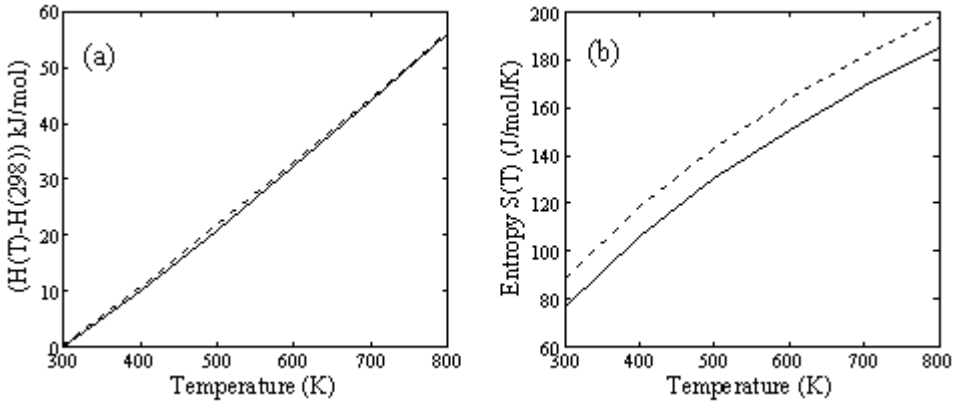

Figure 7-5. Calculated (solid line) and experimental[111] (dotted line) thermodynamic functions for Mg_3N_2. The functions including the enthalpy (*H(T)−H(298)*) and the entropy (*S(T)*) are presented in (*a*) and (*b*), respectively. *H(298)* denotes the standard enthalpy at 298 K.

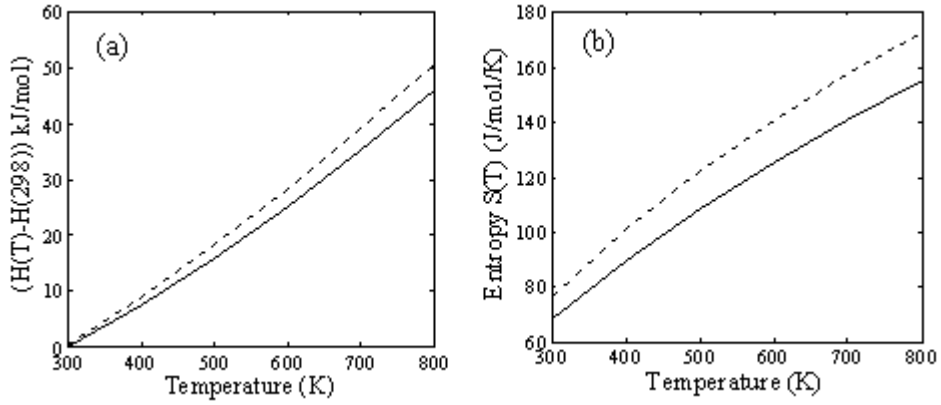

Figure 7-6. Calculated (solid line) and experimental[111] (dotted line) thermodynamic functions for $LiBH_4$. The functions including the enthalpy (*H(T)−H(298)*) and the entropy (*S(T)*) are presented in (*a*) and (*b*), respectively. *H(298)* denotes the standard enthalpy at 298 K.

For gas molecules (H_2 and N_2), one needs to know the Gibbs energy at the standard pressure of 1 atm. The vibrations cannot be treated directly from the phonon calculations for gas molecules because the phonon approach always considers the system as a crystal solid, and thus neglects the translational and rotational modes. The Gibbs energy of a gas molecule was calculated by combining both computational and experimental results presented in our earlier work[132].

The Gibbs energy calculations of these reactions (Figure 7-7) show that reactions (7-1a) and (7-1b) really do not have much Gibbs energy change with respect to temperature. This suggests that these two reactions are occurring due to the ball milling/mixing process and also do not release any hydrogen during the synthesis process. The first hydrogen release occurs *via* reaction (7-2) above 95 ^{o}C, which is also predicted from theoretical calculations as shown in Figure 7-7. Similarly, the shoulder peak due to reaction (7-3) is also supported by theoretical calculations. The second step

hydrogen release due to reaction (7-4) occurs at high temperature (>225 ^{o}C) which may be due to poor kinetics, not unfavorable thermodynamics. Formation of $LiMgBN_2$ occurs *via* reaction (7-5) at the end of the second step hydrogen release *i.e.* above 300 ^{o}C as discussed in the earlier section. The reaction enthalpy calculations of the hydrogen release reactions (Figure 7-8) show that the complete first step hydrogen release is endothermic and the second step is exothermic reaction.

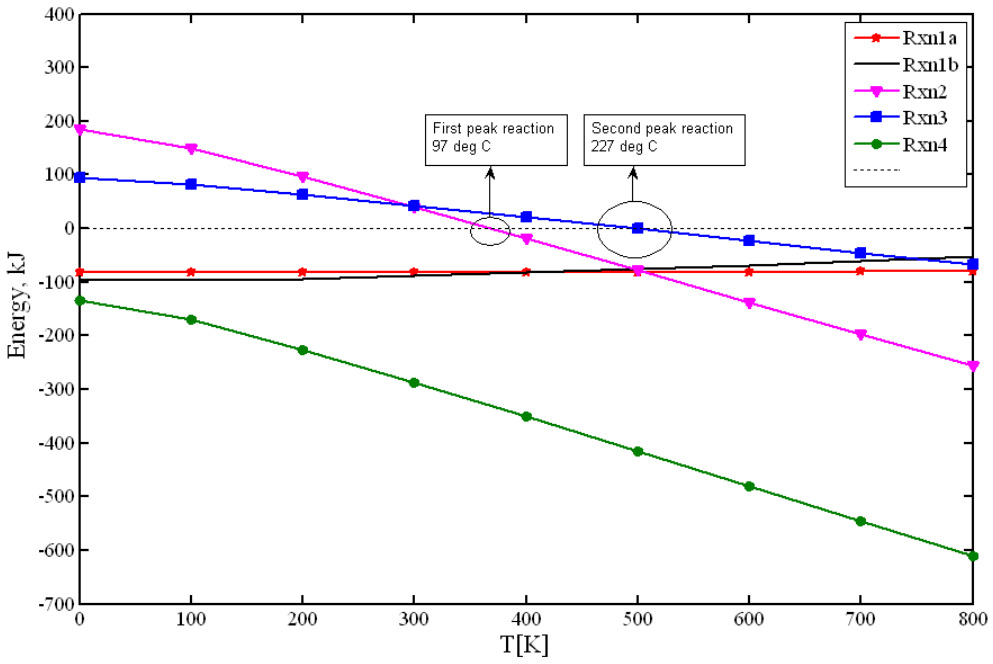

Figure 7-7. Temperature dependent Gibbs energy of reactions (7-1*a*, 7-1*b*, (7-2) – (7-4))

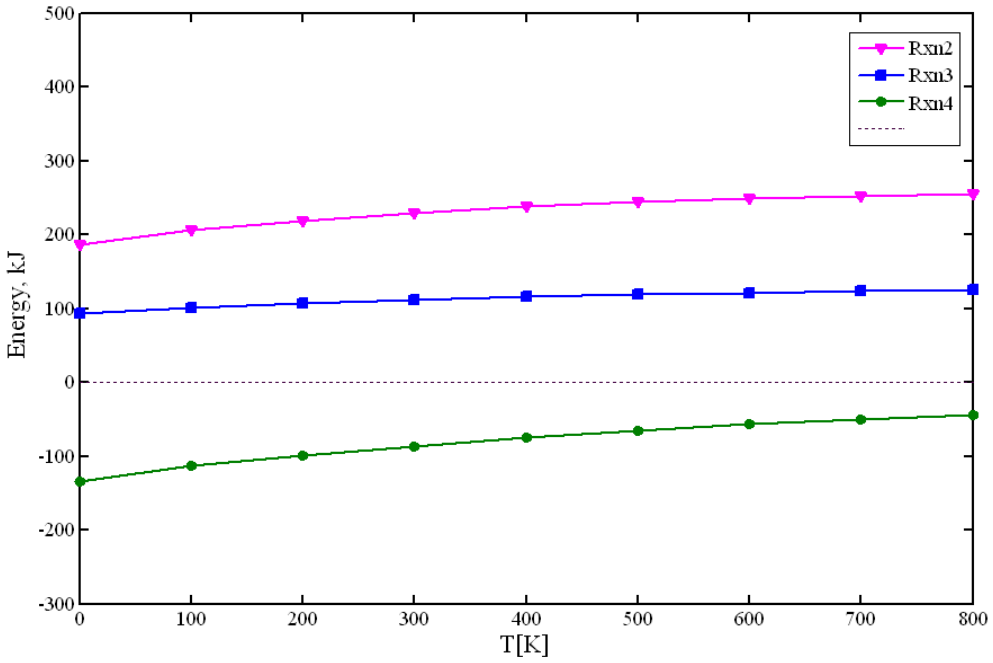

Figure 7-8. Temperature dependent reaction enthalpy of reactions ((7-2) – (7-4))

7.4.3. Quantitative analysis of hydrogen release

It is believed that during the synthesis of Li-Mg-B-N-H hydrogen storage system, initially, the quaternary phase ($Li_4BH_4(NH_2)_3$) formation (supported by phonon frequency of N-H and B-H stretching as shown in Figure 7-1) occurs (reaction (7-1a)) by intermixing/reacting with proportionate ratio of $LiNH_2$ and $LiBH_4$ and then half of this quaternary phase is destabilized by proportional amount of MgH_2 to produce the amide phase (reaction (7-1b)). The reactions (7-1a) and (7-1b) can be rewritten as below:

$$LiBH_4 + 2LiNH_2 \rightarrow \frac{2}{3}Li_4BH_4(NH_2)_3 + \frac{1}{3}LiBH_4 \qquad 7\text{-}6$$

$$\frac{1}{3}Li_4BH_4(NH_2)_3 + \frac{1}{2}MgH_2 \rightarrow \frac{1}{2}Mg(NH_2)_2 + \frac{1}{3}LiBH_4 + LiH \qquad 7\text{-}7$$

The unreacted quaternary phases then react with the residual MgH_2 at higher temperature according to reaction (7-2) to release the first hydrogen from the system. After reaction (7-2), the residue contains LiH, $Mg(NH_2)_2$, $LiBH_4$ and $Li_2Mg(NH)_2$. So, a hydrogen balance gives the amount of hydrogen released during the first step from the following equation:

$$2LiBH_4 + 8LiNH_2 + 4MgH_2 \rightarrow 4LiH + 2Mg(NH_2)_2 + 2LiBH_4 + 2Li_2Mg(NH)_2 + 4H_2 \quad 7\text{-}8$$

As the starting stoichiometric ratio of $LiNH_2$:$LiBH_4$:MgH_2 is kept constant with a 2:1:1 molar ratio, the above equation can be rewritten as follow:

$$LiBH_4 + 2LiNH_2 + MgH_2 \rightarrow LiH + \frac{1}{2}Mg(NH_2)_2 + LiBH_4 + \frac{1}{2}Li_2Mg(NH)_2 + H_2 \quad 7\text{-}9$$

Hence, the amount of hydrogen released during the first step is one mole per mole of starting materials, which is equivalent to approximately 2.19 wt%. Similarly, after the first shoulder peak reaction, the residue contains only $Li_2Mg(NH)_2$ and $LiBH_4$. This information can be supported by both *in situ* IR spectroscopy at 200 ^oC[128] and phonon frequency of N-H stretching from the imide and B-H stretching from $LiBH_4$ (Figure 7-1), respectively. The amount of hydrogen released in this shoulder peak step can be calculated from:

$$LiH + \frac{1}{2}Mg(NH_2)_2 + LiBH_4 + \frac{1}{2}Li_2Mg(NH)_2 \rightarrow LiBH_4 + Li_2Mg(NH)_2 + H_2 \quad 7\text{-}10$$

From reaction (7-10), the amount of hydrogen which can be released another 2.19 wt%, which is similar to that from the first shoulder peak. The total hydrogen released in the complete first step is 4.38 wt%. Similarly, based on the second step reaction, the amount of hydrogen released is two moles of hydrogen (~ 4.38 wt%) according to Equation (7-10). Finally, above 300 ^oC, residues are likely to form a new phase $LiMgBN_2$ according

to reaction (7-11). The quantitative summary of hydrogen release at different temperatures is given in Figure 7-9.

$$LiBH_4 + Li_2Mg(NH)_2 \rightarrow \frac{2}{3}Li_3BN_2 + \frac{1}{3}Mg_3N_2 + \frac{2}{3}LiH + \frac{1}{3}LiBH_4 + 2H_2 \quad (10)$$

$$\frac{2}{3}Li_3BN_2 + \frac{1}{3}Mg_3N_2 + \frac{1}{3}LiBH_4 + \frac{2}{3}LiH \rightarrow 2LiH + LiMgBN_2 \quad (11)$$

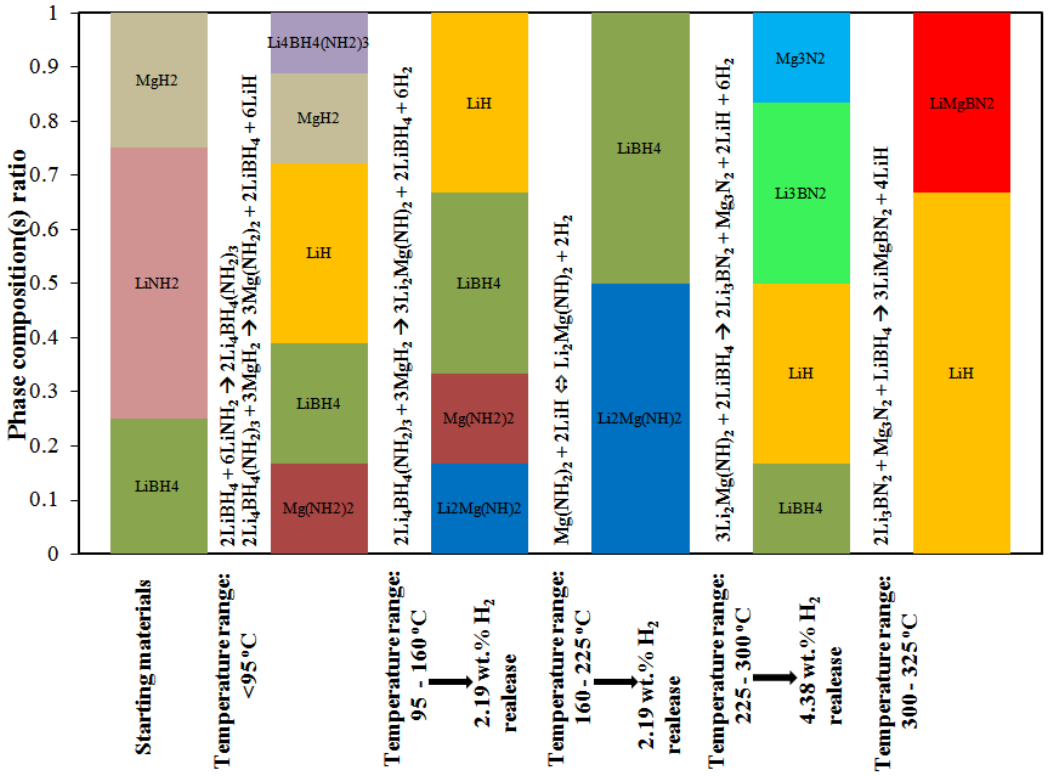

Figure 7-9. Normalized phase compositions of different reactants/products and also intermediate phases in different temperature ranges

7.4.4. Reversible reaction step and van't Hoff plot

We now discuss the thermodynamics of the reversible reaction, *i.e.*, reaction (7-3)[119, 121, 123, 128, 137, 138]. Using the calculated finite temperature thermodynamic properties

such as Gibbs energy and enthalpy of reactions (Figures 7-7 and 7-8) and entropy data as input to the van't Hoff equation, Figure 7-10 shows a plot of the equilibrium H_2 desorption pressures of the reversible reaction as a function of temperature. From our van't Hoff plot, the enthalpy of reversible re/de-hydrogenation of the Li-Mg-B-N-H multinary system is found to be 55.17 kJ/mol of H_2 which yields moderate H_2 pressures at elevated temperatures. This also confirms that the multinary system releases the desired amount of H_2 at higher temperatures than the fuel cell operating conditions shown in Figure 7-10. In other words, they are a little too strongly bound for practical, reversible on-board storage purposes. Catalytic doping may further lower the reversible dehydrogenation temperature and improve kinetics.

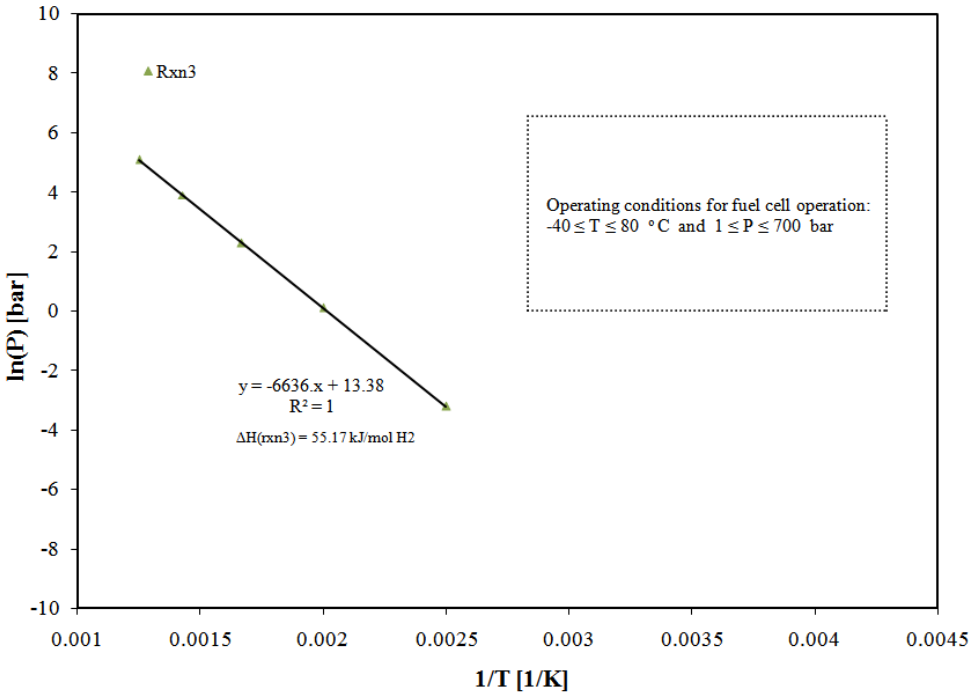

Figure 7-10. The van't Hoff plot derived from the theoretical calculations for the reaction:

$$Mg(NH_2)_2 + 2LiH \Leftrightarrow Li_2Mg(NH)_2 + 2H_2.$$

7.5. Summary

In this work, we have predicted the stability and dehydrogenation reactions at different temperatures of the complex multinary borohydride from theoretical calculations. This required investigation of both the ground state energy by DFT and the lattice vibration energy by the direct method lattice dynamics. The phonon dispersion relations and phonon density of states of the solid phases are calculated using a direct force-constant method. Using the phonon DOS and resulting vibrational energy contribution by the direct method lattice dynamics, the calculated thermodynamic functions including the enthalpy and the Gibbs energy are in good agreement with the experimental values for MgH_2, LiH, Mg_3N_2 and $LiBH_4$ crystal lattices.

The stability of the structures involved in a hydrogen desorption pathway was evaluated. The thermodynamic properties of these compounds were calculated and the feasibility of the mechanism was validated. It is found that all samples are intimate mixtures of $Li_4BN_3H_{10}$ with MgH_2 and that no new chemical compound is formed during the ball milling. This information was verified from both vibrational spectroscopy (B-H, Mg-H and N-H bond stretches; Figure 7-1) and Gibbs energy calculations (Figure 7-7). B-N stretching found at around 1700-1874 cm^{-1} (Figure 7-2) confirms the formation of $LiMgBN_2$ above 300 ^oC.

The reaction enthalpy calculations of the hydrogen release reactions (Figure 7-8) show that the complete first step hydrogen release is endothermic and the second step is exothermic. The total hydrogen storage capacity of this Li-Mg-B-N-H system is calculated to be 8.76 wt% from the desorption behavior observed at different temperatures up to 350 ^oC. Theoretical calculations also show that the multinary

complex borohydride exhibits first hydrogen release at a temperature of about 95 ^{o}C and then the main reversible hydrogen adsorption/desorption reaction (reaction (7-3)) occurs at a temperature of about 225 ^{o}C, which is a little higher than the experimentally determined temperature (190 ^{o}C)[136]. The quantitative reversible hydrogen storage capacity is found to be 4.38 wt% which is also different from the experimentally determined values of 2.5 wt% at 180 ^{o}C[128] (5-6 wt% at around 160 - 175 ^{o}C by adopting different processing reaction pathway schemes)[136].

The van't Hoff plot indicates that the enthalpy of reversible re/de-hydrogenation of Li-Mg-B-N-H multinary system to be 55.17 kJ/mol of H_2 which yields moderate H_2 pressure at elevated temperature only. This suggests that the multinary system release H_2 at higher temperatures, which is not the best situation for ideal fuel cell operation for onboard applications. However, this multinary system is the most promising reversible candidate compare to all other complex hydrides studied to-date. The reversible dehydrogenation temperature, kinetics and also storage capacity can be further improved *via* catalytic doping.

Finally, this type of combined DFT and lattice dynamics study could supplement experiments in testing complex multinary hydrides for hydrogen storage properties. These calculations are helpful in identifying feasible reactions and to rule out unrealistic possibilities, and arrive at practical hydrogen storage materials.

Chapter 8 - Experimental Study Of Li-Mn-B-H System

8.1. Abstract

In this work, we report the synthesis and characterization of $LiMn(BH_4)_3$, member of a new class of complex borohydrides for hydrogen storage. This new complex hydride was prepared with a 3:1 ratio of precursor materials $LiBH_4$ and $MnCl_2$ *via* the solid state mechano-chemical process. The B-H stretch occurrence at 2374 cm^{-1} in addition to two other B-H bonding bands of $LiBH_4$ (2228 and 2297 cm^{-1}) from the FTIR investigation confirm the formation of $LiMn(BH_4)_3$ at room temperature. Thermo gravimetric analysis (TGA) of $LiMn(BH_4)_3$ indicated that a large amount of hydrogen (~8.0 wt %) can be released between 135 and 155 °C in a single dehydrogenation reaction step. Reduction in the decomposition temperature was achieved by doping this Li-Mn-B-H system with small fractions of nano-Ni. An amount of 1.5 mol% nano-Ni was estimated and found to be the optimum concentration for effective decomposition. Nano-Ni loading in the host hydride lowers the melting and thermal decomposition temperatures (at least by 20 °C) as evidenced from the simultaneous TGA, DSC and TPD measurements. The doped $LiMn(BH_4)_3$ exhibits lower activation energy (112 kJ/mole) by 20 kJ/mole as compared to the undoped sample (131 kJ/mole). Moreover, the gas chromatography studies of the undoped and doped $LiMn(BH_4)_3$ demonstrate that the evolved gas is mainly hydrogen and does not contain members of the borane family.

8.2. Introduction

Hydrogen storage is considered to be the key component requiring a research breakthrough for streamlining hydrogen-based clean-fuel transportation[89, 139-141]. A recent challenge in hydrogen storage is to find light weight, low cost and high capacity hydrides with favorable hydrogen sorption kinetics and thermodynamics for on-board vehicular applications[138]. Complex chemical hydrides such as alanates[142-146], alanes[147, 148], borohydrides[126, 149], amides[150, 151] and their combinations[137, 152, 153] are widely investigated in recent years due to their high theoretical hydrogen capacity and tunable properties. The breakthrough discovery of Ti-doped $NaAlH_4$[154, 155] has renewed interest in revisiting these complex hydrides for reversible hydrogen storage. Although the Ti-doped alanates show reversible hydrogen storage behavior at moderate temperatures, these systems may not be ideal to realize the DOE 2010 and FreedomCAR technical targets[156]. This is due to the maximum usable hydrogen storage capacity of 5.4 wt% for $NaAlH_4$, which is considered to be well below the DOE target for 2010[157]. On the other hand, the borohydride complexes $NaBH_4$ and $LiBH_4$ possess high hydrogen storage capacity of 13.0 wt% and 19.6 wt%, respectively[47, 148, 158]. However, the release of hydrogen from $NaBH_4$ is possible only by hydrolysis (reaction with H_2O) and this process is irreversible[159]. For the case of $LiBH_4$, addition of SiO_2, significantly enhances its thermal desorption[160] at 200 °C. In general, the dehydrogenation and/or rehydrogenation of $NaBH_4$ or $LiBH_4$ are difficult to achieve because of the thermodynamic stability due to strong B-H interactions[45, 92]. New, less stable complex borohydrides, $Zn(BH_4)_2$ have been recently reported for hydrogen storage (~8.2 wt.%) at temperatures below 100 ^oC [48, 87, 93, 161]. However, it was found that thermal

decomposition of $Zn(BH_4)_2$ comprises of not only the evolution of H_2, but also of an appreciable amount of B–H (borane) compounds. Nanomaterial doping of the $Zn(BH_4)_2$ structure not only lowers the decomposition temperature by 20 ^oC but also suppresses the release of boranes, as found from both experimental and theoretical studies[94, 118]. Bi-alkali[162, 163] or alkali-transition metal borohydrides[164] also showed potential promise for hydrogen storage due to their high hydrogen capacity and tunable properties. In this paper, we report one such system, $LiMn(BH_4)_3$ prepared by the solid state mechano-chemical process. These materials are widely characterized using X-ray diffraction, Fourier-transformed infrared spectroscopy, thermo gravimetric analysis, differential scanning calorimetric analysis, temperature programmed desorption, hydrogen sorption (kinetics, PCT and cycle life) and gas chromatography. Additionally, doping of nanomaterials (e.g. nanoNi, nanoCo etc.) and the enhancement of hydrogen decomposition characteristics have been extensively studied on these new complex hydrides.

8.3. Experimental details

8.3.1. Materials and method

Starting materials $LiBH_4$ (90% purity), $MnCl_2$ (99% purity) nano-Zn (99.99%) and nano-Ti (99%) were obtained from Sigma Aldrich and other nano-dopants nano-Ni, nano-Co, nano-Fe, nano-Cu and nano-Pd (99.999%) were obtained from QuantumSphere Inc., CA, which were used without further purification. High purity H_2 (99.9999%), N_2 (99.99%) and He (99.99%) were procured from Airgas for the synthesis and analytical measurements. All chemical reactions and operations were performed in a nitrogen filled glove box. $LiBH_4$ and $MnCl_2$ at a 3:1 molar ratio were mixed in a stainless steel bowl

(80 ml) and the lid sealed with a viton O-ring in the glove box. The bowl was then evacuated for 30 minutes to remove residual oxygen and moisture down to ppm levels. A specially designed lid with inlet and outlet valves was used for this purpose.

The mechano-chemical process was done by high energy milling using the Fritsch pulversette planetary mono mill, P6, in an inert atmosphere. The milling parameters, ball to powder weight ratio and milling speed were optimized to 20:1 and 300 rpm, respectively. Milling duration of 20-30 minutes was maintained for all the samples. These mechano-chemically processed complex hydrides were immediately transferred to the glove box for further characterizations. In a similar way, a few mole concentrations of nano-dopants such as nano-Ni, nano-Co, nano-Fe, etc. were added during the milling process for the synthesis of nanomaterial doped $LiMn(BH_4)_3$.

8.3.2. X-ray diffraction

The powder X-ray diffraction of the mechano-chemically milled complex hydride was carried out by the Philips X'pert diffractometer with CuK_α radiation of λ = 5.4060 Å. The incident and diffraction slit widths used for the measurements are 1^o and 2^o, respectively. The incident mask of 10 mm was used for all the samples and their XRD studies. The sample holder (zero background silicon disc of 32 mm diameter procured from The Gem Dugout, Pennsylvania, USA) was covered with polyethylene tape (foil) with O-ring seal in a N_2 filled glove box to avoid the O_2/moisture pickup during the XRD measurements. Diffraction from the tape was calibrated without the actual sample and found to be occurring at the 2θ angles of 22^o and 24^o, respectively. The XRD phase identification and particle size calculation was carried out using the PANalytical X'pert Highscore software with built-in Scherer calculator.

8.3.3. Fourier transform infrared spectroscopy

The B–H bond stretch of the Li-Mn-B-H system was measured using a Perkin-Elmer *Spectrum One* FTIR spectrometer. This instrument operates in a single-beam mode and is capable of data collection over a wave number range of 370–7800 cm^{-1} with a resolution of 0.5 cm^{-1}. The complex borohydrides samples were palletized and sealed in a specially designed KBr cell for infrared measurements.

8.3.4. Simultaneous DSC and TGA

The simultaneous DSC and TGA (SDT) analysis pertaining to the weight loss and the heat flow for the reaction enthalpy during thermal decomposition of undoped and nanomaterial doped complex hydrides were performed by using the TA instrument's SDT-Q600 analytical tool. Calibration of SDT was performed in four steps with empty pan and standard sapphire disc. The four calibration subroutines of TGA weight, DTA baseline, DSC heat flow and temperature were carried out before an actual measurement on the sample. A pre-weighed sample was loaded into the ceramic pan and covered with the ceramic lid inside the glove box to prevent moisture from getting into the sample during transfer. A ramp rate of $2^{o}C$/min was used for all the measurements. TA's Universal Analysis 2000 software was used to analyze the TGA and DSC profiles.

8.3.5. Dehydrogenation kinetics: isothermal volumetric measurements

The isothermal volumetric measurements were carried out using Hy-Energy's PCTPro 2000 sorption equipment. This fully automated Sievert's type instrument uses an internal PID controlled pressure regulator with maximum pressure of 170 bars. It also includes five built-in and calibrated reservoir volumes of 4.66, 11.61, 160.11, 1021.30

and 1169.80 ml. The volume calibration without and with the sample was performed at a constant temperature with an accuracy of $\pm 1^{o}C$ using a helium gas. The software subroutines for hydrogen purging cycles, leak test, kinetics, PCT and cycling, etc. were performed by the HyDataV2.1 Lab-View program. The data collected from each run were analyzed using the Igor Pro 5.03 program using HyAnalysis Macro.

8.3.6. Temperature programmed desorption measurements

Temperature programmed desorption (TPD) measurement was carried out using the Autosorb-1 equipment of Quantachrome Instrument. A 100 to 120 mg amount of sample was loaded in the reactor and heated, in a 25 mL/min helium flow while heating from 25 to 200 °C at 5 ^{o}C/min. The thermal desorption/reduction profiles were recorded and analyzed using TPRWIN software package.

8.3.7. Gas chromatography analysis

It was observed in our previous study on $Zn(BH_4)_2$[88] that di-borane gas evolved in combination with H_2 during the thermal decomposition process. This feature turns the hydrides into irreversible systems obviating practical applications. In the current investigation, samples of both doped and undoped versions of the new complex borohydrides were subjected to gas chromatography analysis during the thermal programmed desorption process. The gas sample was injected (less than 50-100 micro liter) into the TCD detector and the GC signal recorded over a period of retention time. The gas analysis and plotting of the curves were carried out by Saturnview Version 5.52 software.

8.4. Theory

8.4.1. Activation energy calculations

For any chemical reaction, activation energy roughly corresponds to the height of the free energy barrier. The transition state along a reaction coordinate is the point of maximum free energy, where bond-making and bond-breaking are balanced. Multi-step reactions involve a number of transition states. Activation energy is also the minimum energy necessary for a specific chemical reaction to occur. The activation energy of a reaction is usually denoted by E_a, with units of kJ/mole. Activation energy can be reduced by doping of the complex hydrides as represented in Figure 8-1. The Arrhenius equation gives a quantitative basis for the relationship between the activation energy and the rate at which a reaction proceeds. From the Arrhenius equation, the basic rate equation can be expressed as

$$\frac{da}{dt} = A\exp(\frac{-E_a}{RT})\,f(a) \qquad 8\text{-}1$$

where, A is the frequency factor for the reaction, R is the universal gas constant, and T is the absolute temperature. This equation suggests that the activation energy is dependent on temperature, in the regimes in which the Arrhenius equation is valid. Thus E_a can be evaluated from the rate constant at any temperature (within the validity of the Arrhenius equation).

Experimentally, we have determined the activation energy of complex hydrides by temperature programmed desorption (TPD). Once a sample is saturated with Ar:H_2 (reactive gas, 95:5%) at a fixed temperature (normally near ambient), a flow of inert gas

and linear heating rate are applied to desorb previously adsorbed species (in our case it is H_2). Plots of $\ln(\beta/T_{max}^2)$ *vs.* $1/T_{max}$ yield a straight line with a slope $-E_a/R$, where E_a is the activation energy mentioned above for the hydrogen decomposition process or the bonding strength. Activation energy of undoped and doped $LiMn(BH_4)_3$ were estimated according to the Kissinger's theory[165] with the data obtained from TPD measurements of the samples with the ramping rates of 4, 10 and 20 ^oC/min.

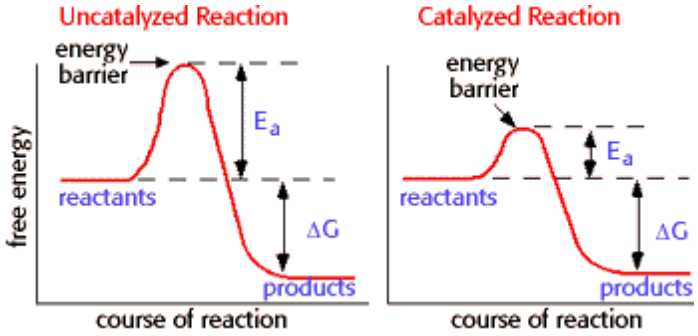

Figure 8-1. Activation energy curve (a) undoped and (b) catalytic doping reactions

8.5. Results and discussions

8.5.1. Formation of complex hydride $LiMn(BH_4)_3$ –FTIR and XRD explorations

Synthesis of the new complex hydride, $LiMn(BH_4)_3$ from the parent compounds $LiBH_4$ and $MnCl_2$ (3:1) was carried out in solid state employing the mechano-chemical milling process. The reactions proceed based on the stoichiometric ratio given in the Equation (8-2) below,

$3LiBH_4 + MnCl_2 \rightarrow LiMn(BH_4)_3 + 2LiCl$ 8-2

The B-H bonding environment of $LiMn(BH_4)_3$ prepared based on the above reaction was determined by the FTIR spectroscopic technique as shown in Figure 8-2. The FTIR spectra of BH_4^- ion in $LiBH_4$ has characteristic bands at 2224 and 2298 cm^{-1}, whereas the $LiMn(BH_4)_3$ structural phase shows a new peak at around 2374 cm^{-1} from the formation of the new complex hydride, in addition to showing the parent B-H stretch. The BH_2 bending modes are the same for both $LiMn(BH_4)_3$ and the parent compound $LiBH_4$.

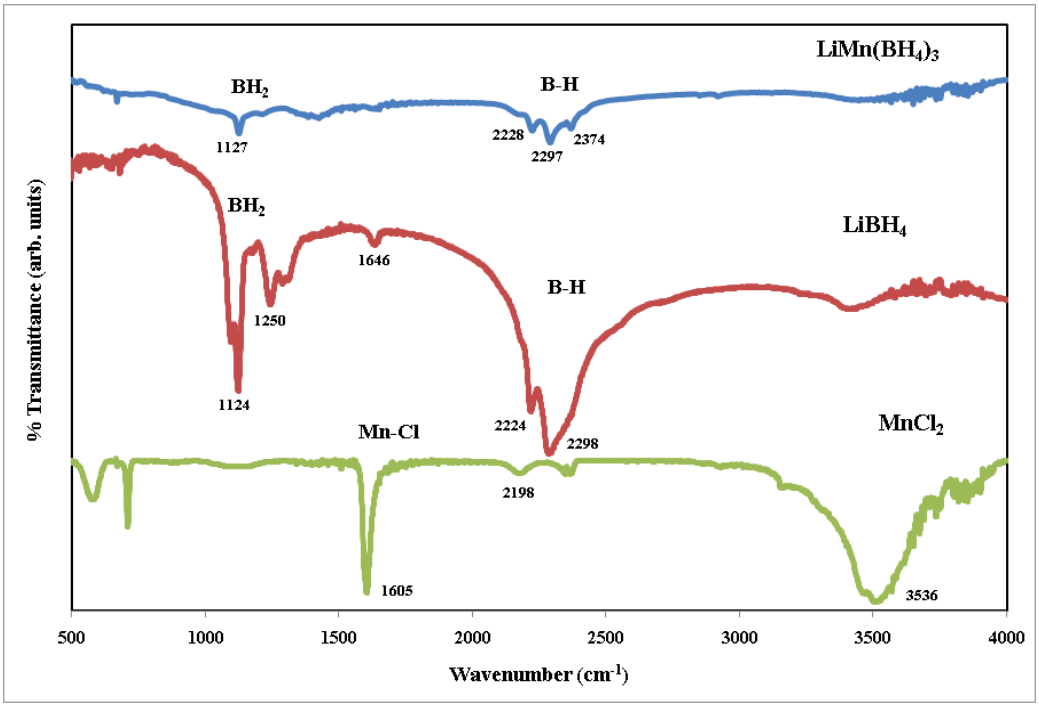

Figure 8-2. FTIR profiles of $LiBH_4$, $MnCl_2$, and $LiMn(BH_4)_3$ + 2LiCl ball milled mixture representing B-H bonding bands and BH_2 bending vibrations

Figure 8-3 represents the powder X-ray diffraction patterns of the pristine $LiBH_4$ and the complex mixture ($3LBH_4$+$MnCl_2$) mechanically milled in hydrogen ambient for 20 minutes. Bragg reflections with high crystalline phases were observed corresponding

to the presence of pure $LiBH_4$ for the parent compound. For the mixed complex hydrides, after the mechano-chemical reaction, the by-product consists of major LiCl peaks which agree well with reaction (8-2) above. Since $LiMn(BH_4)_3$ is not of highly crystalline nature, these peaks are not distinct. Nevertheless, both the FTIR and XRD spectra indirectly confirm the formation of the new complex hydride $LiMn(BH_4)_3$ from the reaction mixtures of $3LiBH_4$ and $MnCl_2$. We have also prepared these complex borohydrides with various concentrations of nanomaterial doping for enhancing hydrogen decomposition characteristics. The successful synthesis of new complex hydride, $LiMn(BH_4)_3$ and its doped counterparts were further evaluated by various other analytical studies such as TGA, DSC, TPD, PCT and GC which are elaborated in the following sections.

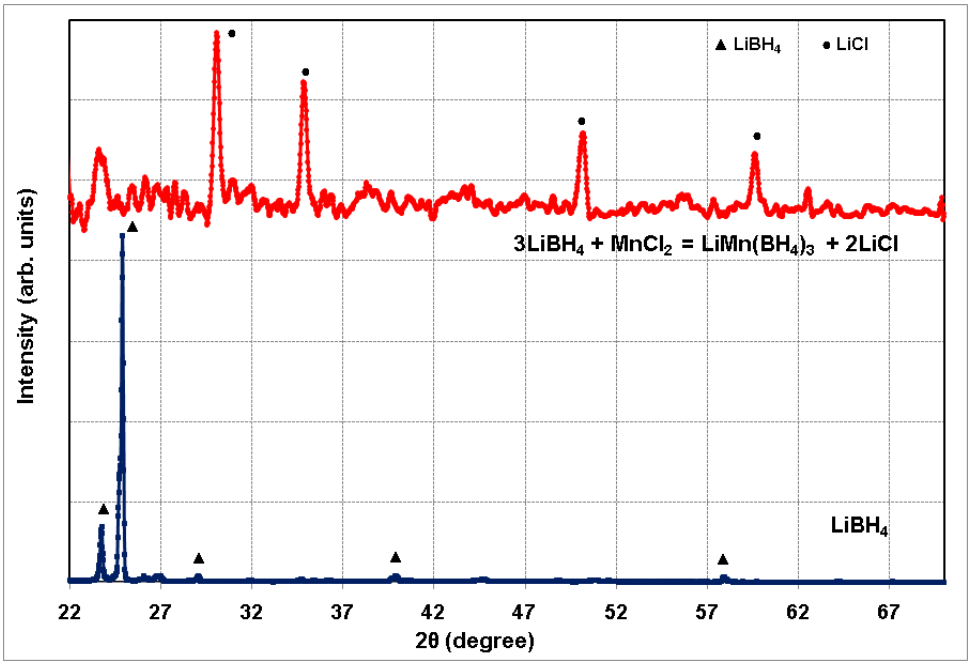

Figure 8-3. X-ray diffraction patterns of a pure $LiBH_4$ and $LiMn(BH_4)_3$+2LiCl mixture obtained after milling under H_2 ambient for 20 minutes

8.5.2. TGA, DSC and TPD studies of undoped and nanomaterials doped $LiMn(BH_4)_3$

We have demonstrated the successful preparation of new alkali-transition metal based complex borohydrides, $LiMn(BH_4)_3$ from the precursors of $LiBH_4$ and $MnCl_2$ by the mechano-chemical process. To reduce the decomposition temperature further, we have attempted to dope the $LiMn(BH_4)_3$ with different mole concentrations of nanomaterials (nano-Ni). It was clearly noticed that doping with nanoNi lowers the decomposition temperature and at the same time enhances the kinetics of the reaction. Optimization of nano-Ni concentration is extremely important for favorable hydrogen storage characteristics. We have studied the optimization procedures for doping $LiMn(BH_4)_3$ and the hydrogen storage characteristics of the resulting materials.

Figure 8-4 represents the simultaneous thermogravimetric (TGA) and differential scanning calorimetric (DSC) profiles of undoped and doped complex borohydrides, $LiMn(BH_4)_3$. Various molar concentrations (X=0, 0.5, 1, 1.5, 2, 2.5, 3) of nano-Ni were doped with the host borohydrides matrix. From Figure 8-4, it is clearly discernable that the doped samples exhibit at least 20-30 ^oC reduction in decomposition temperature (T_{dec}) compared to the undoped one (see also Table 8-1). Moreover, X=1.5 mol% of nano-Ni appears optimum in terms of the earlier on-set temperature and higher hydrogen desorption capacity. DSC profiles complimented this feature as observed from the earlier endothermic transition due to hydrogen decomposition. Based on this optimization of the concentration analysis, we have further carried out studies using various nanomaterial dopants (e.g. nano-Co, nano-Fe etc.) with the X fixed at 1.5 mol% and the results are shown in Figure 8-5.

By fixing the optimum concentration of nano-additive (X= 1.5mol%), the TGA and DSC spectra were obtained for several additives. Nano-Ni, nano-Co, nano-Fe, nano-Cu, nano-Ti, nano-Zn and nano-Pd were studied (see Figure 8-5). Similar to Figure 8-4, the doped $LiMn(BH_4)_3$ materials reveal earlier decomposition than the undoped samples. Among the various dopants, nano-Ni and nano-Co exhibit remarkable performance and in general the stabilities are ordered as *nanoNi* < *nanoCo* < *nanoFe* < *nanoTi* < *nanoZn* < *nanoCu* <*nanoPd* < *undoped*. Though nano-Co doping shows a much earlier on-set of decomposition temperature, the overall H_2 desorption amount is only half when compared to nano-Ni.

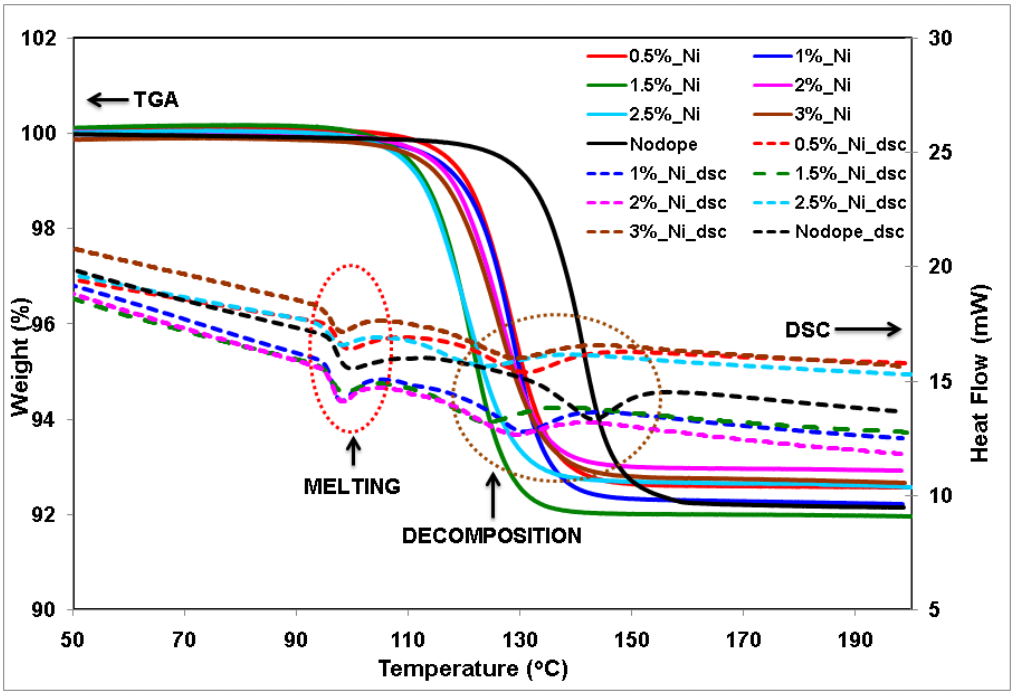

Figure 8-4. Simultaneous DSC and TGA profiles of $LiMn(BH_4)_3$ doped with Xmol% nanoNi, (X=0, 0.5, 1.0, 1.5, 2.0, 2.5, 3.0) ball milled for 20 minutes

Table 8-1. DSC and TGA analysis of undoped and nanoNi doped Li-Mn-B-H

X-mol% nanoNi doped $LiMn(BH_4)_3$	DSC melting transition (°C)	TGA On-set decomposition Temperature (°C)	TGA Peak decomposition Temperature (°C)	Weight loss (%)
Undoped	99	125	143	7.8
0.5	98	112	131	7.3
1.0	98	110	131	7.7
1.5	98	107	123	8.0
2.0	98	108	130	7.0
2.5	98	107	123	7.2
3.0	98	108	129	7.1

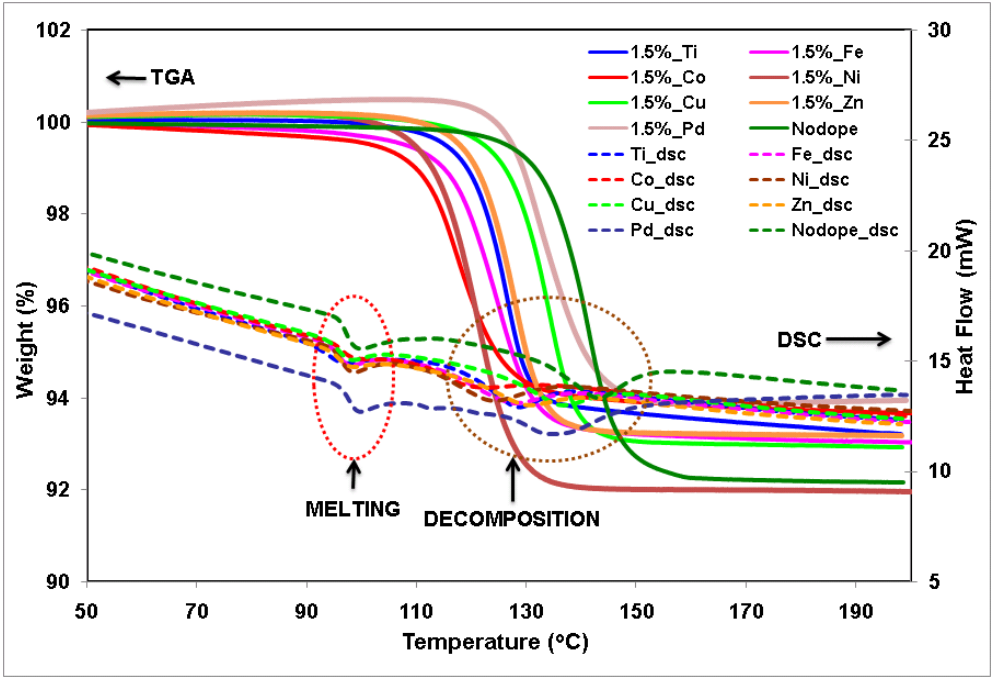

Figure 8-5. Simultaneous DSC and TGA profiles of $LiMn(BH_4)_3$ doped with various nanocatalysts (nanoNi, nanoCo, nanoFe, nanoCu, nanoTi and nanoZn) by fixing the concentration X=1.5mol% and ball milled for 20 minutes

The thermal desorption spectral (TPD) analysis shown in Figure 8-6 compliments the TGA measurements of Figure 8-5. Nano-Ni doped $LiMn(BH_4)_3$ exhibits earlier decomposition temperature with larger hydrogen release (obtained from the area under the curve) than the nano-Co doped one. Overall, the simultaneous TGA, DSC and TPD analyses of undoped and doped $LiMn(BH_4)_3$ reveal that nano-Ni doping with a concentration of 1.5mol% is the optimum system for effective hydrogen decomposition at lower temperatures.

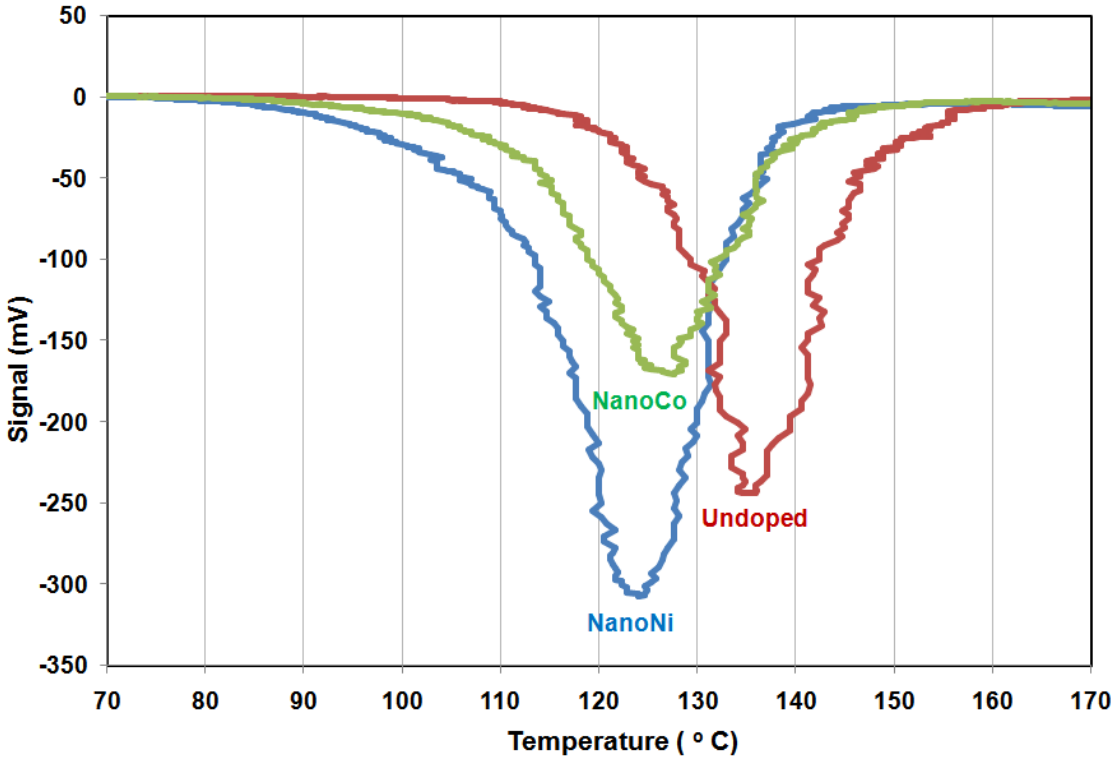

Figure 8-6. Thermal Programmed Desorption (TPD) profiles of undoped and Xmol% nanoNi and nanoCo doped $LiMn(BH_4)_3$; (X=1.5 mol%)

8.5.3. Dehydrogenation kinetics of undoped and nano-Ni doped $LiMn(BH_4)_3$

It is unambiguously seen from the TGA and TPD analyses that nano-Ni doping of 1-2 mol% destabilizes the structure with at least 10-20^{o}C reduction in hydrogen thermal decomposition temperature (T_{dec}). Moreover, the nano-Ni has greater effect on the hydrogen release (desorption kinetics) rate when compared to the undoped $LiMn(BH_4)_3$ as observed in Figure 8-7. The optimum concentration of nano-Ni was found to be 1-2 mol% which can speed up the initial decomposition reaction at least 2 to 3 times when compared to the undoped counterpart.

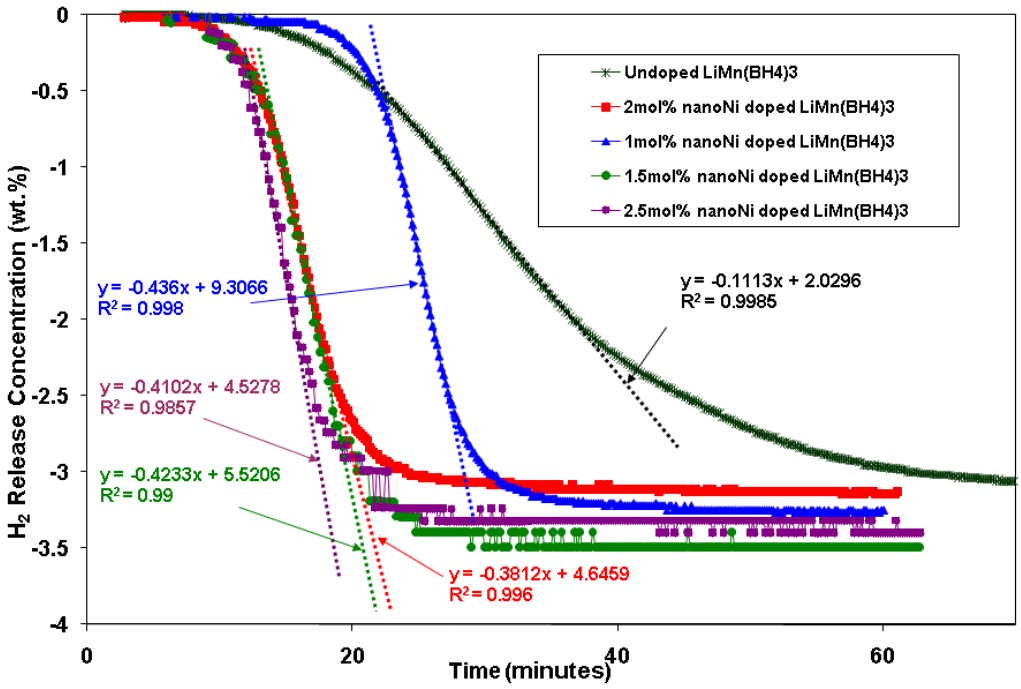

Figure 8-7. Dehydrogenaiton kinetics of undoped and Xmol% nanoNi (X=0.5, 1.0, 1.5, 2.0, and 2.5) doped $LiMn(BH_4)_3$

At lower concentration (1mol%) of nano-Ni, at least 3 to 4 fold increases in the rate of desorption is clearly seen as evidenced from Figure 8-7. A complete desorption from the nano-Ni (1 mol%) sample occurred within 40 minutes as compared to 70 minutes for the undoped sample. For the case of higher doping concentrations of nanocatalysts (1.5, 2 and 2.5 mol%), we see greater improvement in the desorption kinetics behavior when compared to the undoped and 1 mol% nano-Ni doped $LiMn(BH_4)_3$. It is also noteworthy to point out that the four-fold increase in the rate of desorption is still seen in these higher concentrations with the total hydrogen decomposition time found to be lowered from 40 to 20 minutes. Overall, the desorption kinetics profiles seem to agree well with the thermogravimetric analysis represented in Figures 8-4 and 8-5. Hence, it is concluded that the optimum dopant concentrations of 1.5-2.5 mol% are necessary for desorption-rate enhancement and lowering of the hydrogen decomposition temperature (also, refer to Table 8-1).

8.5.4. Activation energy calculations of undoped and nano-Ni doped $LiMn(BH_4)_3$

Based on Kissinger's theory and the approach discussed in Section 8.4, the thermal programmed desorption profiles of $LiMn(BH_4)_3$ at three different ramping rates of 4, 10 and 20 ^oC/min were collected The TPD spectra of undoped and nano-Ni doped $LiMn(BH_4)_3$ at these ramping temperatures are shown in Figure 8-8. The following can be seen in Figure 8-8: (i) TPD signal strength (corresponding to the hydrogen content) depends on the amount of sample used, (ii) uniform shift in T_{max} (temperature at the maximum desorption rate) with increasing the ramping rate in the order of 4>10>20 ^oC/min, (iii) shifting of the peak position independent of whether the sample is undoped

or nano-Ni doped and (iv) reduction in the decomposition temperature at the ramping rate of 4 ^{o}C/min in comparison to the 10 and 20 ^{o}C/min rates.

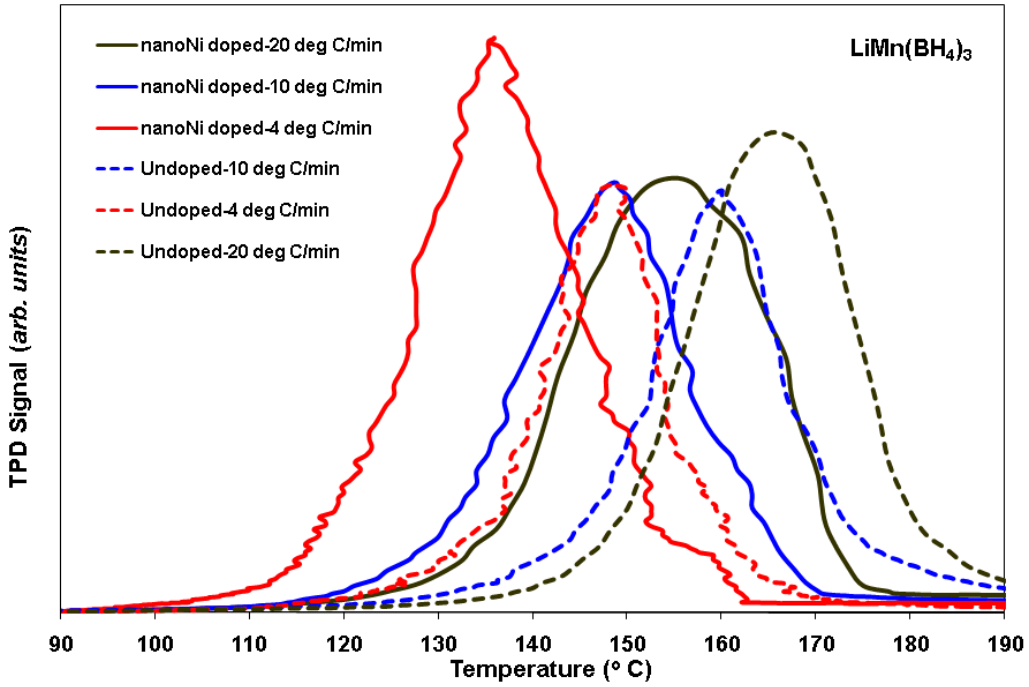

Figure 8-8. TPD spectra of undoped and 1.5mol% nanoNi doped $LiMn(BH_4)_3$ at various ramping rates (4, 10 and 20 ^{o}C/min)

The activation energy for H_2 desorption was calculated using the Kissinger analysis (see Figure 8-9) for both the undoped and nano-Ni doped $LiMn(BH_4)_3$ systems from the TPD data. The slope of the straight line plot of $\ln(\beta/T_{max}^2)$ vs $1/T_{max}$ yields the activation energy (E_a), which is a crucial parameter that needs to be optimized and investigated for efficient hydrogen storage. It is clearly seen from Figure 8-9 that the activation energy for the undoped $LiMn(BH_4)_3$ is 130.64 kJ/mol, whereas for the nano-doped samples, E_a can be lowered by at least 20 kJ/mole (for nano-Ni doped $LiMn(BH_4)_3$

E_a = 111.55 kJ/mole). Due to this lowering of the activation energy of nano-doped samples, about 20-30 ^oC reduction in the decomposition temperature was obtained from the thermogravimetric measurements.

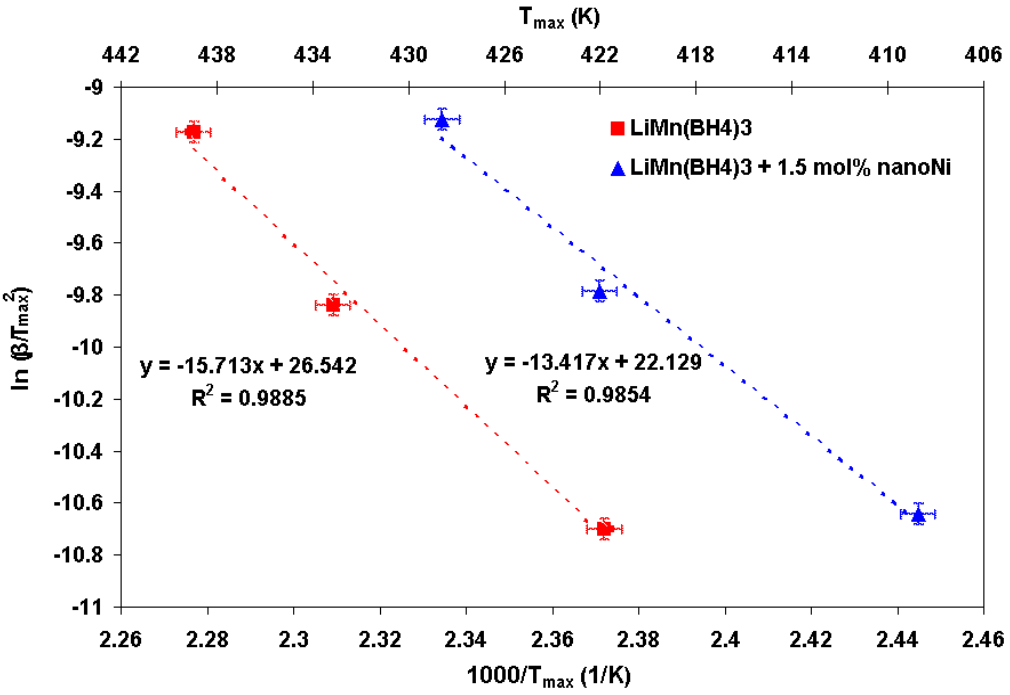

Figure 8-9. Kissinger's plot obtained from the TPD data for the undoped and 1.5 mol% nanoNi doped $LiMn(BH_4)_3$

8.5.5. GC analysis of undoped and nano-Ni doped $LiMn(BH_4)_3$

Figure 8-10 shows the GC analysis spectra of both undoped and 1.5 mol% nano-Ni doped $LiMn(BH_4)_3$. From this figure, it is estimated that no gas other than H_2 desorbed upon repeated sampling. Since the GC measurements are not capable of quantifying the amount of hydrogen desorbed during TPD process, additional Mass-spec analyses are required, which are in progress. Unlike $Zn(BH_4)_2$, the new complex

hydrides $LiMn(BH_4)_3$ releases a lot less or no borane family of gases during the decomposition process.

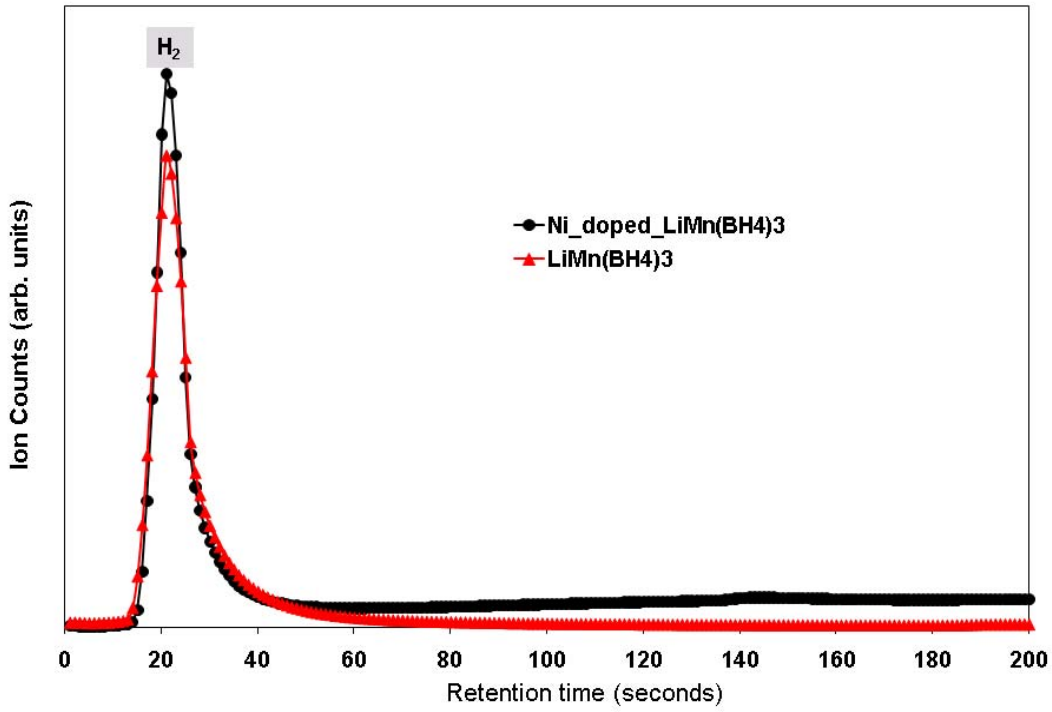

Figure 8-10. Gas Chromatography analysis of undoped and 1.5mol% nanoNi doped $LiMn(BH_4)_3$

8.5.6. Possible mechanism of nano Ni doping on the complex hydride $LiMn(BH_4)_3$

The enhancement of reaction kinetics at low temperatures and the requirement for high hydrogen storage capacity (> 6.0 wt.%) of complex borohydrides could be made possible by either adopting destabilization strategies or nanomaterial doping. If nanostructured materials with high surface area are used as the dopants, they may offer several advantages for the physico-chemical reactions, such as (i) surface interactions, (ii)

adsorption in addition to bulk absorption, (iii) rapid kinetics, (iv) low temperature sorption, (v) hydrogen atom dissociation and molecular diffusion via the surface catalyst. The intrinsically large surface areas and unique adsorbing properties of nanophase dopants can assist the dissociation of gaseous hydrogen molecules and the small volume of individual nanoparticles can produce short diffusion paths to the materials' interiors. The use of nanosized dopants enables a higher dispersion of the catalytically active species[166] and thus facilitates mass transfer reactions. Based on our previous studies on the nickel doped $Zn(BH_4)_2$[88, 94], it is easily discernible that by nanomaterial doping, both the reduction of decomposition temperature and the cohesive energy of the complex hydrides are established. Hence, the hydrogen transfer reactions and breaking of B-H bonds have been facilitated by the Ni- dopants. However, further experimental and theoretical studies to determine the exact mechanism of nanomaterials doped complex hydrides are necessary.

8.6. Summary

In this work, an inexpensive mechano-chemical approach of ball milling technique was utilized to prepare a member of a new class of solvent-free, solid-state complex borohydrides (Li-Mn-B-H) for on-board hydrogen storage. It is found that the endothermic transition due to hydrogen or other gaseous decomposition from the Li-Mn-B-H system occurs with onset below 100^{o}C and a complete decomposition occur at 150 ^{o}C. To reduce the decomposition temperature further, we attempted to dope the $LiMn(BH_4)_3$ system with different molar concentrations of nanodopants such as nano-Ni, nano-Co, and nano-Fe. Thermo gravimetric (TGA) and desorption kinetic profiles of the undoped and nano-doped Li-Mn-B-H system show that the nanodopant materials have

pronounced effects on the hydrogen release kinetics while lowering the decomposition temperature. Moreover, the nano-doped $LiMn(BH_4)_3$ exhibits lower activation energy (112 kJ/mol) by 20 kJ/mol in comparison to the undoped sample (131 kJ/mol).

Though this Li-Mn-B-H complex borohydride exhibits high theoretical hydrogen storage capacity (8-10wt.%) at lower temperature (<150^{o}C), the reversible hydrogenation and dehydrogenation cycling is not promising. This may be due to either the strong B-H interaction or the formation of MnB_2 structure. Further investigations are required using various destabilization mechanisms and strategies for these new materials to evaluate the reversible hydrogen kinetics and storage capacity which is the further recommendation for future work.

Chapter 9 - Summary, conclusions and recommendations

9.1. Overview

The challenge is clear and fascinating: supplying abundant amounts of clean energy; consuming less natural resources and finding the appropriate solutions for any corner of the world. Both fundamental theoretical and experimental research is needed to understand the interaction of hydrogen in solid-state materials to realize the potential of these materials for hydrogen storage.

In this dissertation, we have used combined-first-principles using density functional theory (DFT) and direct method lattice dynamics calculations to understand the properties for hydrogen storage materials, mainly focused on complex borohydrides. This allowed us to establish stability of the crystal structure at finite temperatures using the positive definite frequency distribution criteria of the phonon spectra over the Brillion zone. DFT was used to calculate electronic properties and the direct method lattice dynamics was used to calculate the finite temperature thermal properties. The calculated thermodynamic functions: the enthalpy and the entropy are in good agreement with the experimental values for solid (within the acceptable limit of experimental values) crystal lattices. The Gibbs energy of crystal solid can then be predicted by usual thermodynamic relation between enthalpy, entropy and Gibbs energy. For gas molecules (H_2 and N_2), one needs to know the Gibbs energy at the standard pressure of 1 atm. The Gibbs

energy of a gas molecule was calculated by combining both computational and experimental results as described earlier in Chapter 6. Once the temperature dependent Gibbs energy and entropy are predicted for each element or compound (reactants and products), the reaction thermodynamics can be predicted easily. A number of borohydride systems have been studied using combined first principles and lattice dynamics simulations including for instance zinc borohydride, manganese borohydride and multinary borohydride system. At last, a systematic study has also been carried out for a new type of complex borohydride *i.e.* lithium manganese borohydride system by various experimental techniques. Nano additives were also added to this complex borohydride to study the effect of nano additives and found that the nanodopant materials have destabilized the system to allow for hydrogen storage at lower temperatures and with faster kinetics.

9.2. $Zn(BH_4)_2$ – conclusions and recommendations

It is found that $Zn(BH_4)_2$ is an insulating material having a wide band gap. Electronic structure calculations show strong bonding between hydrogen atoms and boron in the $[BH_4]^-$ complex and also less polar bonding between the Zn and the hydrogen atom. The simulated standard enthalpy of dehydrogenation of $Zn(BH_4)_2$ suggests that decomposition to primary elements is the most favorable one. The findings of our work are in qualitative agreement with experimental results. It is also found that Ni doping improves the dehydrogenation mechanism of this complex borohydride by reducing both the decomposition temperature and cohesive energy of the complex borohydride. Ni has greater affinity towards H atoms and these H atoms are pulled towards these doped Ni atoms and thus affects both low (librational) and high (bending)

frequency modes of the nearest BH_4 complex, which introduces instability *via* the breaking of multiple B-H bonds in the complex borohydride. However, experimentally it was reported that thermal decomposition of $Zn(BH_4)_2$ comprises not only of the evolution of H_2, but also production of an appreciable amount of B–H (borane) compounds. Although Ni dopant lowers the decomposition temperature but still lead to negligible release of boranes and thus, $Zn(BH_4)_2$ cannot be considered as suitable hydrogen storage material.

9.3. $Mn(BH_4)_2$ – conclusions and recommendations

Manganese borohydride ($Mn(BH_4)_2$) is a high theoretical capacity (~10 wt%) solid-state hydrogen storage candidate. $Mn(BH_4)_2$ is found to be tetragonal type structure of space group *I-4m2*. The most feasible dehydrogenation reaction is found to be an endothermic reaction at decomposition temperature. The spin polarized electronic density of states studies reveal that Mn partial 3*d* DOS has metallic character for spin-up and insulating character for spindown projection, are supposed to show some intermediate behavior, which suggests that the $Mn(BH_4)_2$ is a half-metallic hydrogen storage material. The electronic structure analysis shows that the interaction between Mn atoms and BH_4 complexes has an ionic character while the internal bonding of BH_4 is essentially covalent. The theoretical vibrational characterization of manganese borohydride is also well compared with experimental results. The dehydrogenation thermodynamics suggest that the crystal structure is stable at finite temperature and no diborane as a dehydrogenation product is preferred thermodynamically. Thus, complex borohydride of manganese could be considered a potential candidate for hydrogen

storage. However, one needs to address the reversibility issue before its practical on-board applications.

9.4. Li-Mg-B-N-H – conclusions and recommendations

In this work, we have predicted the stability and dehydrogenation reactions at different temperatures of the reversible complex multinary borohydride system from theoretical calculations. The stability of the structures involved in a hydrogen desorption pathway is validated *via*. phonon calculations. The thermodynamic properties of these compounds are then calculated and the feasibility of the mechanism is validated. It is found that all samples are intimate mixtures of $Li_4BN_3H_{10}$ with MgH_2 and that no new chemical compound is formed during the ball milling. This information is verified from both vibrational spectroscopy (B-H, Mg-H and N-H bond stretches; Figure 7-1) and Gibbs energy calculations (Figure 7-8).

The reaction enthalpy calculations of the hydrogen release reactions (Figure 7-9) show that the complete first step hydrogen release is endothermic and the second step is exothermic. The total hydrogen storage capacity of this Li-Mg-B-N-H system is calculated to be 8.76 wt% from the desorption behavior observed at different temperatures up to 350 ^{o}C. Theoretical calculations also show that the multinary complex borohydride exhibits first hydrogen release at a temperature of about 95 ^{o}C and then the main reversible hydrogen adsorption/desorption reaction (reaction (7-3)) occurs at a temperature of about 225 ^{o}C, which is a little higher than the experimentally determined temperature (190 ^{o}C)[136]. The quantitative reversible hydrogen storage capacity is found to be 4.38 wt% which is also different from the experimentally determined values of 2.5 wt% at 180 ^{o}C[128] (5-6 wt% at around 160 - 175 ^{o}C by adopting

different processing reaction pathway schemes in our clean energy research group at University of South Florida).

The enthalpy of reversible re/de-hydrogenation of Li-Mg-B-N-H multinary system is found to be 55.17 kJ/mol of H_2 which yields moderate H_2 pressure at elevated temperature only (Figure 7-11). This suggests that the multinary system release H_2 at higher temperatures, which is not the best situation for ideal fuel cell operation for onboard applications. However, this multinary system is the most promising reversible candidate compare to all other complex hydrides studied to-date. The reversible dehydrogenation temperature, kinetics and also storage capacity can be further improved *via* catalytic doping, which is the further recommendation for future work.

9.5. Li-Mn-B-H – conclusions and recommendations

Complex borohydride of manganese system, member of a new class of complex borohydrides for hydrogen storage can be prepared with a 3:1 ratio of precursor materials $LiBH_4$ and $MnCl_2$ *via* the solid state mechano-chemical process. The occurrence of B-H stretch at three different frequency bands from the Fourier transform infrared spectrometer (FTIR) investigation confirm the formation of $LiMn(BH_4)_3$ at room temperature. It is found that the XRD analysis of milled sample shows only LiCl (product) peaks. Since $LiMn(BH_4)_3$ is not of highly crystalline nature, the direct XRD peaks are not distinct for Li-Mn-B-H system. Nevertheless, both the FTIR and XRD spectra indirectly confirm the formation of the new complex hydride $LiMn(BH_4)_3$ from the reaction mixtures of $3LiBH_4$ and $MnCl_2$. It is also found that a large amount of hydrogen (~8.0 wt %) can be released below 150 °C in a single dehydrogenation reaction step from the thermo gravimetric analysis (TGA) of $LiMn(BH_4)_3$. Furthermore, a

significant reduction in the decomposition temperature can be achieved *via*. catalytic doping of small fractions of nano-Ni to $LiMn(BH_4)_3$ system. The doped $LiMn(BH_4)_3$ exhibits lower activation energy by ~20 kJ/mol in comparison to the undoped sample. Thermo gravimetric (TGA) and desorption kinetic profiles of the undoped and nano-materials doped Li-Mn-B-H system show that the nanodopant materials have pronounced effects on the hydrogen release kinetics while lowering the decomposition temperature. Moreover, the gas chromatography studies of the undoped and doped $LiMn(BH_4)_3$ demonstrate that the evolved gas is mainly hydrogen and does not contain members of the borane family.

Though this Li-Mn-B-H complex borohydride exhibits high theoretical hydrogen storage capacity (8-10 wt%) at lower temperature (<150^{o}C), the reversible hydrogenation and dehydrogenation cycling is not promising. This may be due to either the strong B-H interaction or the formation of MnB_2 structure. Further investigations are required using various destabilization mechanisms and strategies for these new materials to evaluate the reversible hydrogen kinetics and storage capacity which is the further recommendation for future work.

9.6. Major contributions

The contributions of this dissertation to the field of hydrogen storage research are multifold. It develops a fundamental understanding of the hydrogen storage materials mainly focused on complex borohydrides. This study finds the stable crystal structure, electronic structure and nature of chemical bondings of new borohydride complexes, identifies the favorable dehydrogenation reaction and associated thermodynamics, and also unravels the local hydrogen dynamics and storage capacity of the complex

borohydride with additive materials. Finally, this type of combined DFT and lattice dynamics study could supplement experiments in testing complex multinary hydrides for hydrogen storage properties. These calculations are helpful in identifying feasible reactions and to rule out unrealistic possibilities, and arrive at practical hydrogen storage materials. The fundamental theoretical simulations in this research will not only benefit the design of novel solid state borohydride materials, but also establish thermodynamic "guidelines" which are used to help guide reactions and design other suitable nanostructured materials.

The broader impact of the research is to prepare and gain fundamental insights for new hydrogen storage materials which can lead to the design of compact, lightweight, responsive, and affordable hydrogen storage materials which can have 5-10 kg (depending on the size of the vehicle) of usable hydrogen which can enable 480–km (300-miles) driving range in a single fueling. Improved physico-chemical reactions of hydrogen with solid state complexes will also have broad impact on our society to develop zero emission fuel cell vehicles, to mitigate the global warming effects and to supply inexpensive and plentiful clean energy for our current standard of living.

An improvement in the fundamental understanding of the thermal characteristics and adsorption/desorption dynamics of gases on these complex hydrides would contribute to the research studies being carried in catalysis. The modeling techniques used in the present study can be extended to a wide range of other systems.

9.7. Future work directions

Kinetics is emerging as the most important challenge for theory because of the time scale of the hydrogen evolution. The general time scale for quantum mechanical

simulations to evaluate atomic forces is in the order of picoseconds but simulations using empirical and semi-empirical potential energy functions can go up to the order of nanoseconds. Mesoscale simulations, such as kinetic Monte Carlo, can cover up to the time scales in seconds, and continuum methods can cover up to the time scales from seconds to hours. As the time scales for the hydrogen evolutions is in the order of seconds to hour and thus poses serious challenges for theory and computation. The real challenge is to integrate these approaches so that predictions of real materials behavior can be made with a solid physical and chemical basis. Hydrogen storage materials should be studied not only from the catalytic chemistry point of view, but also from the microstructural evolution point of view.

For the experimental work, the preliminary results of PCT experiments for the destabilization of $LiMn(BH_4)_3$ by few mol % of MgH_2 shows that the system becomes reversible at least by 3.0 wt% including the dead weight (*i.e.* LiCl) at low temperature at around 100 ^{o}C. The detail study needs to be done further to understand the exact mechanism of the system and also to find the optimum quantity of MgH_2 for the higher reversible capacity. Moreover, synthesis of the $LiMn(BH_4)_3$ system should be done by solution synthesis method to make single crystal to find the exact structural parameters of the complex borohydride. This method can eradicate the dead weight (*i.e.* LiCl) present in the system during the synthesis of the complex borohydride from its precursor materials using mechanochemical process. Otherwise a novel separation technique needs to be developed to extract the dead weight from the system after mechanochemical process is further recommendation for future work.

References

1. Dresselhaus, M. S.; Thomas, I. L., Alternative energy technologies. *Nature* 2001, 414, 332-337.

2. Fontes, E.; Nilsson, E., Modeling the Fuel Cell. *The Industrial Physicist* 2001, 14-17.

3. Züttel, A., Hydrogen storage methods. *Naturwissenschaften* 2004, 91, 157-172.

4. Dillion, A. C.; Jones, K. M.; Bekkedahl, T. A.; Kiang, C. H.; Bethune, D. S.; Heben, M. J., Storage of hydrogen in single-walled carbon nanotubes. *Nature* 1997, 386, 377-379.

5. Rosi, N. L.; Eckert, J.; Eddaoudi, M.; Vodak, D. T.; Kim, J.; O'Keeffe, M.; O.M. Yaghi, Hydrogen Storage in Microporous Metal-Organic Frameworks. *Science* 2003, 300, 1127-1129.

6. Cho, S. J.; Song, K. S.; Kim, J. W.; Kim, T. H.; Choo, K., Fuel Chem Div Prepr. 2002, 47, 790.

7. Johanson, E. Synthesis and characterisation of potential hydrogen storage materials. Ph.D., University of Uppsala, 2001.

8. Hohenberg, P.; Kohn, W., Inhomogeneous electron gas. *Physical Review* 1964, 136, B864–71.

9. Kohn, W.; Sham, L. J., Self-consistent equations including exchange and correlation effects. *Physical Review* 1965, 140, A1133–38.

10. Jones, R. O.; Gunnarsson, O., The density functional formalism, its applications and prospects. *Rev. Mod. Phys.* 1989, 61, (3), 689-746.

11. Perdew, J. P.; Wang, Y., Correlation hole of the spin-polarized electrongas, with exact small-wave-vector and high-density scaling. *Physical Review B* 1991, 44, 13298–13307.

12. Becke, A. D., Density-functional thermochemistry III. The role of exact exchange. *J. Chem. Phys.* 1993, 98, 5648.

13. Burke, K.; Ernzerhof, M.; Perdew, J. P., The adiabatic connection method: a non-empirical hybrid. *Chem. Phys. Lett.* 1997, 265, 115-120.

14. Wigner, E. P., The transition-state method. *Transactions of the Faraday Society* 1938, 34, 29–41.

15. Ceperley, D. M., Ground-state of the fermion one-component plasma - montecarlo study in 2 and 3 dimensions. *Physical Review B* 1978, 18, 3126–3138.

16. Ceperley, D. M.; Alder, B. J., Ground-state of the electron-gas by a stochastic method. *Phys. Rev. Lett.* 1980, 45, 566–569.

17. Becke, A. D., Density-functional thermochemistry for a new dynamical correlation functional and implications for exact-exchange mixing. *J. Chem. Phys.* 1996, 104, 1040-1046.

18. Kresse, G.; Furthmüller, J., Efficiency of ab-initio total energy calculations for metals and semiconductors using a plane-wave basis set. *Comput. Mater. Sci.* 1996, 6, 15.

19. Kittel, C., *Introduction to Solid State Physics*. Wiley: 1996.

20. Phillips, J. C., Energy-band interpolation scheme based on a pseudopotential. *Phys. Rev.* 1958, 1, 685–695.

21. Antoncik, E., Approximate formulation of the orthogonalized plane-wave method. *J. Phys. Chem. Solids* 1959, 10, 314.

22. http://en.wikipedia.org/wiki/Pseudopotential.

23. Vanderbilt, D., Soft self-consistent pseudopotentials in generalized eigenvalue formalism. *Phys. Rev. B* 1990, 41, (11), 7892.

24. Blochl, P. E., Generalized separable potentials for electronic-structure calculations. *Phys. Rev. B* 1990, 41, 5414-5416.

25. Blöchl, P. E., Projector augmented-wave method. *Phys. Rev. B* 1994, 50, (24), 17953.

26. Kresse, G.; Hafner, J., Ab initio molecular dynamics for liquid metals. *Phys. Rev. B* 1993, 47, (1), 558.

27. Kresse, G.; Furthmüller, J., Efficient iterative schemes for ab initio total-energy calculations using a plane-wave basis set. *Phys. Rev. B* 1996, 54, (16), 11169.

28. Baroni, S.; Gironcoli, S. d.; Giannozzi, P., Phonon dispersions in $Ga_xAl_{1-x}As$ alloys. *Phys. Rev. Lett.* 1990, 65, (1), 84.

29. Baroni, S.; Giannozzi, P.; Testa, A., Green's-function approach to linear response in solids. *Phys. Rev. Lett.* 1987, 58, (18), 1861.

30. Wei, S.; Chou, M. Y., Phonon dispersions of silicon and germanium from first-principles calculations. *Phys. Rev. B* 1994, 50, (4), 2221.

31. Frank, W.; Elsässer, C.; Fähnle, M., Ab initio Force-Constant Method for Phonon Dispersions in Alkali Metals. *Phys. Rev. Lett.* 1995, 74, (10), 1791.

32. Parlinski, K.; Li, Z. Q.; Kawazoe, Y., First-Principles Determination of the Softmode in Cubic ZrO_2. *Phys. Rev. Lett.* 1997, 78, (21), 4063.

33. Parlinski, K., Lattice dynamics of cubic BN. *J. Alloys Compd.* 2001, 328, (1-2), 97-99.

34. Parlinski, K.; Parlinska-Wojtan, M., Lattice dynamics of NiTi austenite, martensite, and R phase. *Phys. Rev. B* 2002, 66, (6), 064307.

35. Parlinski, K. *PHONON*, 2005.

36. TA instrument website. "SDT tutorial," online posting, www.tainstruments.com.

37. Quantachrome instruments web site. "Autosorb1-C Chemisorption - Physisorption Analyzer manual," online posting, www.quantachrome.com.

38. Bruce M. Clemens (2006). "GCEP technical report 2006," online posting, http://gcep.stanford.edu.

39. Keck Interdisciplinary Surface Science Center (2005). "Fourier Transform Infrared Spectroscopy (FT-IR)," online posting, www.nuance.northwestern.edu

40. www.infohost.nmt.edu~maximino/fesem_types_of_signals.htm

41. ETH Zürich website. "SEM technology," online posting, www.microscopy.ethz.ch/sem.htm.

42. Miwa, K.; Ohba, N.; Towata, S.-i.; Nakamori, Y.; Züttel, A.; Orimo, S.-i., First-principles study on thermodynamical stability of metal borohydrides: Aluminum borohydride $Al(BH_4)_3$. *J. Alloys Compd.* 2007, 446-447, 310-314.

43. Miwa, K.; Aoki, M.; Noritake, T.; Ohba, N.; Nakamori, Y.; Towata, S.; Zu¨ttel, A.; Orimo, S., Thermodynamical stability of calcum borohydride $Ca(BH_4)_2$. *Phys. Rev. B* 2006, 74, 155122.

44. Zu¨ttel, A.; Rentsch, S.; Fischer, P.; Wenger, P.; Sudan, P.; Mauron, P.; Emmenegger, C., H ydrogen storage properties of $LiBH_4$. *J. Alloys Compd.* 2003, 356-357, 515-520.

45. Lodziana, Z.; Vegge, T., Structural Stability of Complex Hydrides: $LiBH_4$ Revisited. *phys. Rev. Lett.* 2004, 93, (14), 145501.

46. Nakamori, Y.; Miwa, K.; Ninomiya, A.; Li, H.; Ohba, N.; Towata, S.-i.; Züttel, A.; Orimo, S.-i., Correlation between thermodynamical stabilities of metal borohydrides and cation electronegativites: First-principles calculations and experiments. *Phys. Rev. B* 2006, 74, 045126.

47. Grochala, W.; Edwards, P. P., Thermal Decomposition of the Non-Interstitial Hydrides for the Storage and Production of Hydrogen. *Chem. Rev.* 2004, 104, (3), 1283-1315.

48. Jeon, E.; Cho, Y., Mechanochemical synthesis and thermal decomposition of zinc borohydride. *J. Alloys Compd.* 2006, 422, 273–275.

49. Hafner, J.; Wolverton, C.; Ceder, G., Toward Computational Materials Design: The Impact of Density Functional Calculations on Materials Science. *MRS Bulletin* 2006, 31, 659.

50. Herbst, J. F.; Hector, J. L. G., Electronic structure and energetics of the quaternary hydride $Li_4BN_3H_{10}$. *Appl. Phys. Lett.* 2006, 88, (23), 231904-3.

51. Majzoub, E. H.; McCarty, K. F.; Ozolinš, V., Lattice dynamics of $NaAlH_4$ from high-temperature single-crystal Raman scattering and ab initio calculations: Evidence of highly stable AlH_4^- anions. *Phys. Rev. B* 2005, 71, 024118.

52. Íñiguez, J.; Yildirim, T.; Udovic, T. J.; Sulic, M.; Jensen, C. M., Structure and hydrogen dynamics of pure and Ti-doped sodium alanate. *Phys. Rev. B* 2004, 70, (6), 060101.

53. Marashdeh, A.; Olsen, R. A.; Løvvik, O. M.; Kroes, G.-J., A density functional theory study of Ti-doped $NaAlH_4$ clusters. *Chem. Phys. Lett.* 2006, 426, (1-3), 180-186.

54. Vegge, T., Equilibrium structure and Ti-catalyzed H_2 desorption in $NaAlH_4$ nanoparticles from density functional theory. *Phys. Chem. Chem. Phys.* 2006, 8, 4853.

55. Zarkevich, N. A.; Johnson, D. D., Structural Stability of Complex Hydrides: $LiBH_4$ Revisited. *Phys. Rev. Lett.* 2006, 97, 119601.

56. Vajeeston, P.; Ravindran, P.; Kjekshus, A.; Fjellv°ag, H., High hydrogen content complex hydrides: A density-functional study. *Appl. Phys. Lett.* 2006, 89, 071906.

57. Zeng, Q.; Su, K.; Zhang, L.; Xu, Y.; Cheng, L.; Yan, X., Evaluation of the Thermodynamic Data of CH_3SiCl_3 Based on Quantum Chemistry Calculations. *J. Phys. Chem. Ref. Data* 2006, 35, (3), 1385.

58. Alapati, S. V.; Johnson, J. K.; Sholl, D. S., Identification of Destabilized Metal Hydrides for Hydrogen Storage Using First Principles Calculations. *J. Phys. Chem. B* 2006, 110, 8769-8776.

59. Perdew, J. P.; Chevary, J. A.; Vosko, S. H.; Jackson, K. A.; Pederson, M. R.; Singh, D. J.; Fiolhais, C., Atoms, molecules, solids, and surfaces: Applications of the generalized gradient approximation for exchange and correlation. *Phys. Rev. B* 1992, 46, (11), 6671.

60. Kresse, G.; Joubert, D., From ultrasoft pseudopotentials to the projector augmented-wave method. *Phys. Rev. B* 1999, 59, (3), 1758.

61. Monkhorst, H. J.; Pack, J. D., Special points for Brillouin-zone integrations. *Phys. Rev. B* 1976, 13, (12), 5188.

62. http://www.mkmc.dk/crystal/194/Mg/Zn/main.html, Zn.

63. Park, C. H.; Chadi, D. J., First-principles study of the atomic reconstrcutions of ZnSe(100) surfaces. *Phys. Rev. B* 1994, 49, 16467.

64. http://www.webelements.com/webelements/properties/text/definitions/crystal-structure.html.

65. vanSetten, M. J.; deWijs, G. A., Ab initio study of $Mg(AlH_4)_2$. *Phys. Rev. B* 2005, 72, 073107.

66. http://cst-www.nrl.navy.mil/lattice/struk.xmol/alphaB.pos, Boron.

67. Prasad, D. L. V. K.; Balakrishnarajan, M. M.; Jemmis, E. D., Electronic structure and bonding of β-rhombohedral boron using cluster fragment approach. *Phys. Rev. B* 2005, 72, 195102.

68. Pistorius, C. W. F. T., *Z. Phys. Chem., Neue Folge* 1974, 88, 253.

69. Løvvik, O. M., Crystal structure of $Ca(AlH_4)_2$ predicted from density-functional band-structure calculations. *Phys. Rev. B* 2005, 71, 144111.

70. Wolverton, C.; Ozolins, V., Hydrogen storage in calcium alanate: First-principles thermodynamics and crystal structures. *Phys. Rev. B* 2007, 75, 064101.

71. Løvvik, O. M.; Molin, P. N., Density-functional band-structure calculations of magnesium alanate $Mg(AlH_4)_2$. *Phys. Rev. B* 2005, 72, 073201.

72. Kitajima, N.; Shimanouchi, H.; Ono, Y.; Sasada, Y., The crystal and Molecular Structure of $Cu(AlCl_4)_2$. *Bull. Chem.Soc. Jpn.* 1982, 55, (7), 2064 - 2067.

73. Marynick, D. S.; Lipscomb, W. N., Crystal Structure of Beryllium Borohydride. *Inorg. Chem.* 1972, 11, (4), 820.

74. http://cms.mpi.univie.ac.at/vasp-workshop/.

75. Miwa, K.; Ohba, N.; Towata, S.-i.; Nakamori, Y.; Orimo, S.-i., First-principles study on lithium borohydride $LiBH_4$. *Phys. Rev. B* 2004, 69, 245120.

76. Becke, A. D.; Edgecombe, K. E., A simple measure of electron localization in atomic and molecular systems. *J. Chem. Phys.* 1990, 92, (9), 5397-5403.

77. Silvi, B.; Savin, A., Classification of chemical bonds based on topological analysis of electron localization functions. *Nature* 1994, 371, (6499), 683-686.

78. Borelius, G., Zero-point Energy of Electrons and Phonons in the Periodic System. *Phys. Scr.* 1978, 18, 19-12.

79. Siegel, D. J.; Wolverton, C., Reaction energetics and crystal structure of $Li_4BN_3H_{10}$ from first principles. *Phys. Rev. B* 2007, 75, 014101.

80. Hu, S.-W.; Wang, Y.; Wang, X.-Y.; Chu, T.-W.; Liu, X.-Q., Gas-Phase Reactions between Diborane and Carbon Monoxide: A Theoretical Study. *J. Phys. Chem. A* 2003, 107, 9974-9983.

81. Greene, T. M.; Brown, W.; Andrews, L.; Downs, A. J.; Chertihin, G. V.; Runeberg, N.; Pyykko, P., Matrix Infrared Spectroscopic and ab Initio Studies of ZnH_2, CdH_2, and Related Metal Hydride Species. *J. Phy. Chem.* 1995, 99, 7925.

82. http://en.wikipedia.org/wiki/Diborane.

83. Araujo, C. M.; Ahuja, R.; Guillen, J. M. O.; Jena, P., Role of titanium in hydrogen desorption in crystalline sodium alanate. *Appl. Phys. Lett.* 2005, 86, 251913.

84. Lee, E.-K.; Cho, Y. W.; Yoon, J. K., Ab-initio calculations of titanium solubility in $NaAlH_4$ and Na_3AlH_6. *J. Alloys Compd.* 2006, 416, (1-2), 245-249.

85. Blomqvist, A.; Araujo, C. M.; Jena, P.; Ahuja, R., Dehydrogenation from 3 *d*-transition-metal-doped $NaAlH_4$: Prediction of catalysts. *Appl. Phys. Lett.* 2007, 90, 141904.

86. Alapati, S. V.; Johnson, J. K.; Sholl, D. S., Stability analysis of doped materials for reversible hydrogen storage in destabilized metal hydrides. *Phys. Rev. B* 2007, 76, 104108.

87. Srinivasan, S.; Escobar, D.; Jurczyk, M.; Choudhury, P.; Goswami, Y.; Stefanakos, E., Effects of nanocatalyst doping on the hydrogen storage behavior of new complex borohydrides. *IHEC '07 Proc.* 2007.

88. Srinivasan, S.; Escobar, D.; Jurczyk, M.; Goswami, Y.; Stefanakos, E., Nanocatalyst doping of $Zn(BH_4)_2$ for on-board hydrogen storage. *J. Alloys Compd.* 2008, 462, (1-2), 294-302.

89. Schlapbach, L.; Zuttel, A., Hydrogen-storage materials for mobile applications. *Nature* 2001, 414, (6861), 353-358.

90. Bogdanovi, B.; Schwickardi, M., Ti-doped alkali metal aluminium hydrides as potential novel reversible hydrogen storage materials. *J. Alloys Compd.* 1997, 253-254, 1-9.

91. Jensen, C. M.; Zidan, R. A., Hydrogen storage materials and. method of making by dry homogenation. *U. S. Patent* 2002, 6, 471935.

92. Frankcombe, T. J.; Kroes, G.-J., Quasiharmonic approximation applied to $LiBH_4$ and its decomposition products. *Phys. Rev. B* 2006, 73, 174302.

93. Choudhury, P.; Bhethanabotla, V. R.; Stefanakos, E., Identification of a stable phase for the high-capacity hydrogen-storage material $Zn(BH_4)_2$ from density functional theory and lattice dynamics. *Phys. Rev. B* 2008, 77, (13), 134302-9.

94. Choudhury, P.; Bhethanabotla, V. R.; Stefanakos, E., Ni-induced destabilization dynamics of crystalline zinc borohydride. *Appl. Phys. Lett.* 2008, 92, (13), 134101-3.

95. Wang, X.; Andrews, L., Matrix Infrared Spectra and Density Functional Theory Calculations of Manganese and Rhenium Hydrides. *J. Phys. Chem. A* 2003, 107, (20), 4081-4091.

96. Vajeeston, P.; Ravindran, P.; Ravi, C.; Asokamani, R., Electronic structure, bonding, and ground-state properties of AlB_2-type transition-metal diborides. *Phys. Rev. B* 2001, 63, (4), 045115.

97. Hobbs, D.; Hafner, J.; Spisak, D., Understanding the complex metallic element Mn. I. Crystalline and noncollinear magnetic structure of alpha -Mn. *Phys. Rev. B* 2003, 68, (1), 014407.

98. Choudhury, P.; Srinivasan, S.; Bhethanabotla, V. R.; Stefanakos, E., Transition metal complex hydrides for vehicular application. *FLAVS Meeting, Orlando, FL* 2008.

99. Fossdal, A.; Brinks, H. W.; Fichtner, M.; Haubacka, B. C., Determination of the crystal structure of $Mg(AlH_4)_2$ by combined X-ray and neutron diffraction. *J. Alloys Compd.* 2005, 387, 47-51.

100. Fichtner, M.; Engel, J.; Fuhr, O.; Gloss, A.; Rubner, O.; Ahlrichs, R., The Structure of Magnesium Alanate. *Inorg. Chem.* 2003, 42, 7060 - 7066.

101. Fichtner, M.; Fuhr, O., S ynthesis and structures of magnesium alanate and two solvent adducts. *J. Alloys Compd.* 2002, 345, 286-296.

102. Fichtner, M.; Fuhr, O.; Kircher, O., M agnesium alanate—a material for reversible hydrogen storage? *J. Alloys Compd.* 2003, 356-357, 418-422.

103. Einarsrud, M. A.; Justnes, H.; Rytter, E.; Oye, H. A., Structure and Stability of Solid and Molten Complexes in the $MgCl_2$-$AlCl_3$ System. *Polyhedron* 1987, 6, (5), 975 - 986.

104. Ozolins, V.; Majzoub, E. H.; Wolverton, C., First-Principles Prediction of a Ground State Crystal Structure of Magnesium Borohydride. *Phys. Rev. Lett.* 2008, 100, 135501.

105. Jorgensen, J. D.; Hu, Z.; Teslic, S.; Argyriou, D. N.; Short, S.; Evans, J. S. O.; Sleight, A. W., Pressure-induced cubic-to-orthorhombic phase transition in ZrW_2O_8. *Phys. Rev. B* 1999, 59, (1), 215 - 225.

106. Andersen, A. M. K.; Carlson, S., High-pressure structre of alpha and delta $ZrMo_2O_8$. *Acta. Cryst. B* 2000, 57, 20 - 26.

107. Justnes, A.; Rytter, E.; F.Andresen, A., A Crystal structure determination of Titanium(II) Tetrachloroaluminate by Vibrational Correlation Methods and Powder Diffration. *Polyhedron* 1982, 1, (4), 393 - 396.

108. Staffel, T.; Meyer, G., Synthesis and Crystal Structure of $Cd[AlCl_4]_2$ and $Cd_2[AlCl_4]_2$. *Z. anorg. allg. Chem.* 1987, 548, 45 - 54.

109. Butz, A.; Miehe, G.; Paulus, H.; Strauss, P.; Fuess, H., The Crystal Structure of $Mn(ReO_4)_2 \cdot 2H_2O$ and of the Anhydrous Perrhenates $M(ReO_4)_2$ of Divalent Manganese, Cobalt, Nickel, and Zinc. *J. Solid State Chem.* 1998, 138, 232 - 237.

110. Du, A. J.; Smith, S. C.; Lu, G. Q., Role of charge in destabilizing AlH_4 and BH_4 complex anions for hydrogen storage applications: Ab initio density functional calculations. *Phys. Rev. B* 2006, 74, (19), 193405-4.

111. Chase, M. W. J., *NIST-JANAF Themochemical Tables, Fourth Edition, J. Phys. Chem. Ref. Data, Monograph 9,1-1951 (1998).*

112. Zhang, X.-B.; Shi, S.-Q.; Ke, X.-Z.; Han, S.; Shioyama, H.; Kuriyama, N.; Kobayashi, T.; Xu, Q., Dehydrogenation Reaction for Na-O-H System: A First-Principles Study. *ChemPhysChem* 2007, 8, (13), 1979-1987.

113. Reuter, K.; Scheffler, M., Composition, structure, and stability of RuO_2(110) as a function of oxygen pressure. *Phys. Rev. B* 2001, 65, (3), 035406.

114. Stull, D. R.; Scheffler, M., *JANAF Thermochemical Tables, 2nd ed. (U.S. National Bureau of Standards, Washington, DC, 1971).*

115. Topor, L.; Kleppa, O. J., Enthalpies of formation of first-row transition-metal diborides by a new calorimetric method. *J. Chem. Thermodyn.* 1985, 17, (11), 1003-1016.

116. Donald, J. S.; Wolverton, C., Reaction energetics and crystal structure of $Li_4BN_3H_{10}$ from first principles. *Phys. Rev. B* 2007, 75, 014101.

117. Liu, Y.; Hu, J.; Wu, G.; Xiong, Z.; Chen, P., Formation and Equilibrium of Ammonia in the $Mg(NH_2)_2$-2LiH Hydrogen Storage System. *J. Phys. Chem. C* 2008, 112, 1293-1298.

118. Srinivasan, S.; Escobar, D.; Goswami, Y.; Stefanakos, E., Effects of catalysts doping on the thermal decomposition behavior of $Zn(BH_4)_2$. *Int. J. Hydrogen Energy* 2008, 33, 2268-2272.

119. Sudik, A.; Yang, J.; Halliday, D.; Wolverton, C., Hydrogen Storage Properties in $(LiNH_2)_2$-$LiBH_4$-$(MgH_2)_X$ Mixtures (X = 0.0 -1.0). *J. Phys. Chem. C* 2008, 112, 4384-4390.

120. Satyapal, S.; Petrovic, J.; Read, C.; Thomas, G.; Ordaz, G., The U.S. Department of Energy's National Hydrogen Storage Project: Progress Towards Meeting Hydrogen-Powered Vehicle Requirements. *Catal. Today* 2006, 120, 246.

121. Wolverton, C.; Siegel, D. J.; Akbarzadeh, A. R.; Ozolins, V., Discovery of novel hydrogen storage materials: an atomic scale computational approach. *J. Phys.: Condens. Matter* 2008, 20, 064228

122. Akbarzadeh, A. R.; Ozolinš, V.; Wolverton, C., First-Principles Determination of Multicomponent Hydride Phase Diagrams: Application to the Li-Mg-N-H System. *Adv. Mater.* 2007, 19, 3233-3239.

123. Chen, P.; Xiong, Z.; Yang, L.; Wu, G.; Luo, W., Mechanistic Investigations on the Heterogeneous Solid-State Reaction of Magnesium Amides and Lithium Hydrides. *J. Phys. Chem. B* 2006, 110, 14221-14225.

124. Leng, H.; Ichikawa, T.; Fujii, H., Hydrogen Storage Properties of Li-Mg-N-H Systems with Different Ratios of $LiH/Mg(NH_2)_2$. *J. Phys. Chem. B* 2006, 110, 12964-12968.

125. Wang, Y.; Chou, M. Y., First-principles study of cation and hydrogen arrangements in the Li-Mg-N-H hydrogen storage system. *Phys. Rev. B* 2007, 76, 014116.

126. Vajo, J. J.; Skeith, S. L.; Mertens, F., Reversible Storage of Hydrogen in Destabilized $LiBH_4$. *J. Phy. Chem. B* 2005, 109, 3719.

127. Luo, S.; Flanagan, T. B.; Luo, W., The effect of exposure of the H-storage system ($LiNH_2$ + MgH_2) to water-saturated air. *J. Alloys Compd.* 2007, 440, (1-2), L13-L17.

128. Sudik, A.; Yang, J.; Siegel, D. J.; Wolverton, C.; III., R. O. C.; Drews, A. R., Impact of Stoichiometry on the Hydrogen Storage Properties of $LiNH_2$-$LiBH_4$-MgH_2 Ternary Composites. *J. Phys. Chem. C* 2009, 113, 2004-2013.

129. Perdew, J. P.; Burke, K.; Ernzerhof, M., Generalized Gradient Approximation Made Simple. *Phys. Rev. Lett.* 1996, 77, (18), 3865.

130. Barrera, G. D.; Colognesi, D.; Mitchell, P. C. H.; Ramirez-Cuesta, A. J., LDA or GGA? A Combined Experimental Inelastic Neutron Scattering and Ab Initio Lattice Dynamics Study of Alkali Metal Hydrides. *Chem. Phys.* 2005, 317, 119.

131. Alapati, S. V.; Johnson, J. K.; Sholl, D. S., Using First Principles Calculation to Identify New Destabilized Metal Hydride Reactions for Reversible Hydrogen Storage. *Phys. Chem. Chem. Phys.* 2007, 8, 1438.

132. Choudhury, P.; Bhethanabotla, V. R.; Stefanakos, E., Manganese borohydride as a hydrogen storage candidate: First-principles crystal structure and thermodynamic properties. *J. Phy. Chem. C* 2009, 113, 13416-13424.

133. Velikokhatnyi, O. I.; Kumta, P. N., Energetics of the lithium-magnesium imide–magnesium amide and lithium hydride reaction for hydrogen storage: An ab initio study. *Mater. Sci. Eng., B* 2007, 140, 114-122.

134. The Inorganic Crystal Structure Database (ICSD), http://www.fiz-informationsdienste.de/en/DB/icsd/.

135. Herbst, J. F.; L. G. Hector, J., Energetics of the Li amide/Li imide hydrogen storage reaction. *Phys. Rev. B* 2005, 72, 125120.

136. Niemann, M. U.; Srinivasan, S. S.; Kumar, A.; Stefanakos, E. K.; Goswami, Y.; McGrath, K., Processing Analysis of the Ternary LiNH2-MgH2-LiBH4 System for Hydrogen Storage. *Int. J. Hydrogen Energy* 2009, (Submitted).

137. Yang, J.; Sudik, A.; Siegel, D. J.; Halliday, D.; Drews, A.; III, R. O. C.; Wolverton, C.; Lewis, G. J.; Sachtler, J. W. A.; Low, J. J.; Faheem, S. A.; Lesch, D. A.; Ozolins, V., Hydrogen storage properties of $2LiNH_2$ + $LiBH_4$ + MgH_2. *J. Alloys. Compd.* 2007, 446-447, 345.

138. Yang, J. C., Material-based hydrogen storage. *Int. J. Hydrogen Energy* 2008, 33, (16), 4424-4426.

139. Crabtree, G. M.; Dresselhaus, M. S.; Buchanan, M. V., The Hydrogen Economy *Physics Today* 2004, 57, (12), 39-44.

140. Edwards, P. P.; Grochala, W.; Book, D.; Harris, I., *Metal Hydride Synthesis and a Fuel Cell Using Metal Hydrides for Hydrogen Storage*. In: Office EP ed.; 2004.

141. Stefanakos, E.; Goswami, Y.; Srinivasan, S.; Wolan, J., In *J. Hydrogen Energy Myer Kutz (Hrsg.) Environmentally Conscious Alternative Energy Production, John Wiley & Sons, 4, 165 (2007)*

142. Bogdanovic, B.; Schwickardi, M., Ti-doped alkali metal aluminium hydrides as potential novel reversible hydrogen storage materials. *J. Alloys Compd.* 1997, 253-254, 1-9.

143. Bogdanovic, B.; Schwickardi, M., *Verfahren zur reversilben Speicherung von Wasserstoff*. In: Office EP ed.; 1997.

144. Graetz, J.; Lee, Y.; Reilly, J. J.; Park, S.; Vogt, T., Structures and thermodynamics of the mixed alkali alanates. *Phys. Rev. B* 2005, 71, (18), 184115.

145. Jensen, C. M.; Zidan, R., *Hydrogen Storage Materials and Methods of Making by Dry Hydrogenation*. In: Office UP ed.; 2002; Vol. 6, 471, 935 B2. USA.

146. Kang, J. K.; Lee, J. Y.; Muller, R. P.; III, W. A. G., Hydrogen storage in $LiAlH_4$: Predictions of the crystal structures and reaction mechanisms of intermediate phases from quantum mechanics. *J. Chem. Phys.* 2004, 121, (21), 10623.

147. Brinks, H. W.; Brown, C.; Jensen, C. M.; Graetz, J.; Reilly, J. J.; Hauback, B. C., The crystal structure of α -AlD_3. *J. Alloys. Compd.* 2007, 441, (1-2), 364-367.

148. Graetz, J.; Reilly, J. J.; Kulleck, J. G.; Bowman, R. C., Kinetics and thermodynamics of the aluminum hydride polymorphs. *J. Alloys. Compd.* 2007, 446-447, 271-275.

149. Au, M. Destabilized and catalyzed alkali metal borohydrides for hydrogen storage with good reversibility, U.S. Patent Appl. Publ., US 2006/0194695 A1, Aug. 31. 2006.

150. Chen, P.; Xiong, Z.; Lou, J.; Lin, J.; Tan, K. L., Interaction of hydrogen with metal nitrides and imides. *Nature* 2002, 420, 302.

151. Hu, Y. H.; Ruckenstein, E., H_2 Storage in Li_3N. Temperature-Programmed Hydrogenation and Dehydrogenation. *Ind. Eng. Chem. Res.* 2003, 42, (21), 5135-5139.

152. Lewis, J. G.; Sachtler, J. W.; Drews, A.; Low, J. J.; Lesch, D. A.; Faheem, S. A.; Dosek, P. M.; Knight, L. M.; Halloran, L.; Jensen, C. M.; Yang, J.; Sudik, A.; Siegel, D. J.; Wolverton, C.; Ozolins, V.; Zhang, S., High throughput screening of the ternary $LiNH_2$–MgH_2–$LiBH_4$ phase diagram. *J. Alloys. Compd.* 2007, 446-447, 355-359.

153. Niemann, M.; Srinivasan, S.; McGrath, K.; Kumar, A.; Goswami, Y.; Stefanakos, E., Nanocrystalline effects in complex composite hydrides. *Ceramic Transactions* 2009, 202, 111.

154. Bogdanovic, B.; Felderhoff, M.; Kaskel, S.; Pommerin, A.; Schlichte, K.; Schuth, F., Improved hydrogen storage properties of Ti-doped sodium aluminate using titanium nanoparticles as doping agents. *Adv. Mater.* 2003, 15, (12), 1012.

155. Bogdanovic, B.; Ritter, A.; Spliethoff, B., Active MgH2-Mg systems for reversible chemical energy storage. *Angew. Chem. Int. Ed. Engl* 1990, 29, 223.

156. *Report of the Basic Energy Science Workshop on Hydrogen Production, Storage and use prepared by* Argonne National Laboratory: May 13-15, 2003.

157. Satyapal, S.; Petrovic, J.; Thomas, G., Gassing with Hydrogen. *Scientific American* 2007, 81-87.

158. Nakamori, Y.; Ninomiya, A.; Kitahara, G.; Aoki, M.; Noritake, T.; Miwa, K.; Kojima, Y.; Orimo, S., Dehydriding reactions of mixed complex hydrides. *J. Power Sources* 2006, 155, 47.

159. Li, Z. P.; Liu, B. H.; Arai, K.; Morigazaki, N.; Suda, S., Protide compounds in hydrogen storage systems. *J. Alloys. Compd.* 2003, 356-357, 469-474.

160. Zuttel, A.; Wenger, P.; Rentsch, S.; Sudan, P.; Mauron, P.; Emmeneger, C., $LiBH_4$ a new hydrogen storage material. *J. Power Sources* 2003, 118, 1.

161. Narashimhan, S.; Balakumar, R., Synthetic Applications of Zinc Borohydride. *Aldrichimica Acta* 1998, 31, (1), 19-26.

162. Grove, H.; Brinks, H. W.; Heyn, R. H.; Wu, F.-J.; Opalka, S. M.; Tang, X.; Laube, B. L.; Hauback, B. C., The structure of $LiMg(AlD_4)_3$. *J. Alloys. Compd.* 2008, 455, 249-254.

163. Nakamura, Y.; Fossdal, A.; Brinks, H. W.; Hauback, B. C., Characterization of Al-Ti phases in cycled TiF_3-enhanced Na2LiAlH_6. *J. Alloys. Compd.* 2006, 416, (1-2), 274-278.

164. Hagemann, H.; Longhini, M.; Kaminski, J. W.; Wesolowski, T. A.; Cerny, R.; Penin, N.; Sorby, M. H.; Hauback, B. C.; Severa, G.; Jensen, C. M., $LiSc(BH_4)_4$: A Novel Salt of Li^+ and Discrete $Sc(BH_4)^{4-}$ Complex Anions. *J. Phys. Chem. A* 2008, 112, (33), 7551-7555.

165. Kissinger, H. E., Variation of Peak Temperature With Heating Rate in Differential Thermal Analysis. *Journal of Research of the National Bureau of Standards* 1956, 57, 217.

166. Joo, S. H.; Choi, S. J.; Ryoo, R., Ordered nanoporous arrays of carbon supporting high dispersions of platinum nanoparticles. *Nature* 2001, 412, 169.

About the Author

Pabitra Choudhury was born in Barnia of Nadia district in West Bengal, India. He completed both his middle and high school education at Bethuadahari J. C. M. High School, Nadia of West Bengal, India. Pabitra holds a BS from IIT, Bombay and an MS from IIT, Roorkee, India, both in chemical engineering.

He began pursuing his Ph.D. degree in the Chemical and Biomedical Engineering Department at University of South Florida in 2006. His dissertation research as applied to materials related to energy field resulted in publications in high quality journals such as Physical Review B, Applied Physics Letters, Journal of Physical Chemistry C, and International Journal of Hydrogen Energy. His research has also resulted in 15+ publications including conference/symposium proceedings, associated with prestigious national and international conferences.